The Dissertation Committee for Nellymar Membreño Certifies that this is the approved version of the following dissertation:

Characterizing the Lithiation and Failure Mechanisms of Transition Metal Phosphates and Phosphides for Lithium Ion Batteries

Committee:

Keith J. Stevenson, Supervisor

Graeme Henkelman

Lauren J.Webb

Delia J. Milliron

Richard M. Crooks

Characterizing the Lithiation and Failure Mechanisms of Transition Metal Phosphates and Phosphides for Lithium Ion Batteries

by

Nellymar Membreño, B.S.

Dissertation

Presented to the Faculty of the Graduate School of

The University of Texas at Austin

in Partial Fulfillment

of the Requirements

for the Degree of

Doctor of Philosophy

The University of Texas at Austin

May 2015

Dedication

To my parents, Elimar and Alvaro Membreño.

Acknowledgements

I would like to acknowledge all of the scientists in the Stevenson lab with whom I had the pleasure to work with and learn from. This includes Jing Wu, Jacob Goran, Salome Ngatia, Cori Atkinson, Jaclyn Wiggins-Camacho, Katie Walker, Sankaran Murugesan, Srinivas Beeram, Radhika Dasari, Anthony Dylla, Alex Veneman, Kjell Schroder, Aoife O'Mahony, Jonathon Duay, William Hardin, Ian Rust, Donald Robinson, Matthew Charlton, Daniel Redman, Tyler Mefford, Janine Elliot, Dean Campbell and Mi Chen.

I would also like to thank my collaborators Kyusung Park, Penghao Xiao, Justin Hall, Prof. John B. Goodenough, Prof. Graeme Henkelman and Prof. Richard A. Jones. Very special thanks go to the undergraduates and high school student Paola Quijano, Alexa Marsh and Souvik Banarjee for helping me complete my experiments and for entrusting me as your mentor during the time you spent with me. I am also greatly indebted to the help of Ricardo Palacios and David Gray from the aerospace machine shop for their great suggestions and machining of the *in situ* Raman miscroscopy test cell.

To my friends Rachel Anderson, Netzahaulcóyotl Arroyo Curras and Karen Scida thank you for the many fruitful electrochemistry and non-electrochemistry related discussions throughout the years.

For those who influenced and nurtured me as a junior scientist before entering graduate school I also give my gratitude. This includes my tremendous high school chemistry teacher Dr. Phyllis Hoar and my undergraduate advisors Dr. Yong Cai, Dr. Cynthia K. Larive and Dr. William R. Heiniman. As well as their graduate students that

allowed me to work on their projects Lucy Yehiayan, Christopher J. Jones and Robert A. Wilson.

Finally, I would like to thank my advisor Keith J. Stevenson for his guidance, support and mentorship throughout my graduate career.

Characterizing the Lithiation and Failure Mechanisms of Transition Metal Phosphates and Phosphides for Lithium Ion Batteries

Nellymar Membreño, PhD

The University of Texas at Austin, 2015

Supervisor: Keith J. Stevenson

In this dissertation the lithiation and failure mechanisms of some promising transition metal phosphide and phosphate materials are discussed for application in lithium ion batteries (LIBs). More specifically, the materials investigated include the intercalation cathode $Li_3V_2(PO_4)_3$ and the conversion anode FeP_2. For FeP_2, a nano amorphous material obtained through a novel, low-temperature synthetic reaction was galvanostatically characterized and the correlation between its morphology and lithiation properties is discussed. For $Li_3V_2(PO_4)_3$, Raman microscopy and X-ray photoelectron spectroscopy (XPS) are primarily used as the analytical techniques to characterize the bulk and surface chemistry of this material. In the first chapter the advancements and current challenges of LIBs are discussed. A brief overview on the different lithiation mechanisms (intercalation, alloying and conversion) is presented along with the cathode and anodes that historically have been of interest. The potential of $Li_3V_2(PO_4)_3$ and FeP_2 as next generation LIB electrodes is also discussed. In the second chapter we present the first reports of a nano, amorphous FeP_2 material obtained through a novel, low-temperature reaction between a σ-bonded alkly Fe complex with PH_3. Electrochemical lithiation of nano, amorphous FeP_2 showed superior performance to the bulk, crystalline morphology and a competing lithiation mechanism between classical intercalation and

conversion is proposed. The third chapter discusses the monoclinic phase of $Li_3V_2(PO_4)_3$ which is characterized via Raman microscopy and compared to the spectrum calculated through density functional theory (DFT) providing groundwork for future *in situ* experiments. The fourth chapter reports on XPS measurements of composite $Li_3V_2(PO_4)_3$ electrodes after complete intercalation/deintercalation reactions and specifically examines the role that the carbon black additive plays on the interface of the composite electrode and electrolyte. Finally, the fifth chapter presents a novel design for an *in situ* Raman microscopy test cell for LIBs along with a detailed explanation of the important component and design criteria for optimal scattering and electrochemical measurements. Future *in situ* Raman microscopy experiments for $Li_3V_2(PO_4)$ and other LIB materials of interest are discussed.

Table of Contents

CHAPTER 1 1

Lithium Ion Batteries: Characteristics and Limitations 1

1.1 Introduction 1

1.2 References 18

CHAPTER 2 21

Low-Temperature Synthesis of Amorphous FeP_2 and Its Use as Anodes for Li Ion Batteries 21

2.1 Introduction 21

2.2 Experimental Section 23

2.2.1 General Experimental Information 23

2.2.2 Synthesis of Amorphous FeP_2 23

2.2.3 Electrochemical Characterization 23

2.2.4 XPS Analysis 24

2.2.5 Elemental Analysis 25

2.3 Results and Discussion 25

2.4 Conclusions 35

2.5 References 35

CHAPTER 3 39

In Situ Raman Study of Phase Stability of $Li_3V_2(PO_4)_3$ upon Thermal and Laser Heating 39

3.1 Introduction 39

3.2 Experimental and Theoretical Methods 42

3.2.1 α-$Li_3V_2(PO_4)_3$ Solid State Synthesis 42

3.2.2 XRD Characterization 43

3.2.3 Scanning Electron Microscopy 43

3.2.4 *Ex situ* and *In situ* Raman Microscopy 43

3.2.5 Thermal Studies 44

3.2.6 VASP-DFT 44
3.3 Results and Discussion 45
3.3.2 Comparison of Experimental and Theoretical Raman Spectra ...47
3.3.3 Vibrational Modes of α-$Li_3V_2(PO_4)_3$ as a Function of Laser Irradiation Power 51
3.3.4 Thermal studies on α-$Li_3V_2(PO_4)_3$ 55
3.4 Conclusions 67
3.5 References 68

CHAPTER 4 70

Electrode/Electrolyte Interface of Composite α-$Li_3V_2(PO_4)_3$ Cathodes in a Non-Aqueous Electrolyte for Lithium Ion Batteries and the Role of the Carbon Additive 70
4.1 Introduction 70
4.2 Experimental Section 73
4.2.1 Preparation of α-$Li_3V_2(PO_4)_3$ 73
4.2.2 Electrochemical Analysis 74
4.2.3 X-ray photoelectron spectroscopy (XPS) 74
4.3 Results and Discussion 75
4.3.1 Electrochemistry of $Li_3V_2(PO_4)_3$ 75
4.3.2 XPS Characterization of the SEI 80
4.3.3 SEI on Anode vs. Cathode 86
4.3.4 SEI on TMPs 88
4.3.5 SEI on $Li_3V_2(PO_4)_3$ 89
4.3.6 Spontaneous Reactions Between $Li_3V_2(PO_4)_3$ & Electrolyte 91
4.3.7 Limitations in Analyzing Composite Electrodes 97
4.4 Conclusions 99
4.5 References 101

CHAPTER 5 104

Future Direction: Novel *In Situ* Raman Microscopy Test Cell for Lithium Ion Batteries 104

5.1 Introduction 104

5.2 Experimental Section 106

5.2.1 Materials for the test cell 106

5.2.2 Full cell construction 107

5.2.3 Titanium Metallocene O_2 indicator 110

5.2.4 Electrode Materials 110

5.2.5 Raman Microscopy Measurements 112

5.3 Results and Discussion 113

5.3.1 Oxygen test 113

5.3.2 Electrochemical Performance 113

5.3.3 *In situ* Raman microscopy of a carbon black material at high operating potentials 117

5.3.4 ALD deposited TiO_2 as a model electrode 119

5.4 Conclusions 123

5.5 References 124

Appendix 125

References 131

CHAPTER 1

Lithium Ion Batteries: Characteristics and Limitations

1.1 INTRODUCTION

Today's society depends on oil for vehicle transportation; however, the fluctuating prices, climate effects from the CO_2 byproduct and limited reserves in only a few countries makes it one of the greatest global challenges for this generation.[1] As a result, research on alternative energy sources has soared with a vital emphasis on lithium ion technology as a power source for vehicle propulsion. Yet, there are many technological challenges that have to be resolved before LIBs match the performance of internal combustion vehicles.[2–4] Superior power, energy density, cycle life, safety and cost are all needed to meet the energy storage demands for electric transportation. This requires the use of high voltage cathodes (i.e. $Li_3V_2(PO_4)_3$) and low voltage anodes (i.e. FeP_2) that operate beyond the stability limits of common LIB electrolytes (Figure 1.1). Operating at these unstable potentials produces a solid electrolyte interphase (SEI) which is formed from the decomposition of the electrolyte solvents simultaneously consuming lithium. The SEI results in an irreversible charge/discharge "loss", a lower rate capability and cycle life and diminishes the overall performance of the battery. Therefore, characterizing the properties of the LIB electrode as well as the electrode/electrolyte interface is crucial in the advancement of next-generation LIBs.

Rechargeable batteries were first developed between the mid 1800s and early 1900s by notable scientists Gaston Planté (lead-acid), Waldemar Junger (nickel-cadmium) and Thomas Edison (nickel-iron).[5] Nickel-metal hydride and high-temperature sodium and lithium batteries preceded commercialization of LIBs which had its break-through in 1991 when Sony exchanged the lithium metal anode for graphite.[5] Since then,

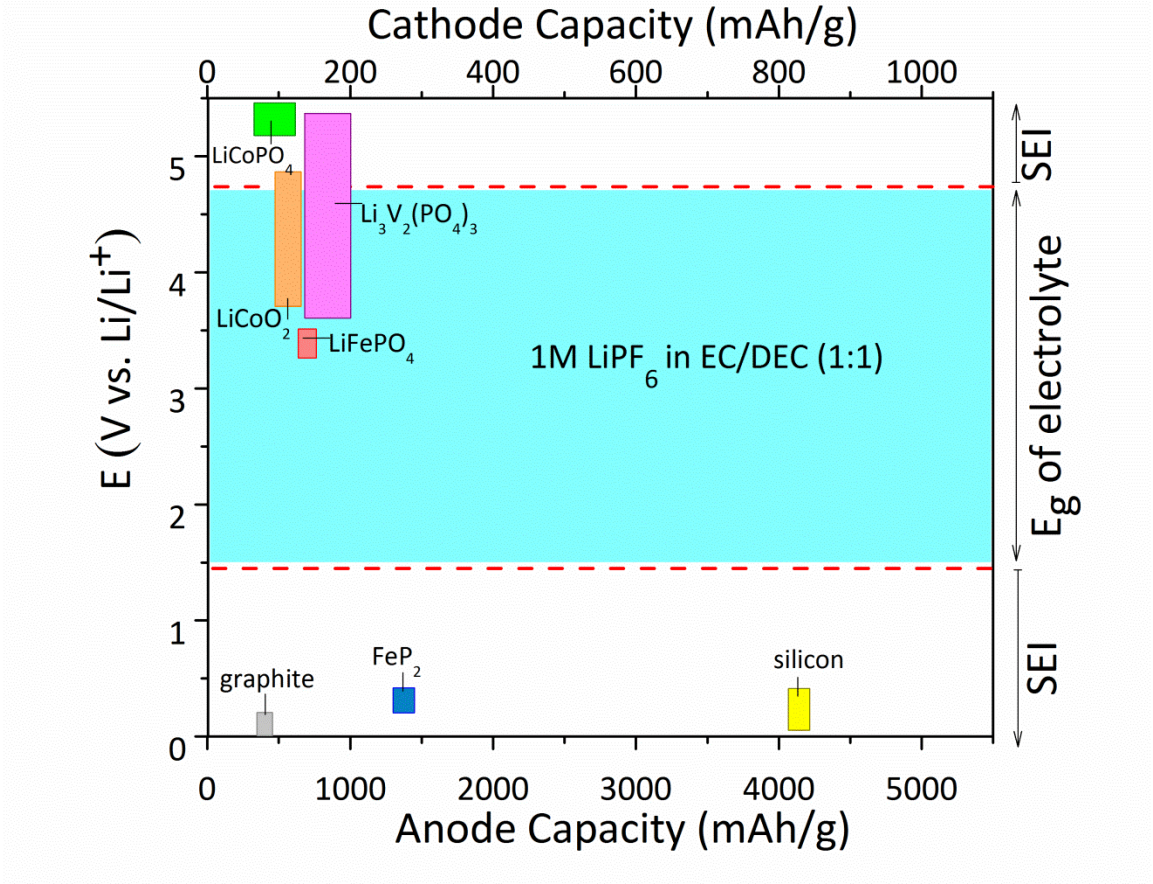

Figure 1.1 Voltage versus capacity of various cathode and anode electrodes relative to the window of the $LiPF_6$ EC:DEC electrolyte. The electrodes that operate outside of the window of the electrolyte develop an SEI.

graphite remains to be the standard anode and multiple cathodes have been used depending on the application (Figure 1.1).

LIBs consist of two dissimilar electrodes (anode and cathode) separated by an ionic conductor (electrolyte) while electrically connected through an external circuit.[6] The cathode is usually a lithiated transition-metal oxide (TMO) which becomes oxidized during charging (eq.1). In parallel to this reaction the anode, usually graphite, gets reduced (eq. 2).[7] The electrons generated go through the external circuit to do work.

$$LiMO \leftrightharpoons xLi^+ + xe^- + Li_{1-x}MO \quad (1)$$

$$C_6 + Li^+ + e^- \leftrightharpoons LiC_6 \quad (2)$$

Equations 1 and 2 are examples of intercalation reactions for LIBs. The intercalation mechanism for LIBs was a natural result of the extensive studies in the 1970s on electrically conductive hosts that could insert electroactive species.[8,9] Crystalline materials with layers in their lattices allow for the intercalation of lithium ions without changing the crystal structure. In LIBs the anode and cathode are both intercalation hosts. Lithium ions shuttle back and forth between the two electrodes, hence the term "shuttle mechanism". The reversibility of these reactions is dependent on the stability of the crystalline structures for both electrodes during the intercalation/deintercalation process. Ideally, these types of electrodes should be able to intercalate multiple lithium ions at potentials that are within the electrochemical window of LIBs for many cycles without a significant change in volume.

Also of vital importance to the operation of LIBs is the electrolyte employed. For the past two decades the most widely adopted electrolyte has been based on alkyl carbonates. The electrolyte contains a lithium salt with two alkyl carbonate solvents in order to meet the many criteria demanded by LIBs. These requirements include a high dielectric constant (high solubility of lithium salts), low viscosity (fast lithium ion

diffusion rates), inert on charged anode and cathode surfaces during operation and stability as a liquid in a wide temperature range.[10,11] Of the alkyl carbonate electrolytes, $LiPF_6$ in ethylene carbonate (EC) and diethyl carbonate (DEC) has been the popular choice due to its optimal performance. EC, a cyclic alkyl offers low viscosity and DEC, a linear alkyl has a high dielectric constant. Combined, they have a high ionic conductivity. The electrochemical window has been estimated to be ~1.3-4.3 V vs. Li/Li^+.[10]

Since the 1990s, multiple novel cathode materials have been developed. The requirements necessary for cathodes include: a readily oxidizable/reducible ion, reversible reaction with lithium, high capacity and voltage, stable structure, low cost and it must be environmentally benign.[8] Two classes of structures can be found. The first class is the layered compound with an anion close-packed lattice in which alternate layers between the anion sheets are occupied by a transition metal, and in the empty alternate layers lithium inserts itself ($LiCoO_2$[12], $LiTiS_2$[13] and spinel[14]). The second class has more of an open structure (MnO_2, $LiFePO_4$[15] and vanadium oxides[16]).[8] Although the first class is more compact and contains an advantage in terms of energy stored per unit volume the second class of structures could potentially be of lower cost. Individually, these materials have their own challenges and limitations which are beyond the scope of this dissertation. For this dissertation the focus will be on the $Li_3V_2(PO_4)_3$ cathode which is in the family of transition metal phosphates (TMPs).

Transition metal phosphates (TMPs) are based on abundant, cheap and non-toxic elements. The covalent bonding in the phosphate anion also makes it a more thermally and chemically stable structure.[15,17] The olivine phase of the TMPs has been heavily studied, predominantly $LiFePO_4$, which has a discharge potential of 3.4 V vs. Li/Li^+, fitting within the limits of alkyl carbonate electrolytes. However, a drawback for $LiFePO_4$

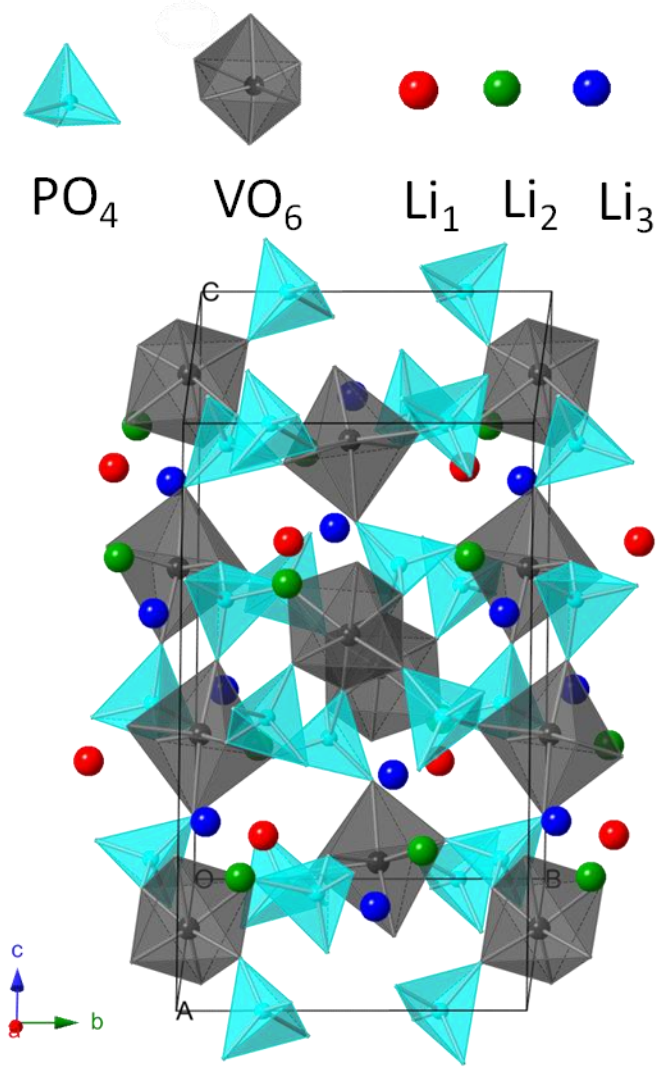

Figure 1.2 Crystal structure of monoclinic (α) $Li_3V_2(PO_4)_3$. The PO_4 tetrahedra are in cyan. The VO_6 octahedra are in dark grey. The three energetically distinct lithium ions $Li_{1,2,3}$ are depicted in red, green and blue.

as well as other phosphate materials (M-O-P-O-M) is the poor inherent conductivity therefore requiring a conductive carbon coating to obtain reversible lithium intercalation/deintercalation. [15] $VOPO_4$[18] and $Li_3V_2(PO_4)_3$[19] are two vanadium phosphates that are strong candidates for cathode materials.

$Li_3V_2(PO_4)_3$ in its monoclinic phase, as shown in Figure 1.2, has the ability to store up to three lithium ions which are reversibly extractable (eq. 3).

$$Li_3V_2(PO_4)_3 \leftrightharpoons 3Li^+ + 3e^- + V_2(PO_4)_3 \quad (3)$$

The intercalation mechanism is complex due to the multiple two-phase transitions that occur during charging (deintercalation). During reintercalation solid solution behavior is seen from the insertion of 0 to 2 lithium ions followed by two-phase transitions. However, the reversible intercalation/deintercalation of three lithium ions that occurs even at fast cycling rates makes $Li_3V_2(PO_4)_3$ the phosphate with the highest theoretical gravimetric capacity of 197 mAh/g (monoclinic phase).[19]

Most of the recent work published on $Li_3V_2(PO_4)_3$ has focused on developing new synthetic strategies that provide control over the morphology and particle size.[19] The synthetic procedures are based on sol-gel[20], hydrothermal[21], spray pyrolysis chemistry[22], etc. Pure $Li_3V_2(PO_4)_3$ has a low electronic conductivity ~10^{-8} S/cm that is comparable to olivine $LiFePO_4$, but several orders of magnitude lower than most transition metal oxides (~10^{-3}-10^{-4} S/cm).[19] Therefore, great emphasis has been placed on increasing the electronic conductivity of $Li_3V_2(PO_4)_3$ by applying a carbon, metal or metal oxide coating. A simple, solid-state based carbon coating on micron sized $Li_3V_2(PO_4)_3$ particles can result in a seven-order-of-magnitude increase in electronic conductivity. Moreover, theoretical studies show that lithium ions diffuse 1-dimensionally (along the (100) direction) at a sluggish rate of 10^{-11} cm^2s^{-1} in monoclinic $Li_3V_2(PO_4)_3$.[23] Improvements to lithium ion diffusion in $Li_3V_2(PO_4)_3$ have been made through nanostructured particles

which offer shorter path lengths for lithium ion diffusion and higher electrical conductivity, thus offering higher charge-discharge rates. Several carbon coated, nano-architectures have been devised including nanospheres[24], nanobelts,[25] nanofibers[26], nanoplates[27] etc. that give reasonable capacities (~103 mAh/g) at the high rate of 100 C (A C rate is defined as the rate at which a battery is discharged relative to its maximum capacity. A 1 C rate means that the battery will entirely discharge in 1 hr). But the higher volume-to-surface-area, which increases the electrode/electrolyte interface and is beneficial to the conductivity of the particles, can also be detrimental to its intercalation properties. When operating at voltages outside of the stability window of the electrolyte as is the case for $Li_3V_2(PO_4)_3$, oxidatively decomposed species can react with the surface of the electrode. In order for all three lithium ions to be intercalated/deintercalated from the monoclinic structure a 4.8 V vs. Li/Li^+ charging potential must be applied. As was mentioned above, the stability window of the common, alkly carbonate electrolytes has an upper limit of ~4.3 V vs. Li/Li^+. Operating outside of the electrochemical window of the electrolyte could lead to an electrode/electrolyte interfacial film. These surface films greatly affect the lithium intercalation/deintercalation properties of the electrode thus changing the performance of the material. Yet, there is only one report that has investigated the interfacial region of $Li_3V_2(PO_4)_3$.[28] Furthermore, the electrode/electrolyte interface of cathodes, even the most heavily studied TMOs remains controversial due to conflicting proposed mechanisms. Thus far, in situ X-ray diffraction (XRD)[29], X-ray absorption (XAS)[29], and infrared (IR) spectroscopy[30] have shown that the $Li_3V_2(PO_4)_3$ structure reversibly intercalates/deintercalates all three lithium ions after the first cycle. But questions remain about the stability of the structure once fully delithiated at such high charging potentials, especially after multiple cycles. Considering the fact that many groups are developing different coatings on $Li_3V_2(PO_4)_3$ which result in higher capacity

retention it is important to specifically determine what chemical processes are taking place at the interface of the $Li_3V_2(PO_4)_3$ electrode/electrolyte and to determine the stability of the $Li_3V_2(PO_4)_3$ structure at high voltages.[31]

X-ray photoelectron spectroscopy (XPS) is one of the most common techniques used to probe the chemical composition of the electrode/electrolyte interface of LIBs. The technique is based on the photoelectric effect. Soft x-rays are used to irradiate a sample. The photons are absorbed by an atom from the sample (molecule or solid) which ionizes the atom by emission of a core shell electron. A spectrum of the kinetic (or binding) energy distribution of emitted photoelectrons is then obtained. Every peak at a particular energy corresponds to a specific element.[32] Therefore, the specific elements present in the sample can be identified. Additionally, the intensity of the peaks is related to the concentration of the element within the area of analysis. Moreover, a slight shift in the position of a peak that corresponds to a specific element indicates a unique chemical bonding environment of that element. Therefore, XPS allows for the identification of the molecular environment of the sample. Since the probing depth for XPS is about 10 nm it is considered to be a highly surface sensitive technique and therefore very useful for studying the electrode/electrolyte interface.[32] The Texas Materials Institute (TMI) at the University of Texas at Austin developed an ultra-high-vacuum chamber using reduced oxidation interface (RoX) that allows samples to be transported from a glove box to the XPS instrument.[33] This is a large advantage to other analytical techniques for which such interfaces have yet to be developed. In conclusion, XPS is the analytical tool best suited to study the electrode/electrolyte interface of the $Li_3V_2(PO_4)_3$ electrodes because it provides quantitative information about the molecular environment, it is surface sensitive, there is extensive literature of electrode/electrolyte interface chemistry to compare to and the RoX vacuum chamber allows for analysis of the samples under anhydrous and anoxic

conditions. These studies helped to better correlate the surface chemistry of $Li_3V_2(PO_4)_3$ at high operating voltages and its corresponding electrochemical performance.

Raman microscopy was used to study the bulk properties of $Li_3V_2(PO_4)_3$. To understand Raman microscopy as an analytical technique the fundamentals of the Raman effect must first be described. The Raman effect is based on the scattering phenomenon. This occurs when a photon interacts with a molecule in the ground electronic state and becomes excited to a virtual state (lower in energy than the lowest excited electronic state). In the virtual state the photon can scatter without a change in energy (Rayleigh), can lose energy to the molecule (Stokes) or gain energy from the molecule (Anti-Stokes). Most of the photons will undergo Rayleigh scattering (elastic).[32] However, every 1 in 10^7 photons will have a change in energy (inelastic) during scattering resulting in a change in the atomic coordinates of the molecule, called a vibration. Since most molecules are found in the lowest vibrational ground state, Stokes scattering is the more probable event. Therefore, Raman data is plotted as the intensity of the scattered radiation as a function of the Stokes-shifted frequencies in wavenumbers (cm^{-1}). Each peak in the spectrum corresponds to a vibrational energy of the molecule or crystal. Therefore, each molecule or crystal has its own "finger print" spectrum. With Raman spectroscopy structural information about the sample is gained at the level of atomic bonds. Its high sensitivity allows for detection of crystalline and amorphous materials, a huge advantage over diffraction based techniques which require long range order in the structure. With Raman spectroscopy the sample is preserved in its pristine state during analysis because no sample preparation is required. Careful selection of the irradiation source allows for non-destructive analysis of samples.[34] In this dissertation a fundamental investigation is presented on the first theoretical and experimental Raman microscopy spectrum of α-$Li_3V_2(PO_4)_3$. Spectra of $Li_3V_2(PO_4)_3$ after electrochemical cycling is compared to the

pristine spectrum to investigate the reversibility of the material at high charging potentials.

Coupling Raman spectroscopy to a microscope provides additional advantages that are especially useful for LIB materials. The irradiation source can be focused to a small area which is useful when analyzing composite electrodes which are a heterogeneous mixture of active material, binder and conductive carbon. This allows for each individual component to be analyzed and with a confocal Raman microscope set up 2-D and 3-D mapping can be obtained.[34] Strong IR absorbers such as glass are weak Raman scatterers allowing for analysis to be taken in a glass vial. Since the surface and bulk chemistry of LIB materials is highly reactive towards water and oxygen this permits for analysis under anhydrous and anoxic conditions.[34]Moreover, these optically transparent materials facilitate the making of *in situ* devices that allow for spectroelectrochemical measurements of LIBs during operation. A comparison of *ex situ* versus *in situ* Raman microscopy measurements for LIB materials is discussed in this dissertation. The development of a novel *in situ* Raman microscopy test cell is also presented.

The requirements necessary for anode electrodes in LIBs are similar to those for the cathodes (reversible reaction with lithium, high capacity and voltage, stable structure, low cost and environmentally benign). Carbon has been the material of choice because of its light weight and low electrochemical potential.[35] Carbons can be divided into two broad categories: hard (glassy carbon) and soft carbons (graphitic carbon). These two types of materials vary greatly in their physical and chemical properties. Graphite, which has a better ordering of graphene layers, can insert one lithium for every six carbon atoms (LiC_6). This corresponds to a theoretical capacity of 372 mAh/g with a low and flat discharge profile between 0 and 0.3 V.[35] The electrolyte must be carefully selected for

graphite. In propylene carbonate (PC) based electrolytes the PC decomposes at ~0.8 V leading to physical disintegration of graphite, called "exfoliation". Besenhard et al. proposed that exfoliation occurs from co-intercalation of PC and lithium.[36,37] The PC decomposes into gaseous products within the interstitial region resulting in structural strain that breaks the weak Van der Waals forces between the graphene sheets. The process is irreversible and prevents lithium from intercalating into the interstitial region. Replacing the PC based electrolyte with EC and DEC solvents results in a compact and protective surface film called the solid electrolyte interphase (SEI) preventing co-intercalation or any exfoliation. The hard carbons have a higher capacity than graphite but the discharge profile has a slope like plateau between 0 and 1 V, which results in a slightly lower cell voltage as compared to graphite. To improve performance of carbon anodes structural modifications have been made such as incorporation of B, O ,Si and P, texture control and slight oxidation.[35]

A prospective anode that could potentially circumvent the initial irreversible capacity experienced by carbon is $Li_4Ti_5O_{12}$. The cubic spinel structure accommodates three more lithium ions per formula unit with a negligible change in volume at a flat discharge voltage around 1.5 V.[38] But both the higher discharge voltage and lower capacity as compared to carbon make it an unsuitable competitor. Metals and semimetals that are reactive towards lithium through an alloying process also have been investigated.[39] Unlike intercalation materials, alloying materials can achieve an extremely high capacity by withstanding major structural changes and exchange multiple electrons during the redox reaction. As an example, silicon theoretically has a capacity of 3590 mAh/g as compared to 372 mAh/g for graphite.[39] These alloying reactions have proven difficult to make reversible as the alloying/de-alloying process introduces large strains in the particles of the active material and composite electrode. Significant capacity loss is

noted and attributed to a progressive decohesion and shuffling of the particles. Modifying the binder and active material ratio to circumvent these failure processes has alleviated some of the capacity drop for these materials but at the cost of electrode capacity.

Another novel reaction of high interest involves the reaction between lithium and a transition metal anion to form metal nanoparticles immersed in a lithium anion matrix (eq. 4).[40]

$$M_aX_b + (b \cdot n)Li \leftrightharpoons aM + bLi_nX \quad (4)$$

This reaction is formally referred to as the conversion reaction. Several binary compounds (M-X, X = O, N, F, S, P and H) have already proven to undergo the conversion reaction. The metal nanoparticles produced become embedded in the lithium binary matrix creating a high interfacial surface that facilitates the reversibility of the reaction (Figure 1.3). Because the redox center can lie on bands that have a strong anion contribution the transition metal and anionic species can be selected so as to fine tune the redox potential. Many challenges must still be overcome before this lithiation reaction is considered a particle alternative to intercalation chemistry. As noted in the alloying reactions, particle decohesion occurs in conversion reactions from the large volume changes that take place during the structural reorganization. There is also a large voltage hysteresis that is observed between the charging and discharging process (loss in energy density). This is coupled with a large coulombic inefficiency in the first cycle.[40]

Of the binary compounds, transition metal oxides have been the most thoroughly characterized. Experimentally, oxides based on Cr, Mn, Fe, Co, Ni, Cu, Mo, W and Ru have all proven to undergo the conversion reaction with lithium. Group 4 and 5 transition metals have not. The redox potentials for some of the oxides are as low as 0.2 V vs. Li/Li^+ (ex: Cr_2O_3, Mn_2O_3).[40] In addition, these multi-electron reactions offer double and sometimes even triple the specific gravimetric capacities that can be achieved with

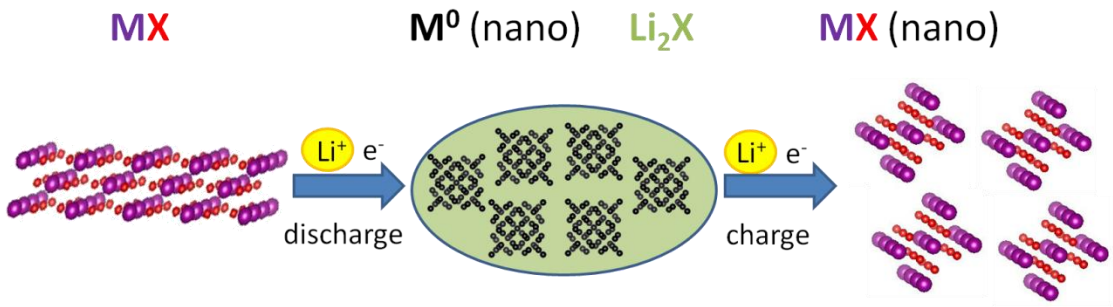

Figure 1.3 Schematic representations of the discharge and charge reactions for conversion materials. MX represents the bulk, crystalline binary compound. M^0 represents the metallic nanoparticles immersed in the Li_2X matrix formed during discharging. MX (nano) represents the nano, amorphous binary compound that is reformed during the charging process.

intercalation based anodes. Ideally, these compounds should be based off cheap and abundant transition metals. Binary, transition metal sulfides, nitrides and fluorides undergo the conversion reaction at higher potentials than the oxides which make them impractical as anodes. However, the binary transition metal phosphide (BTMPs) compounds operate at a low enough potential to be competitive with the carbon anode discharge potential.[40]

There are very few reports on the conversion reaction of iron phosphides, FeP_y. Recent studies have shown that the iron rich phases (y = 0.33, 0.5) do not show any redox activity with lithium.[41] However, the phosphide rich phases (FeP, FeP_2) directly convert to Li_3P and Fe nanoparticles yielding initial capacities of 720 and 1300 mAh/g.[42–44] In these materials the high covalency between the iron and phosphorous permits electron transfer to occur into bands that have a strong phosphide contribution. Yet, extended reversibility for the conversion reaction of both FeP and FeP_2 has not been achieved. The limited studies on iron phosphides have solely focused on the bulk, crystalline phase.

The electrochemical mechanism by which the conversion reaction takes place often involves an intermediate phase, Li-M-X.[40] In BTMPs extensive lithium insertion occurs before conversion to Li_3P and metal nanoparticles. The intermediate reactions suggest that the formation of the metal nanoparticles is not energetically favorable. One of the defining electrochemical characteristics of these reactions is the large voltage hysteresis between the charge and discharge process. This is largely attributed to the difference in Gibbs free energy between the initial bulk, crystalline binary reactant and the final nano, amorphous metallic product immersed in the Li_nX matrix. Moreover, for some of these conversion electrodes it has been found that the intermediate phase formed upon the conversion reaction is not reformed upon deconversion.[40] One example of this is FeF_3 which forms $Li_x[Fe^{3+}_{1-x}Fe^{2+}_x]F_3$ before complete reduction to LiF and Fe. The

reverse reaction forms a different intermediate, $Li_{3-3x}Fe_xF_3$, before reforming to FeF_3 upon oxidation.[45] The different reaction pathways of conversion (reduction) and deconversion (oxidation) result in differing equilibrium potentials. More importantly, it is apparent that we do not have a clear understanding of the conversion/deconversion mechanism. Understanding the mechanism is essential in developing strategies to combat the voltage hysteresis that causes a large overall energy penalty in this type of lithiation chemistry. Beyond the first conversion/deconversion reaction the voltage hysteresis is greatly diminished partly because the amorphous character of the sample does not change beyond the first cycle. Yet, there is still a significant hysteresis that remains constant with further cycling. Unaccounted processes that are contributing to this continuous hysteresis msut be investigated. Other challenges faced by the conversion reaction include a large coulombic inefficiency during the first cycle and low capacity retention with further cycling. The greatest challenge remains to be the large voltage hysteresis during the conversion/deconversion. Without a thorough understanding of its origins it will be impossible to minimize thus, preventing further developments of these types of battery materials.

A common strategy to improve performance in binary conversion materials is to engineer these materials into nanoparticles. Nanoparticles offer the obvious advantage of a shorter lithium diffusion path which enhances initial capacity and rate capability. The nanostructure could also alleviate textural formatting during the first cycle. Furthermore, a nano, amorphous structure would better match the Gibbs free energy of the nano, amorphous products (M^0, Li_nX), potentially reducing the problematic voltage hysteresis. There are limited synthetic strategies that offer control in the size and morphology of these materials. Richard A. Jones and coworkers devised a simple, clean and energy efficient (low temperature) strategy for synthesizing nano, amorphous BTMPs (M = Ti,

Mo, Ni, Fe).[46] The scarce reports on FeP_2 motivated a collaborative project between our group and that of Prof. Jones to synthesize nano, amorphous FeP_2 to gain insight on the effects of this new morphology (nano, amorphous) and its electrochemical performance.

This dissertation is divided into five chapters. In this first chapter some of the general lithiation mechanisms that are currently known for LIBs (intercalation, alloying, conversion) have been discussed. A short account of some of the common cathodes and anodes that have been studied to date are reported. Lastly, a general introduction to $Li_3V_2(PO_4)_3$ as an intercalation cathode and FeP_2 as a conversion anode is given.

The second chapter discusses the electrochemical lithiation of nano, amorphous FeP_2 synthesized via a novel, low-temperature reaction between $Fe(N(SiMe_3)_2)_3$ and PH_3 gas in THF. A reaction that can be generalized for any σ-bonded alkyl of the d-block transition metals with PH_3 gas at room temperature. From various characterization techniques (XPS, X-ray diffraction (XRD), scanning electron microscopy (SEM), elemental analysis) the product was confirmed to be the kinetically stabilized nano, amorphous phase of FeP_2. Gravimetric capacities are presented from galvanostatic lithiation/delithiation experiments with extended cycling. As compared to reports on bulk, crystalline FeP_2 this nano, amorphous material has a greater retention of the gravimetric capacity and a diminished voltage hysteresis. Based on galvanostatic cycling studies, the lithiation mechanism proposed for nano, amorphous FeP_2 can be defined as a competition between traditional lithium ion intercalation/deintercalation and a possible conversion reaction. Lastly, the deleterious reaction between nano, amorphous FeP_2 in the presence of air is discussed and its electrochemical performance compared to the material prepared and tested under anoxic/anhydrous conditions.[46]

The third chapter discusses characterization of $Li_3V_2(PO_4)_3$ via Raman microscopy which is compared to the theoretical spectrum calculated by density

functional theory (DFT) (in collaboration with Graeme Henkelman and co workers). Thermal effects from the laser on the monoclinic phase of $Li_3V_2(PO_4)_3$ was determined via *in situ* Raman microscopy at elevated temperatures under different atmospheres (air, N_2, O_2). Thermal measurements (differential scanning calorimety (DSC) and thermal gravimetric analysis (TGA)) were acquired to confirm the in situ measurements.[47] The fourth chapter reports on the interfacial chemistry between a composite $Li_3V_2(PO_4)_3$ electrode and an alkyl carbonate electrolyte ($LiPF_6$ EC/DEC) at a high and stable charging potential (4.8 V and 4.2 V vs. Li/Li^+) where different electrochemical performance is noted. Additionally, the interface between the composite $Li_3V_2(PO_4)_3$ electrode and electrolyte after aging was investigated. X-ray phototelectron spectroscopy measurements under anoxic and anhydrous conditions revealed similar chemical species on the surface of the composite $Li_3V_2(PO_4)_3$ cathode after being charged at both potentials and after aging. Analogous experiments on the individual constituents of the composite electrode are reported. The role of the carbon black additive on the formation of the solid electrolyte interphase (SEI) on $Li_3V_2(PO_4)_3$ composite electrodes is explained.

The fifth and final chapter reports on the development of a novel *in situ* Raman microscopy test cell for LIBs. The pertinent components and design criteria necessary for optimal electrochemical and Raman scattering measurements is identified.[34] A composite $LiFePO_4$ electrode is tested in this novel *in situ* Raman microscopy test cell and compared to previous in situ Raman microscopy measurements made in our group on a different, non-optimal design.[48] Finally, some improvements are suggested for a more advanced and/or specialized in situ Raman microscopy test cell. *In situ* experiments are proposed for $Li_3V_2(PO_4)_3$ and other LIB materials.

1.2 REFERENCES

(1) Wigley, T. M. L.; Raper, S. C. B. *Science* **2001**, *293* (5529), 451.

(2) Winter, M.; Brodd, R. J. *Chem. Rev.* **2004**, *104* (10), 4245.

(3) Karden, E.; Shinn, P.; Bostock, P.; Cunningham, J.; Schoultz, E.; Kok, D. *Sel. Pap. Ninth Eur. Lead Battery Conf. Ninth Eur. Lead Battery Conf.* **2005**, *144* (2), 505.

(4) Armand, M.; Tarascon, J.-M. *Nature* **2008**, *451* (7179), 652.

(5) Thackeray, M. M.; Wolverton, C.; Isaacs, E. D. *Energy Environ. Sci.* **2012**, *5* (7), 7854.

(6) Tarascon, J.-M.; Armand, M. *Nature* **2001**, *414* (6861), 359.

(7) Etacheri, V.; Marom, R.; Elazari, R.; Salitra, G.; Aurbach, D. *Energy Environ. Sci.* **2011**, *4* (9), 3243.

(8) Whittingham, M. S. *Chem. Rev.* **2004**, *104* (10), 4271.

(9) Whittingham, M. S. *Chem. Rev.* **2014**, *114* (23), 11414.

(10) Goodenough, J. B.; Kim, Y. *Chem. Mater.* **2010**, *22* (3), 587.

(11) Xu, K. *Chem. Rev.* **2004**, *104* (10), 4303.

(12) Okubo, M.; Hosono, E.; Kim, J.; Enomoto, M.; Kojima, N.; Kudo, T.; Zhou, H.; Honma, I. *J. Am. Chem. Soc.* **2007**, *129* (23), 7444.

(13) Yersak, T. A.; Yan, Y.; Stoldt, C.; Lee, S.-H. *ECS Electrochem. Lett.* **2012**, *1* (1), A21.

(14) Liu, D.; Zhu, W.; Trottier, J.; Gagnon, C.; Barray, F.; Guerfi, A.; Mauger, A.; Groult, H.; Julien, C. M.; Goodenough, J. B.; Zaghib, K. *RSC Adv.* **2014**, *4* (1), 154.

(15) Yuan, L.-X.; Wang, Z.-H.; Zhang, W.-X.; Hu, X.-L.; Chen, J.-T.; Huang, Y.-H.; Goodenough, J. B. *Energy Environ. Sci.* **2011**, *4* (2), 269.

(16) Watanabe, T.; Ikeda, Y.; Ono, T.; Hibino, M.; Hosoda, M.; Sakai, K.; Kudo, T. *Proc. Second Int. Symp. Soft Solut. Process. 2000* **2002**, *151* (1–4), 313.

(17) Jiajun, C. *Materials* **2013**, *6* (1), 156.

(18) Harrison, K. L.; Bridges, C. A.; Segre, C. U.; Varnado, C. D.; Applestone, D.; Bielawski, C. W.; Paranthaman, M. P.; Manthiram, A. *Chem. Mater.* **2014**, *26* (12), 3849.

(19) Rui, X.; Yan, Q.; Skyllas-Kazacos, M.; Lim, T. M. *J. Power Sources* **2014**, *258* (0), 19.

(20) Jiang, T.; Pan, W.; Wang, J.; Bie, X.; Du, F.; Wei, Y.; Wang, C.; Chen, G. *Electrochimica Acta* **2010**, *55* (12), 3864.

(21) Qiao, Y. Q.; Tu, J. P.; Xiang, J. Y.; Wang, X. L.; Mai, Y. J.; Zhang, D.; Liu, W. L. *Electrochimica Acta* **2011**, *56* (11), 4139.

(22) Ko, Y. N.; Koo, H. Y.; Kim, J. H.; Yi, J. H.; Kang, Y. C.; Lee, J.-H. *15th Int. Meet. Lithium Batter. IMLB* **2011**, *196* (16), 6682.

(23) Lee, S.; Park, S. S. *J. Phys. Chem. C* **2012**, *116* (48), 25190.

(24) Mai, L.; Li, S.; Dong, Y.; Zhao, Y.; Luo, Y.; Xu, H. *Nanoscale* **2013**, *5* (11), 4864.

(25) Pan, A.; Choi, D.; Zhang, J.-G.; Liang, S.; Cao, G.; Nie, Z.; Arey, B. W.; Liu, J. *J. Power Sources* **2011**, *196* (7), 3646.

(26) Chen, Q.; Zhang, T.; Qiao, X.; Li, D.; Yang, J. *J. Power Sources* **2013**, *234* (0), 197.

(27) Qiao, Y. Q.; Wang, X. L.; Mai, Y. J.; Xiang, J. Y.; Zhang, D.; Gu, C. D.; Tu, J. P. *J. Power Sources* **2011**, *196* (20), 8706.

(28) Chen, Y.; Zhang, D.; Bian, X.; Bie, X.; Wang, C.; Du, F.; Jang, M.; Chen, G.; Wei, Y. *Electrochimica Acta* **2012**, *79* (0), 95.

(29) Yoon, J.; Muhammad, S.; Jang, D.; Sivakumar, N.; Kim, J.; Jang, W.-H.; Lee, Y.-S.; Park, Y.-U.; Kang, K.; Yoon, W.-S. *J. Alloys Compd.* **2013**, *569* (0), 76.

(30) Burba, C. M.; Frech, R. *Solid State Ion.* **2007**, *177* (39–40), 3445.

(31) Zhang, L.-L.; Liang, G.; Peng, G.; Zou, F.; Huang, Y.-H.; Croft, M. C.; Ignatov, A. *J. Phys. Chem. C* **2012**, *116* (23), 12401.

(32) Skoog, D. A.; Holler, J.; Crouch, S. R. *Principles of Instrumental Analysis*, 6th ed.; Cengage Learning: Boston, 2006.

(33) Schroder, K. W.; Celio, H.; Webb, L. J.; Stevenson, K. J. *J. Phys. Chem. C* **2012**, *116* (37), 19737.

(34) Baddour-Hadjean, R.; Pereira-Ramos, J.-P. *Chem Rev* **2009**, *110* (3), 1278.

(35) Arumugam Manthiram. In *Battery Applications*; The University of Texas at Austin; pp 68–82.

(36) Besenhard, J. O. *Carbon* **1976**, *14* (2), 111.

(37) Besenhard, J. O.; Fritz, H. P. *Angew. Chem. Int. Ed. Engl.* **1983**, *22* (12), 950.

(38) Aldon, L.; Kubiak, P.; Womes, M.; Jumas, J. C.; Olivier-Fourcade, J.; Tirado, J. L.; Corredor, J. I.; Pérez Vicente, C. *Chem. Mater.* **2004**, *16* (26), 5721.

(39) McDowell, M. T.; Lee, S. W.; Nix, W. D.; Cui, Y. *Adv. Mater.* **2013**, *25* (36), 4966.

(40) Cabana, J.; Monconduit, L.; Larcher, D.; Palacín, M. R. *Adv. Mater.* **2010**, *22* (35), E170.

(41) Bernardi, J. *Ph. D. Thesis dissertation*; University of Montpellier: Montpellier, France, 2008.

(42) Boyanov, S.; Bernardi, J.; Gillot, F.; Dupont, L.; Womes, M.; Tarascon, J.-M.; Monconduit, L.; Doublet, M.-L. *Chem. Mater.* **2006**, *18* (15), 3531.

(43) Boyanov, S.; Womes, M.; Monconduit, L.; Zitoun, D. *Chem. Mater.* **2009**, *21* (15), 3684.

(44) Silva, D. C. C.; Crosnier, O.; Ouvrard, G.; Greedan, J.; Safa-Sefat, A.; Nazar, L. F. *Electrochem. Solid-State Lett.* **2003**, *6* (8), A162.

(45) Doe, R. E.; Persson, K. A.; Meng, Y. S.; Ceder, G. *Chem. Mater.* **2008**, *20* (16), 5274.

(46) Hall, J. W.; Membreno, N.; Wu, J.; Celio, H.; Jones, R. A.; Stevenson, K. J. *J. Am. Chem. Soc.* **2012**, *134* (12), 5532.

(47) Membreño, N.; Xiao, P.; Park, K.-S.; Goodenough, J. B.; Henkelman, G.; Stevenson, K. J. *J. Phys. Chem. C* **2013**, *117* (23), 11994.

(48) Wu, J.; Dathar, G.K.P.; Sun, C.; Theivanayagam, M.G.; Applestone, D.; Dylla, A.G.; Manthiram, A.; Goodenough, J.B.; Stevenson, K.J. *Nanotechnology* **2013**, *24* (42), 424009/1.

CHAPTER 2[1]

Low-Temperature Synthesis of Amorphous FeP_2 and Its Use as Anodes for Li Ion Batteries

2.1 INTRODUCTION

Lithium ion batteries are currently used in small appliances such as cell phones and laptop computers and are the most promising power source for plug-in hybrid electric vehicles (PHEVs) and electric vehicles (EVs).[1a,b] These modes of transportation have the potential to greatly reduce CO_2 emissions and to reduce our dependence on foreign oil. Lithium ion battery cathode materials that meet many of the requirements for utilization in PHEVs and EVs, including high charge and discharge rates, have been discovered.[1c,d] Lithiated graphite is currently the most widely used anode, although considerable improvements in safety, cost and weight are sought as well as materials with higher capacity and higher power in order to realize the full potential of PHEVs and EVs.[2-4]

Anode materials based on inexpensive, binary, transition-metal phosphides (BTMPs) offer great promise for lithium ion batteries because of their exceptionally high gravimetric storage capacities relative to conventional lithium ion carbon anode materials. However, lithium ion-coupled charge transfer reactions in BTMPs induce large irreversible volume changes in excess of 300% due to the formation of Li_xM, Li_xP, M^0 phases. This can facilitate failure processes including aggregation and pulverization as well as loss of electrical contact between the active material and current collector (support). While such a drastic volume change cannot be alleviated completely, the magnitude of the volume change can be reduced by the use of BTMPs with a more

[1] Reprinted with permission from Hall, J. W.; Membreño, N.; Wu, J.; Celio, H.; Jones, R. A.; Stevenson, K. J. *J. Am. Chem. Soc.* **2012**, *134*, 5532. Copyright 2012 American Chemical Society. Justin Hall contributed to the project by synthesizing the FeP_2 nanoparticles. Hugo Celio assisted with XPS experiments. Jing Wu conducted preliminary electrochemistry experiments. Richard Jones supervised the synthesis of FeP_2. Keith Stevenson supervised the characterization of FeP_2.

optimized nanostructure and porous or layered architecture.[5-7] Of the BTMP materials studied to date, FeP, FeP_2, and FeP_4 are attractive because they are based on inexpensive iron. The theoretical full conversion capacities of FeP, FeP_2 and FeP_4 are 926, 1365 and 1789 mAh/g, respectively, all of which are considerably greater than that of the traditional graphite anode (372 mAh/g).

Current methods of preparing nanosized particles of BTMPs typically employ arrested precipitation or solvothermal routes, both of which require relatively high temperatures. For the late transition metals, pioneering studies by Brock[10] and Schaak[11] on the synthesis of nanosized BTMPs have been focused on the use of trioctylphosphine (TOP) and trioctylphosphineoxide (TOPO) at temperatures generally in the range of 200 - 300 °C.[12-18] In addition, Brock[10h] has also demonstrated that desilylation could be used to produce FeP nanoparticles at 240 - 300 °C. These high temperature routes to BTMPs, in most cases, provide the most thermodynamically stable, well known, crystalline phase of the material. In contrast, we have discovered that σ-bonded metal alkyls[19] or dialkylamide derivatives[20] of the d-block transition metals react readily with PH_3 at room temperature or slightly elevated temperatures to give kinetically stabilized amorphous or nanocrystalline phases of BTMPs in high yields.[21] We have to date prepared amorphous phosphides of Ti, Mo, Fe, Mn and Ni by this method. The phosphides of Ti, Mo, Mn and Ni, will be reported separately.

Since the main byproduct from these reactions (eq. 1 and 2) are alkanes or secondary amines, this process represents a relatively clean and simple method of producing these materials.

$$MR_x + y\,PH_3 \rightarrow MP_y + x\,RH \quad (1)$$

$$M(NR_2)_x + y\,PH_3 \rightarrow MP_y + x\,HNR_2 \quad (2)$$

Thus, the reaction of the mononuclear Fe amide $Fe(N(SiMe_3)_2)_3$ with PH_3 in THF solution produces a black, air-sensitive powder.[22,23]

2.2 Experimental Section

2.2.1 General Experimental Information

All manipulations were carried out under inert atmosphere with the rigorous exclusion of air and moisture. Iron(III) chloride and lithium bis(trimethylsilyl)amide were purchased from Sigma-Aldrich and used without further purification. Tetrahydrofuran and hexanes were purchased from Fischer Scientific and distilled from Na/benzophenone prior to use. Fourier transform infrared (FTIR) spectroscopy analysis was performed on a Thermo Nicolet Avatar 330 spectrometer. Powder X-ray diffraction (PXRD) analysis was performed on a Bruker D8 diffractometer equipped with a Ge monochromated Cu K_α.source. Scanning electron microscopy (SEM) images were collected with a Zeiss Supra 40 VP scanning electron microscope.

2.2.2 Synthesis of Amorphous FeP_2

A solution of $Fe(N(SiMe_3)_2)_3$ (5.20 g, 9.68 mmol) in THF (100 mL) was treated with PH_3 (25 PSI) in a Fischer-Porter bottle (12 oz.) and the reaction mixture heated at 100 °C while stirring (2 h). The mixture was allowed to cool to room temperature and unreacted PH_3 removed under vacuum. The product was isolated as a black powder via centrifugation. It was washed twice with THF and dried under vacuum. Yield: 1.04 g (91%).

2.2.3 Electrochemical Characterization

Electrochemical performance of FeP_2 was tested using the standard CR2032 coin cell. The cathode was made from a mixture of 75 wt% FeP_2, 15 wt% Super P ® Li and 10

wt% Polytetrafluoroethylene (PTFE) that was dissolved in 7 drops of amyl acetate and rolled into a thin sheet from which circular pellets of usually 5 mg were punched, in a glovebox under argon. Coin cells were assembled with lithium metal as the anode and Celgard® as the separator saturated in 1M $LiPF_6$ in 1:1 ethylene carbonate (EC)/ diethyl carbonate (DEC) as the electrolyte. The cells were set to rest for 6 hours before electrochemical testing to ensure complete absorption of electrolyte into the electrode. Discharge/charge experiments were then carried out on a Arbin BT2000 battery tester at a rate of 0.1 C with a potential window between 2.0 and 0.25 V versus Li/Li^+.

2.2.4 XPS Analysis

All X-ray photoelectron (XPS) spectra were obtained using a Kratos AXIS Ultra spectrometer equipped with a monochromatized Al Kα source, hybrid optics, and a delay line detector coupled to a hemispherical analyzer. The analysis chamber base pressure was typically 2×10^{-9} Torr. All spectra were recorded using a single sweep with a spot size of 300 μm x 700 μm. Survey scans were collected from 0–1200 eV with a pass energy of 80 eV, step size of 1 eV, and a dwell time of 250 ms. The high resolution component spectra were collected with a pass energy of 20 eV, step size of 0.1 eV, and a dwell time of 4000 ms. All binding energies were referenced to the adventitious carbon line (C 1s, 284.8 eV) and charge neutralization was applied during all acquisitions. All samples were prepared in a nitrogen filled glove box and transported directly to the spectrometer using a dedicated interface for transporting air sensitive samples built at the Surface Analysis Laboratory of the Texas Materials Institute (TMI) at UT-Austin. The design of the interface contains a set of built-in figures of merit that were used to verify that samples were not exposed to traces of oxygen and water during transport. Details of the design of the interface will be published elsewhere.[24] Casa XPS analysis software was

used for stoichiometry determination of the samples and Kratos sensitivity factors used for each element of interest.

Surface analysis of the as prepared active material by XPS was consistent with the formation of an iron phosphide[25-28] (Fe $2p_{3/2}$ BE = 707.8 eV, P $2p_{3/2}$ BE = 129.4 eV). In addition, surface oxidation was observed as previously reported for bulk FeP_2[29], with broad peaks of slightly higher binding energy in both the Fe 2p and P 2p regions (Fe $2p_{3/2}$ BE = 710.0 eV, P 2p BE = 133.1 eV) as well as the presence of an intense O 1s peak (O 1s BE = 531.7 eV). The observed surface phosphorous to iron ratio was 6.88:1 for total atomic content, with 5.33:1 for the components assignable to the iron phosphide (Table 2.1).

2.2.5 Elemental Analysis

The Fe:P ratio of the bulk material was determined slowly adding concentrated aqua regia (1 mL) to an ampule containing the iron phosphide (0.3024 g) in a liquid nitrogen bath. The ampule was sealed via rotoflow valve and allowed to warm slowly to room temperature. The ampule was again submerged in liquid nitrogen and an additional aliquot of aqua regia (1 mL) added. After slowly warming to room temperature, the excess gas pressure was carefully released. The sample solution was analyzed via inductively coupled plasma optical emission spectroscopy (ICP-OES) (Applied Analytical Inc., Austin Texas).

2.3 Results and Discussion

Preliminary SEM data revealed that the product from the reaction of mononuclear Fe amide $Fe(N(SiMe_3)_2)_3$ with PH_3 is an aggregate material with particles ranging from 10 to 50 nm in size (Figure 2.1) and no diffraction peaks were observed in the PXRD pattern. Microanalytical data established the Fe:P ratio as 1:1.99. Peaks that

Table 2.1 Observed binding energies for Fe 2p, P 2p, and O 1s components from XPS analysis of unexposed amorphous FeP_2.

Component	Binding Energy (eV)
Fe $2p_{3/2}$ (Fe-P)	707.8
Fe $2p_{1/2}$ (Fe-P)	720.1
Fe $2p_{3/2}$ (Fe-PO)	710.0
Fe $2p_{1/2}$ (Fe-PO)	723.4
P $2p_{3/2}$ (Fe-P)	129.4
P $2p_{1/2}$ (Fe-P)	130.4
P 2p (Fe-PO)	133.1
O 1s	531.7

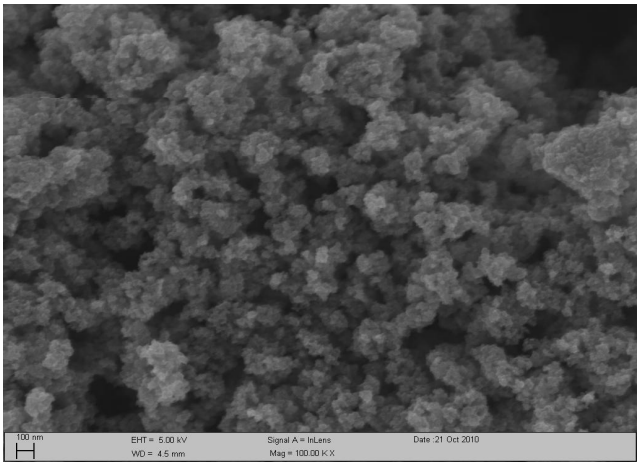

Figure 2.1 SEM image of amorphous FeP_2 synthesized at low temperature.

could be assigned to residual P-H or C-H moieties were also absent in the IR spectrum. The surface area, as measured by multipoint Brunauer-Emmett-Teller analysis with N_2, was 140 m^2/g. This material, that did not undergone high-temperature annealing, showed significant promise as an anode material.

Preliminary electrochemical studies showed excellent performance toward lithiation/delithation (Figure 2.2), with gravimetric discharge and charge capacities of 1258 and 766 mAh/g, translating to 61% reversibility on the first cycle (Figure 2.3). The initial capacity of our material compares favorably with that of crystalline FeP_2 prepared via conventional high-temperature routes.[9a,c] Boyanov et al.[9a] reported that FeP_2 prepared by heating powders of the elements to 973 K for 5 days has an initial capacity of 1000 mAh/g and a capacity loss of 34% during the first cycle, leading to a reversible capacity of 653 mAh/g. A sustained cyclability of 300 mAh/g could be obtained only by limiting the potential window. Ouvrard and co-workers[9c] also reported that FeP_2 prepared using the elements in a tin flux method had an initial capacity of 1365 mAh/g, but did not indicate whether significant capacity was retained upon continuous cycling.[9c]

For our amorphous FeP_2, some of the irreversible capacity loss on the first cycle is associated with the irreversible formation of a solid electrolyte interphase (SEI) layer, as is common for anode materials cycled below 1 V vs Li/Li^+. Although our material demonstrates gradual capacity loss, the cyclability is superior to that in any previous work presented for FeP_2, with 66% retention of the theoretical capacity on the 10^{th} cycle (906 mAh/g).[30] We attribute our better retention to both the amorphous and nanostructural nature of our material, which alleviate the severe mechanical strain upon lithiation/delithiation. In a comparative study between crystalline and amorphous MnO_X

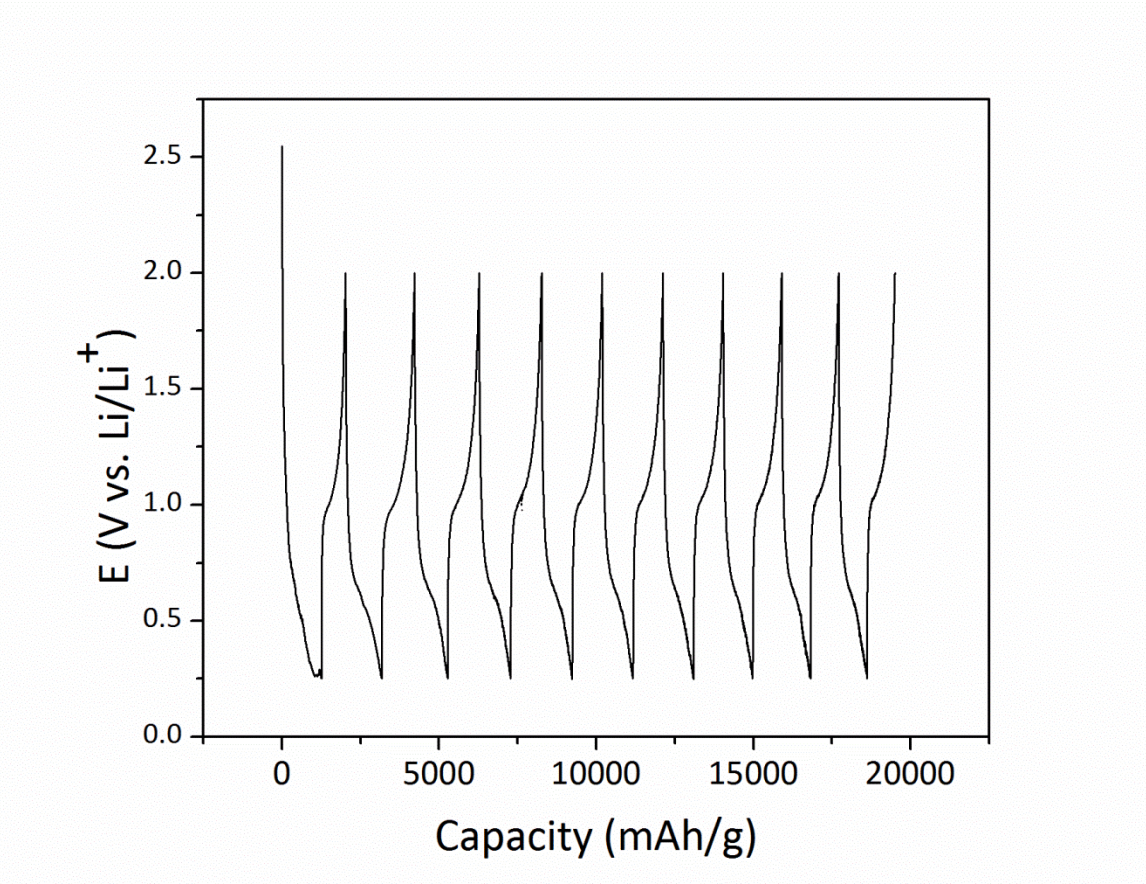

Figure 2.2 Discharge/charge plot of amorphous FeP_2 over 10 cycles at 0.1 C.

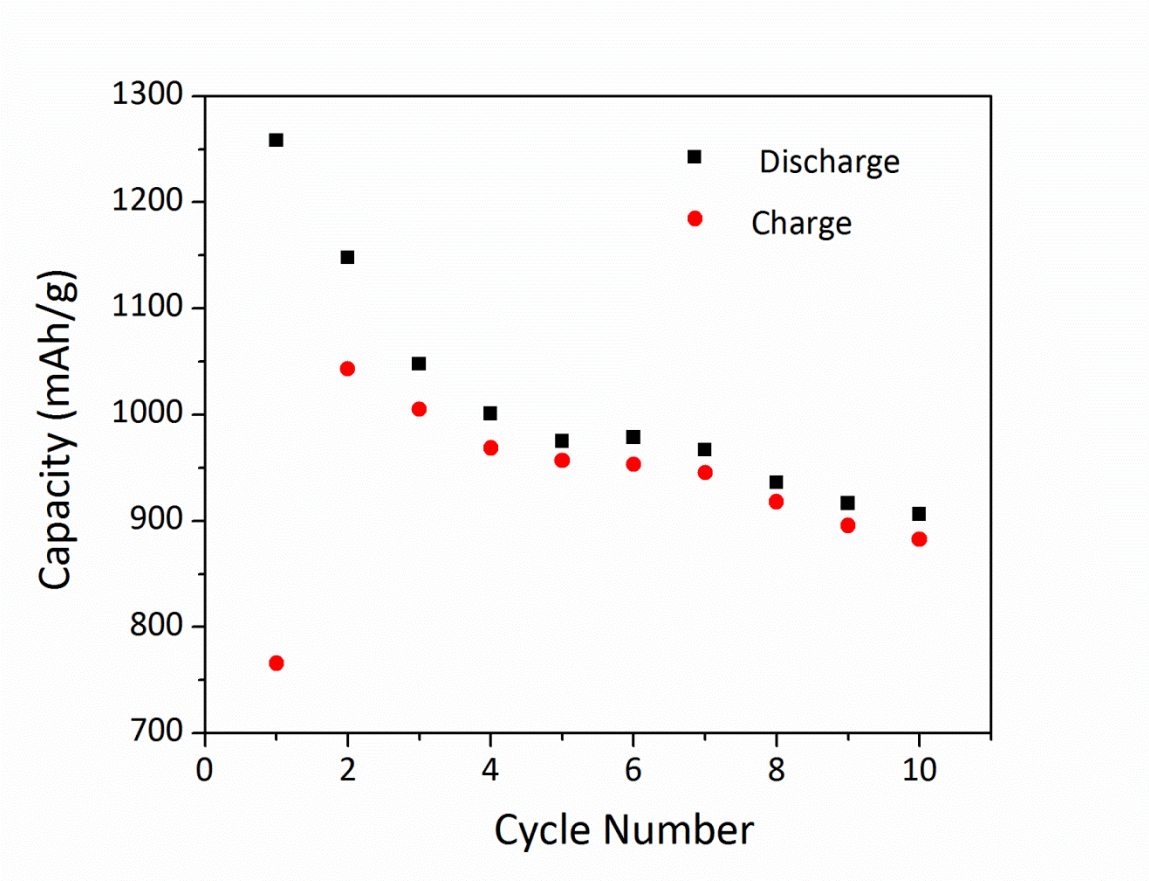

Figure 2.3 Discharge and charge capacities for the first 10 cycles of amorphous FeP_2 at 0.1 C.

nanoparticles, Guo et al.[5b] showed not only that the cycling stability was improved but also that subsequent lithiation potentials (after the first cycle) changed only slightly, confirming the enhanced structural stability of the amorphous material.

Depending on the transition metal, BTMPs can be categorized with two lithiation mechanisms: Li^+ insertion or intercalation,

$$M_yP_n + xLi^+ + xe^- \rightarrow Li_xM_yP_n \quad (3)$$

or Li^+ conversion or alloying,

$$M_yP_n + xLi^+ + xe^- \rightarrow yM^0 + nLi_bP \quad (4)$$

where M = transition metal and b = oxidation state of P.

An incremental capacitance plot analogous to slow-scan cyclic voltammetry (SSCV) exhibited a reversible lithiation potential centered at 0.56 V vs Li/Li^+ on the first discharge and thereafter remained at around 0.65 V (Figure 2.4). Delithiation takes place at 1.00 V vs. Li/Li^+. From analysis of this plot it appears that the charge storage mechanism involves contributions from the Li^+ insertion/deinsertion reaction and a possible conversion process (consistent with that reported previously).[9a] However, we do not see evidence for an initial direct conversion of the FeP_2 starting material to form Li_3P and Fe^0 in the first discharge. In our amorphous FeP_2 material, the lithiation/delithiation is highly reversible with high capacity retention.

More studies are underway to elucidate the reaction mechanism with lithium. As reported previously, the lithiation/delithation process in crystalline BTMPs is complex, showing distinct electrochemical features and charge/discharge plateaus consistent with the existence of different structures/phases.[9a]

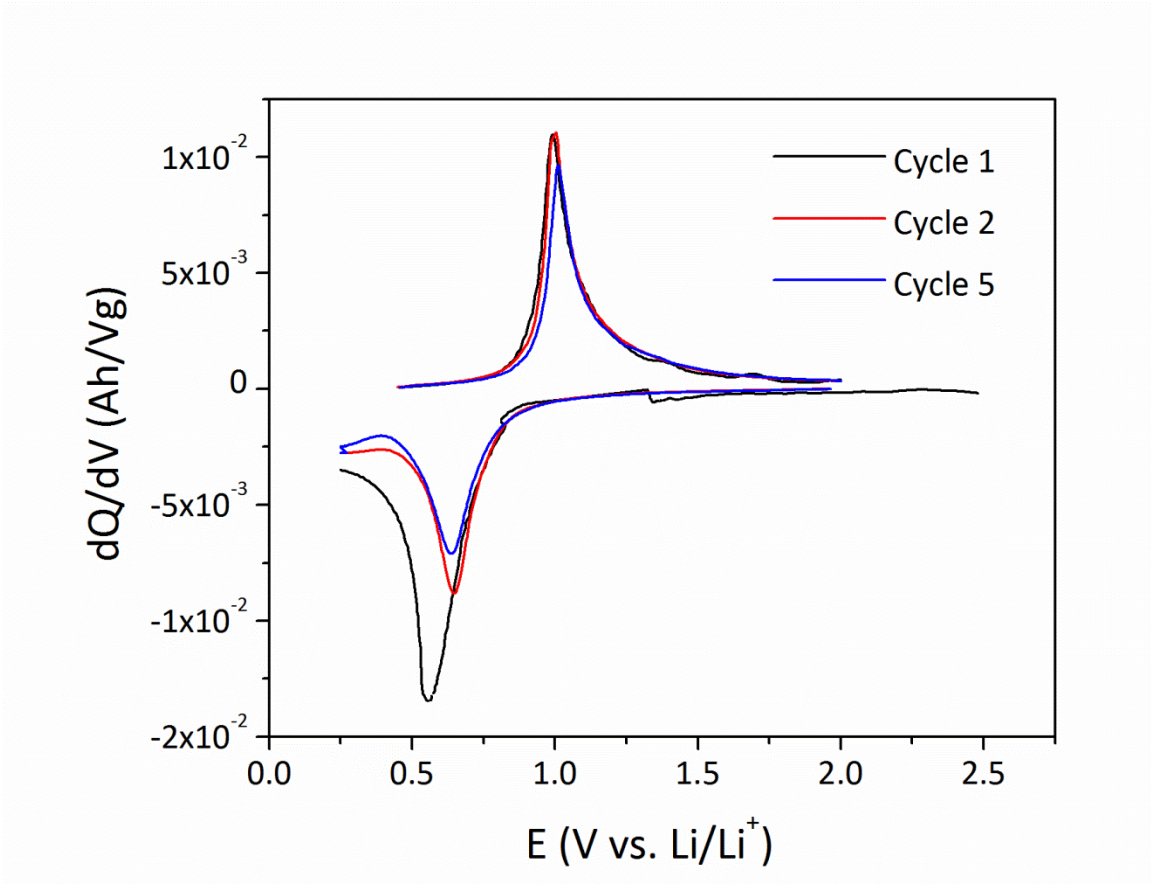

Figure 2.4 Incremental capacitance plots of the first (black), second (red) and fifth (blue) cycles of amorphous FeP_2.

Precaution must be taken with amorphous FeP_2 produced by our low-temperature route, as even minimal air exposure is detrimental to the electrochemical properties of the material. Following brief exposure, a drastic reduction of the initial discharge capacity to 130 mAh/g, along with an absence of voltage plateau features on the discharge/charge plot indicated that the electrode became inactive (Figure 2.5). Consequently, amorphous FeP_2 was handled in an inert environment prior to fabrication of the coin cell in order to determine its characteristic electrochemical properties.

One major factor for exploiting these phosphide-based materials in future applications lies in controlling the kinetics of lithium insertion, thereby lowering the charge/discharge polarization voltage, which is currently responsible for the still poor energy performance of anode (negative) electrodes. Controlling the geometrical orientation and alignment of BTMP nanostructures are other compelling strategies for suppressing volume changes and preventing degradation processes.[31] Our new low-temperature synthetic strategy for the preparation of kinetically stabilized BTMPs may allow us to develop suitable design criteria and guiding principles that allow for control over the morphology and composition and thus help us to discover electrode architectures with enhanced mass and charge transport, electron and ion conductivity, and electron transfer kinetics.[32,33]

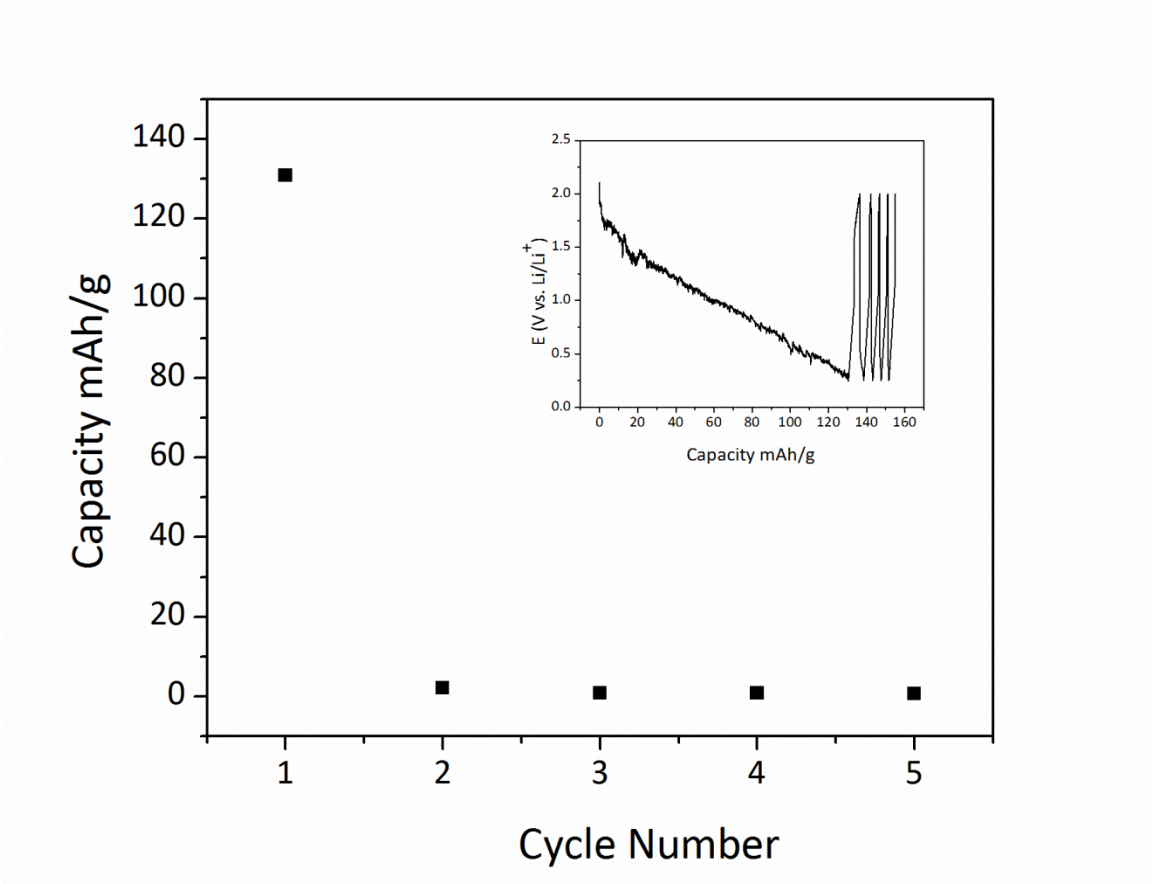

Figure 2.5 Discharge capacities for the first 5 cycles of air exposed, amorphous FeP2. Inset is the corresponding discharge/charge plot at 0.1C.

2.4 CONCLUSIONS

The reaction of $Fe(N(SiMe_3)_2)_3$ with PH_3 in THF at 100 °C gives amorphous FeP_2 in high yield. As an anode material in a Li-ion battery, this material shows remarkable performance towards electrochemical lithiation/delithation, with gravimetric discharge and charge capacities of 1258 and 766 mAh/g, translating to 61% reversibility on the first cycle and a discharge capacity of 906 mAh/g after ten cycles, which translates to 66% retention of the theoretical full conversion capacity of FeP_2 (1365 mAh/g). Moreover, the nano, amorphous morphology has a greatly reduced voltage hysteresis as compared to the bulk crystalline material.

2.5 REFERENCES

(1) (a) Karden, E.; Ploumen, S.; Fricke, B.; Miller, T.; Snyder, K. *J. Power Sources* **2007**, *168*, 2. (b) Kennedy, B.; Patterson, D.; Camilleri, S. *J. Power Sources* **2000**, *90*, 156. (c) Scrosati, B.; Garche, J. *J. Power Sources* **2010**, *195*, 2419. (d) Kang, B.; Ceder, G. *Nature* **2009**, *458*, 190.

(2) Biensan, P.; Simon, B.; Pere, J. P.; de Guibert, A.; Broussely, M.; Bodet, J. M.; Perton, F. *J. Power Sources* **1999**, *81*, 906.

(3) Choi, N.-S.; Profatilova, I. A.; Kim, S.-S.; Song, E.-H.; *Thermochim. Acta*, **2008**, *480*, 10.

(4) Haxel, G. B.; Hedrick, J. B.; Orris, G. J.; *Rare Earth Elements-Critical Resources for High Technology*; Fact Sheet 087-02; U.S. Geological Survey: Reston, VA, 2002.

(5) (a) Bruce, P. G.; Scrosati, B.; Tarascon, J.-M. *Angew. Chem. Int. Ed.* **2008**, *47*, 2930. (b) Guo, J.; Liu, Q.; Wang, C.; Zachariah, M. R. *Adv. Funct. Mater*. **2011**, *22*, 803.

(6) Guo, Y.-G.; Hu, J.-S.; Wan, L.-J. *Adv. Mater.* **2008**, *20*, 2878.

(7) Wang, Y.; Cao, G. *Adv. Mater.* **2008**, *20*, 2251.

(8) (a) Gillot, F.; Bichat, M. P.; Favier, F.; Morcrette, M.; Doublet, M. L.; Monconduit, L. *Electrochim. Acta* **2004**, *49*, 2325. (b) Pralong, V.; Souza, D. C. S.; Leung, K. T.; Nazar, L. F. *Electrochem. Commun.* **2002**, *4*, 516. (c) Souza, D. C. S.; Pralong, V.; Jacobson, A. J.; Nazar, L. F. *Science* **2002**, *296*, 2012. (d) Doublet, M.-L.; Lemoigno, F.; Gillot, F.; Monconduit, L. *Chem. Mater.* **2002**, *14*, 4126. (e) Bichat, M.-P.; Gillot, F.; Monconduit, L.; Favier, F.; Morcrette, M.;

Lemoigno, F.; Doublet, M.-L. *Chem. Mater.* **2004**, *16*, 1002. (f) Gillot, F.; Monconduit, L.; Doublet, M.-L. *Chem. Mater.* **2005**, *17*, 5817. (g) Bichat, M.-P.; Pascal, J.-L.; Gillot, F.; Favier, F. *Chem. Mater.* **2005**, *17*, 6761. (h) Boyanov, S.; Bernardi, J.; Gillot, F.; Dupont, L.; Womes, M.; Tarascon, J.-M.; Monconduit, L.; Doublet, M.-L. *Chem. Mater.* **2006**, *18*, 3531. (i) Gillot, F.; Menetrier, M.; Bekaert, E.; Dupont, L.; Morcrette, M.; Monconduit, L.; Tarascon, J. M. *J. Power Sources* **2007**, *172*, 877. (j) Boyanov, S.; Annou, K.; Villevieille, C.; Pelosi, M.; Zitoun, D.; Monconduit, L. *Ionics*, **2008**, *14*, 183. (k) Villevieille, C.; Robert, F.; Taberna, P. L.; Bazin, L.; Simon, P.; Monconduit, L. *J. Mater. Chem.* **2008**, *18*, 5956. (l) Kim, M. G.; Lee, S.; Cho, J. *J. Electrochem. Soc.* **2009**, *156*, A89. (m) Boyanov, S.; Bernardi, J.; Bekaert, E.; Menetrier, M.; Doublet, M.-L.; Monconduit, L. *Chem. Mater.* **2009**, *21*, 298. (n) Kim, M. G.; Cho, J. *J. Electrochem. Soc.* **2009**, *156*, A277. (o) Mauchamp, V.; Moreau, P.; Monconduit, L.; Doublet, M.; Boucher, F.; Ouvard, G. *J. Phys. Chem. C* **2007**, *111*, 3996. (p) Xiang, J. Y.; Wang, X. L.; Zhong, J.; Zhang, D.; Tu, J. P. *J. Power Sources* **2011**, *196*, 379. (q) Xiang, J. Y.; Wang, X. L.; Xia, X. H.; Zhong, J.; Tu, J. P. *J. Alloys Compd.* **2011**, *509*, 157.

(9) (a) Boyanov, S.; Zithoun, D.; Menetrier, M.; Jumas, J. C. ; Womes, M.; Monoconduit, L. *J. Phys. Chem. C*, **2009**, *113*, 21441-21452. (b) Boyanov, S.; Womes, M.; Jumas, J. C.; Monoconduit, *Hyperfine Interact*, **2008**, *187*, 57-69. (c) Silva, D. C. C.;Crosnier, O.; Ouvrard, G.; Greedan, J.; Safa-Sefat, A.; Nazar, L. F. *Electrochem and Solid State Lett.* **2003**, *6*, A162-A165.

(10) (a) Brock, S. L.; Senevirathne, K. *J. Solid State Chem.* **2008**, *181*, 1552. (b) Stamm, K. L.; Brock, S. L. *J. Alloys and Compounds*, **2008**, *453*, 476. (c) Senevirathne, K.; Burns, A. W.; Bussell, M. E.; Brock, S. L. *Adv. Funct. Mater.* **2007**, *17*, 3933. (d) Gregg, K. A.; Perera, S. C.; Lawes, G.; Shinozaki, S.; Brock, S. L. *Chem. Mater.* **2006**, *18*, 879. (e) Somaskandan, K.; Tsoi, G. M.; Wenger, L. E.; Brock, S. L. *Chem. Mater.* **2005**, *17*, 1190. (f) Aitken, J. A.; Ganzha-Hazen, V.; Brock, S. L. *J Solid State Chem.* **2005**, *178*, 970. (g) Perera, S. C.; Brock, S. L. Mat. Res. Soc. Symp. Proc. 2003, 755, DD5.91-DD6.12.6. (h) Perera, S. C.; Fodor, P. S.; Tsoi, G. M.; Wenger, L. E.; Brock, S. L. *Chem. Mater.* **2003**, *15*, 4034. (i) Perera, S. C.; Tsoi, G.; Wenger, L. E.; Brock, S. L. *J. Am. Chem. Soc.* **2003**, *125*, 13960. (j) Stamm, K. L.; Garno, J. C.; Liu, G-Y.; Brock, S. L. *J. Am. Chem. Soc.* **2003**, *125*, 4038. (k) Muthuswamy, E.; Brock, S. L. *J. Am. Chem. Soc.* **2010**, *132*, 15849. (l) Muthuswamy, E.; Brock, S. L. *Chem. Commun.* **2011**, *47*, 12334.

(11) (a) Henkes, A. E.; Schaak, R. E. *Inorg. Chem.* **2008**, *47*, 671. (b) Henkes, A. E.; Vasquez, Y.; Schaak, R. E. *J. Am. Chem. Soc.* **2007**, *129*, 1896. (c) Henkes, A. E.; Schaak, R. E. *Chem. Mater*. **2007**, 19, 4234.

(12) Qian, C.; Kim, F.; Ma, L.; Tsui, F.; Yang, P.; Liu, J. *J. Am. Chem. Soc.* **2004**, *126*, 1195.

(13) Wang, M.; McDonald, R.; Mar, A. *Inorg. Chem.* **2000**, *39*, 4936.

(14) (a) Kleinke, H.; Franzen, H. F. J. Solid State Chem. 1997, 131, 379-386. (b) Kleinke, H.; Franzen, H. F. *J. Am. Chem. Soc*. **1997**, *119*, 12824.

(15) Chen, L.; Huang, M.; Gu, Y.; Shi, L.; Yang, Z.; Qian, Y. *Materials Letters*, **2004**, *58,* 3337.

(16) Liu, S.; Qian, Y.; Xu, L. *Solid State Communications*, **2009**, *149*, 438.

(17) Barry, B. M.; Gillan, E. G. *Chem. Mater.* **2008**, *20*, 2618.

(18) George, P. P.; Pol, V. G.; Gedanken, A. *J. Nanoparticle Research,* **2007**, *9*, 1187.

(19) (a) Davidson, P. J.; Lappert, M. F.; Pearce, R. *Chem. Rev.* **1976,** *76,* 219-242. (b) Schrock, R. R.; Parshall, G. W. *Chem. Rev.* **1976,** *76,* 243.

(20) Lappert, M. F.; Power, P. P.; Protchenko, A.; Seeber, A.; John Wiley and Sons Pub., **2008**, Ch.6 pp 149.

(21) Literature from the 19th and early 20th centuries contains evidence that PH_3 will react with salts of Cr, U, Mn, Ni, Co and Fe to form metal phosphides, however these materials are poorly characterized and these reactions do not appear to have been investigated in the modern era. See for example *Gmelins Handbuch der Anorganischen Chemie*, Part C, **1965**, *16*, 45.

(22) **Caution:** Phosphine is a highly poisonous and reactive gas. All operations must be performed by highly trained personnel under rigorous exclusion of air.

(23) Alyea, E. C.; Bradley, D. C.; Copperthwaite, R. G. *Dalton Trans.* **1972**, 1580.

(24) Celio, H.; Johnson, A. J. University of Texas, Austin, TX. Unpublished work, 2012.

(25) Grosvenor, A. P.; Cavell, R. G.; Mar, A. *Struct. Bond.* **2009,** *133,* 4.

(26) Grosvenor, A. P.; Wik, S. D.; Cavell, R. G.; Mar, A. *Inorg. Chem.* **2005,** *44,* 8988.

(27) Myers, C. E.; Franzen, H. F.; Anderegg, J. W. *Inorg. Chem.* **1985,** *24,* 1822.

(28) Wagner, C. D.; Naumkin, A. V.; Kraut-Vass, A.; Allison, J. W.; Powell, C. J.; Rumble, J. R., Jr. *NIST X-ray Photoelectron Spectroscopy (XPS) Database, Version 3.5*. http://srdata.nist.gov/xps/ Default.aspx (Accessed July 2011).

(29) Nemoshkalenko, V. V.; Didyk, V. V.; Krivitskii, V. P.; Senkevich, A. I. *Zh. Neorg. Khim.* **1983,** *28,* 2182-2186. (30) Ohkawa, H.; Yoshida, K.; Saito, M.; Uematsu, K.; Toda, K.; Sato, M. *Chem. Lett.* **1999**, *28*, 1017.

(30) Cyclability is defined as the coulomic efficiency between lithation and delithation. In specific terms the coulombic efficiency of battery is the ratio of integrated charge associated with charging compared to the charge that can be extracted from the battery during discharging. The losses that reduce coulombic

efficiency are primarily due to the loss in charge due to secondary reactions, such as the electrolysis of solvent or other surface redox reactions in the battery.

(31) Qian, C.; Kim, F.; Ma, L.; Tsui, F.; Yang, P.; Liu, J. *J. Am. Chem. Soc.* **2004**, *126*, 1195.

(32) Balaya, P.; Bhattacharyya, A. J.; Jamnik, J.; Zhukovskii, Yu. F.; Kotomin, E. A.; Maier, J. *J. Power Sources* **2006**, *159*, 171.

(33) Maier, J. *J. Power Sources* **2007**, *174*,569.

CHAPTER 3[2]

In Situ Raman Study of Phase Stability of $Li_3V_2(PO_4)_3$ upon Thermal and Laser Heating

3.1 INTRODUCTION

Transition metal phosphates that include $LiFePO_4$, $LiMnPO_4$ and $Li_3V_2(PO_4)_3$ have resurged as alternatives to the commercially dominating $LiCoO_2$ cathode owing to their safety, thermal stability, low cost and competitive energy densities.[1,2] The inherent stability of these materials originate from the P-O bond covalency in the metal phosphate framework that houses mobile Li ions.[1] $Li_3V_2(PO_4)_3$ can either be found in the rhombohedral (NASICON) or monoclinic (α) lattice system at room temperature, depending on the synthetic route, with the latter phase being the more thermodynamically stable.[2]

In the monoclinic lattice, the $V_2(PO_4)_3$ units are alternately positioned perpendicular to one another creating a slightly more compressed structure as compared to the rhombohedral phase.[3] More specifically, two distinct vanadium sites are present in slightly distorted VO_6 octahedra that share oxygen vertices with PO_4 tetrahedra (the three phosphate tetrahedra can be distinguished by their varying average P-O bond lengths).[2] Within the interstitial voids of the lattice are three unique lithium sites. Following the assignment used by Yin et al. Li(1) is coordinated to four oxygens forming a true tetrahedron while Li(2) and Li(3) occupy a highly distorted tetrahedron with a fifth Li-O bond.[2] Along the *a*-axis of the crystal, Li polyhedra are linked through common oxygen allowing for diffusion along the other directions.[3] However, Lee and co-workers

[2] Reprinted with permission from Membreño, N.; Xiao, P.; Park, K.-S.; Goodenough, J. B.; Henkelman, G.; Stevenson, K. J. *J. Phys. Chem. C* **2013**, *117*, 11994. Copyright 2013 American Chemical Society. Penghao Xiao conducted DFT calculations. Dr. Henkelman supervised the DFT calculations. Kyusung Park synthesized $Li_3V_2(PO_4)_3$. Dr. Goodenough supervised the synthesis. Dr. Stevenson supervised the characterization of $Li_3V_2(PO_4)_3$ via Raman and thermal studies.

calculated lower migration energies along the [001] direction resulting in a highly anisotropic Li^+ mobility despite not being 1-dimensional.[4] Nevertheless, the ability to electrochemically extract all three lithium ions from α-$Li_3V_2(PO_4)_3$ gives it the high specific gravimetric capacity of 197 mAh/g. This value is the highest of all the transition metal phosphates, making it a prospective cathode material for lithium-ion batteries and meriting a fundamental understanding of its vibrational modes through Raman microscopy.

Raman microscopy is highly suitable for probing the chemical bond structure in electrode materials used in lithium-ion energy storage devices. The microscope offers the ability to focus the photon beam onto a small area (~1 μm diameter) of importance for electrode materials that are composite mixtures of conductive carbon (to enhance electronic conductivity) and binder.[5] Raman microscopy frequently serves as a complementary technique to X-ray diffraction (XRD)[6] and powder neutron diffraction (PND) data for crystalline materials. However, unlike diffraction methods that solely identify materials with long range order, Raman spectroscopy allows for the investigation of amorphous materials.[5] On a more technical level, there is no need for particular sample preparation and the excitation source is chosen to be non destructive. Consequently, little to no modifications are made to the sample, permitting it to be further analyzed by other techniques.[5]

From an analytical perspective, Raman microscopy provides the high sensitivity necessary to detect changes in crystal symmetry, oxidation states, local phase inhomogeneities and structural order/disorder.[5] This sensitivity is especially useful for *ex situ* analysis of cycled electrodes.[5,7] Moreover, *in situ* measurements can be easily devised by using transparent materials (such as glass, quartz, and sapphire) as optical windows for electrochemical cells as they present too weak a Raman signal to cause

interference.[8–10] These spectroelectrochemical devices have served as invaluable tools for understanding lithium intercalation mechanisms in both cathode and anode materials as well as for the understanding of the chemical and/or electrochemical processes that are responsible for cell failure.[5]

Although structural characterization of transition-metal phosphates has predominantly been executed via Li^7 magic angle spinning nuclear magnetic resonance (MAS NMR),[11,12] Mossbauer spectroscopy and PND[13], a number of optical spectroscopy studies have been reported for these materials.[14–17] The commercial success of the cheap and toxically benign $LiFePO_4$ has made it the most thoroughly studied of the phosphates.[1] Burba et al.[14] observed Raman spectral changes of chemically delithiated $LiFePO_4$ ($0 \leq x \leq 1$). With partial delithiation ($Li_{0.74}FePO_4$), new spectral peaks were found in the v_1 and v_3 region of the spectrum that grew in intensity until complete delithiation ($FePO_4$). Despite not having complete assignments of the vibrations, these observations provided indirect evidence of the two phase mechanism for the electrochemical delithiation of $LiFePO_4$. Paraguassu et al.[18] later assigned all 36 Raman wavenumbers for $LiFePO_4$ using a computational simulation based on Wilson's FG matrix method. The method was applied to $LiFePO_4$ and $LiNiPO_4$. It showed good agreement between experimental and calculated wavenumbers (about 5 and 9% deviation respectively).

$Li_3M_2(PO_4)_3$ (M = Sc, Fe) compounds, isostructural to $Li_3V_2(PO_4)_3$, were investigated by Kravchenko et al.[17] by means of infrared (IR) and Raman microscopy in the 77-670 K temperature range to understand the structural changes associated with the superionic phase transition.[7]Complete spectral assignments were not made in these studies, but identification of the sublattice lithium vibrations, found at 505 cm^{-1} in the Raman spectrum of $Li_3Sc_2(PO_4)_3$, was made by comparison of Li^6 isotope enriched $Li_3Sc_2(PO_4)_3$ with a non-enriched sample. Burba et al.[7] later looked at vibrations for the

electrochemically delithiated species ($0 \leq x \leq 3$) of both NASICON and α-$Li_3V_2(PO_4)_3$ with emphasis on the $(PO_4)^{3-}$ vibrations that are highly sensitive to Li^+ extraction and the oxidation state of vanadium. *Ex situ* mid-IR spectra were found to be in accordance with the already established complex two-phase transition mechanism proposed by Yin et al.[2,12] Furthermore, the work showed that after the first electrochemical cycle full reversibility of the α-$Li_3V_2(PO_4)_3$ structure is regained with some $(PO_4)^{3-}$ band broadening indicative of some local disordering. The investigators intended to similarly analyze the $(PO_4)^{3-}$ Raman active vibrations for α-$Li_3V_2(PO_4)_3$ at various electrochemically delithiated stages but the weak bands observed did not allow for further analysis. The usually intense phosphate peaks were thought to be broadened and weakened because of an amorphous surface layer on the particles.

Here the complete Raman vibrational spectrum of α-$Li_3V_2(PO_4)_3$ is reported and compared to the theoretical Raman frequencies (wavenumbers) calculated with density functional theory (DFT) using the Vienna *ab inito* simulation package (VASP). In addition, thermal effects as a function of irradiation power density were studied to understand the phase stability of α-$Li_3V_2(PO_4)_3$ under confocal Raman measurements. Our findings show that with increasing irradiation power α-$Li_3V_2(PO_4)$ transforms into the high temperature β and γ-phases before becoming completely oxidized to $LiVOPO_4$. The oxidation process was further confirmed by thermal studies with both Raman interfaced with a hot-stage and differential scanning calorimetry (DSC).

3.2 Experimental and Theoretical Methods

3.2.1 α-$Li_3V_2(PO_4)_3$ Solid State Synthesis

For the preparation of α-$Li_3V_2(PO_4)_3$, stoichiometric amounts of Li_2CO_3 (Aldrich, >99%), V_2O_3 (Aldrich, 99.99%), and $(NH_4)H_2PO_4$ (Alfa Aesar, >98%) were

thoroughly mixed in a mortar with the aid of isopropyl alcohol for 1-hr. An excess of lithium (2%) was added to compensate for high-temperature lithium evaporation. After thoroughly grinding the precursor materials, the dry mixture was thermally decomposed at 450 ^{o}C in an Ar atmosphere for 1-hr. The decomposed and oxidized powder was once again ground in a mortar and subsequently pressed into a pellet. Finally, the pellet was heated to 900 ^{o}C under a 95 % Ar 5% H_2 gas flow for 5 hrs. Upon completion of the calcination process, a green-colored pellet was obtained and ground into a fine powder for materials characterization.

3.2.2 XRD Characterization

Diffraction patterns were collected on a Rigaku R-axis Spider diffractometer equipped with an image plate detector using a Cu Kα radiation source (λ=1.542 Å) operated at 40 kV and 40 mA. Samples were mounted on a 0.5 mm Nylon loop and scanned for 10 minutes while rotating at 1 °/min. With the 2DP software, radial data were integrated over 2θ = 10-60 °. The peaks were analyzed by using the Joint Committee on Powder Diffraction Standards (JCPDS) database.

3.2.3 Scanning Electron Microscopy

Images were obtained with a Model Quanta 650 FEG at 30.00 kV. 3.2.4 Ex Situ and In Situ Raman Microscopy

3.2.4 *Ex situ* and *In situ* Raman Microscopy

Raman spectra were acquired with a Renishaw inVia microscope system having a 514.5 nm Ar^{+} laser in the backscattering configuration. For ex situ analysis, the beam was focused with a 50x objective lens resulting in approximately a 1.3 μm spot diameter under air. The phase stability of $Li_3V_2(PO_4)_3$ under laser irradiation was studied at 0.067, 0.080, 0.113, 0.403, 0.855, 4.101 and 7.612 mW power. The laser was focused on the

same sample area while increasing or decreasing the power of the laser. For the in situ heat analysis, under N_2 and air, a Linkam Scientific THMS600 microscope stage was used to ramp the sample temperature from room temperature to 600 °C. The temperature program used was as follows: 23-126 °C at a rate of 2 °C/min, 126-150 °C at a rate of 1 °C/min, 150-195 °C at a rate of 2 °C/min, 195-220 °C at a rate of 1 °C/min and 220-600 °C at a rate of 10 °C/min. 1-hr temperature holds were performed at 126, 150, 195 and 220 °C while 30-min temperature holds were performed at 258, 296, 334, 372, 410, 448, 486, 524, 562, and 600 °C to ensure complete and homogenous heating of the sample. The beam was focused with an L 50x objective lens resulting in approximately a 0.8 μm spot diameter. An acquisition time of about 300 s was used for the *in situ* heat analysis and was varied between 20–120 s for the *ex situ* studies.

3.2.5 Thermal Studies

Differential Scanning Calorimetry (DSC) was conducted on a TA Instruments DSC-Q100. A sample of 9.000 mg was placed in an Al crucible. Each DSC cycle consisted of heating the sample from 25 °C to 250 °C and then cooling it back to 25 °C. A total of 3 cycles were performed at a rate of 5 °C/min under a N_2 flow rate of 50.00 mL/min. Thermal Gravimetric Analysis (TGA) was performed on a TA Instruments TGA-Q50. A sample of 4.347 mg was placed in a Pt crucible. The first ramp consisted of heating the sample from 25 °C to 500 °C at a rate of 2.50 °C/min. The second ramp continued the heating from 500 °C to 800 °C at a rate of 5.00 °C/min.

3.2.6 VASP-DFT

The vibrational frequency calculations were performed with finite differences of the atomic forces from DFT,[19] using the HSE06 hybrid functional for the exchange-correlation energy.[20] Valence electrons were described with a plane wave basis set up to

an energy cutoff of 283 eV; core electrons were incorporated into pseudo-potentials in the projector augmented wave phasework.[21–24] Only the gamma point was included for the Brillouin-zone integration. The lattice parameters for the crystal super-cell were set to experimental values.[2] Tests in which the volume was varied showed that the energy of the experimental lattice constants was very close to the minimum from fitting to the equation of state (0.15 eV higher for 80 atoms). For the frequency calculations, only symmetrically inequivalent forward differences were taken to save computational cost. The magnitude of each displacement was 0.01 Å.

DFT+U functional was also performed with an effective U value of 4.0 as a comparison, but the frequencies were systematically underestimated in the whole range. The frequencies are eigenvalues of the Hessian matrix whose elements are the second derivatives of energy with respect to the displacements. Thus they are very sensitive to the accuracy of the potential energy surface. This is also the reason that makes Raman/IR spectroscopy a powerful tool in detecting local chemical environment changes.

3.3 Results and Discussion

3.3.1 Characterization of α-$Li_3V_2(PO_4)_3$

The solid state synthesis of α-$Li_3V_2(PO_4)_3$ was as described in full detail in the experimental section. The product was characterized with XRD and ESEM to determine the phase purity, crystal structure and particle size. As shown in Figure 3.1(a), the material can be indexed to the monoclinic space group $P2_1/n$. ESEM images (Figure 3.1(b)) reveal highly agglomerated particles ranging from 0.1-50 μm in size.

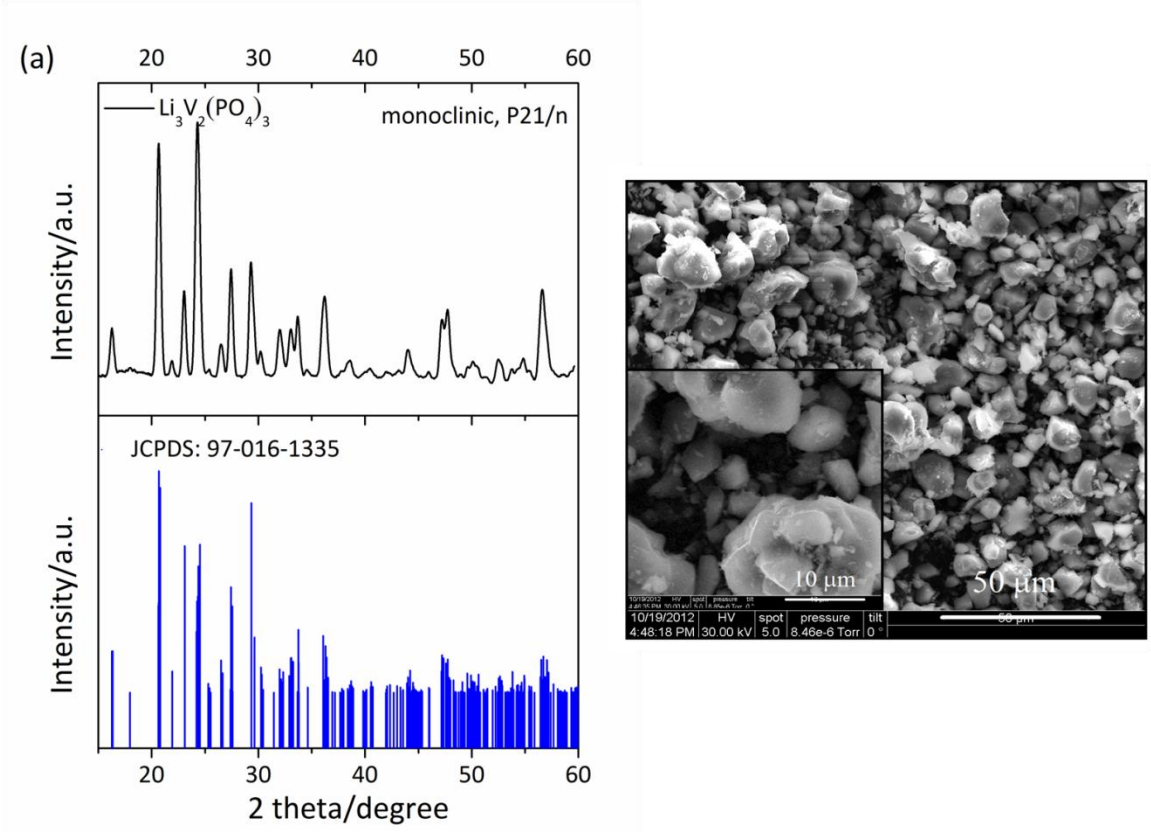

Figure 3.1 (a) XRD and (b) ESEM of microcrystalline $Li_3V_2(PO_4)_3$.

3.3.2 Comparison of Experimental and Theoretical Raman Spectra

From the symmetry-based analysis of α-$Li_3V_2(PO_4)_3$, the predicted number of normal modes is 237 with 120 of these normal modes Raman active; the remainder are IR active.[7]

$$\Gamma_{\alpha\text{-}Li_3V_2(PO_4)_3} = 60\ A_g + 60\ B_g + 59\ A_u + 58\ B_u \quad (1)$$

As with any centrosymmetric crystal, the IR active modes are Raman inactive and vice versa. Any mode that respects centrosymmetry is IR active. The Raman active modes can be further labeled as A_g or B_g. A_g modes are invariant under all four symmetry operations of the C_{2h} point group while B_g modes are invariant for two of the operations. By analyzing the symmetry of each Raman mode for α-$Li_3V_2(PO_4)_3$ with pyspglib,[25] all of the Raman modes were labeled. Some of the calculated Raman modes, along with their symmetry assignments, can be found in Table 3.1. A complete list of the calculated modes can be found in the Appendix. The vibration modes corresponding to the 294.9, 599.7, 1055.3 and 1085.7 cm^{-1} assignments are represented as schemes shown in Figure 3.2.[26]

From the unpolarized Raman spectrum of α-$Li_3V_2(PO_4)_3$, only 19 vibrational modes 1077.9, 1058.7,1030.0, 1009.2, 975.4, 652.2, 603.6, 559.7, 505.5, 454.4, 430.4, 375.3, 349.4, 290.4, 255.5, 223.9, 169.4, 134.1 and 118.1 cm^{-1} were detected (Figure 3.3 and Table 3.1).

Nevertheless, the DFT calculations clearly distinguish between the experimental spectral regions where vibrational modes occur from the regions where no vibrations are present. Vibrational spectra of transition-metal phosphates consist of internal and external modes. Internal modes are vibrations that occur within atomic groups (such as LiO_4, MO_6

Table 3.1 Raman modes for $Li_3V_2(PO_4)_3$ observed by Raman microscopy and the corresponding calculated Raman modes with symmetry assignments by VASP-DFT.

Table 1. Raman vibrational modes for $Li_3V_2(PO_4)_3$ in units of cm^{-1}			
Number	Calculated	Observed	Assignment
1	1085.7	1077.9	A_g
2	1055.3	1058.7	B_g
3	1030.4	1030.0	A_g
4	1010.2	1009.2	A_g
5	974.0	975.4	A_g
6	654.9	652.2	A_g
7	599.7	603.6	B_g
8	560.4	559.7	A_g
9	508.0	505.5	B_g
10	451.2	454.4	B_g
11	427.5	430.4	B_g
12	376.5	375.3	A_g
13	346.1	349.4	A_g
14	294.9	290.4	A_g
15	252.7	255.5	A_g
16	224.3	223.9	A_g
17	167.6	169.4	A_g
18	136.2	134.1	A_g
19	116.7	118.1	B_g

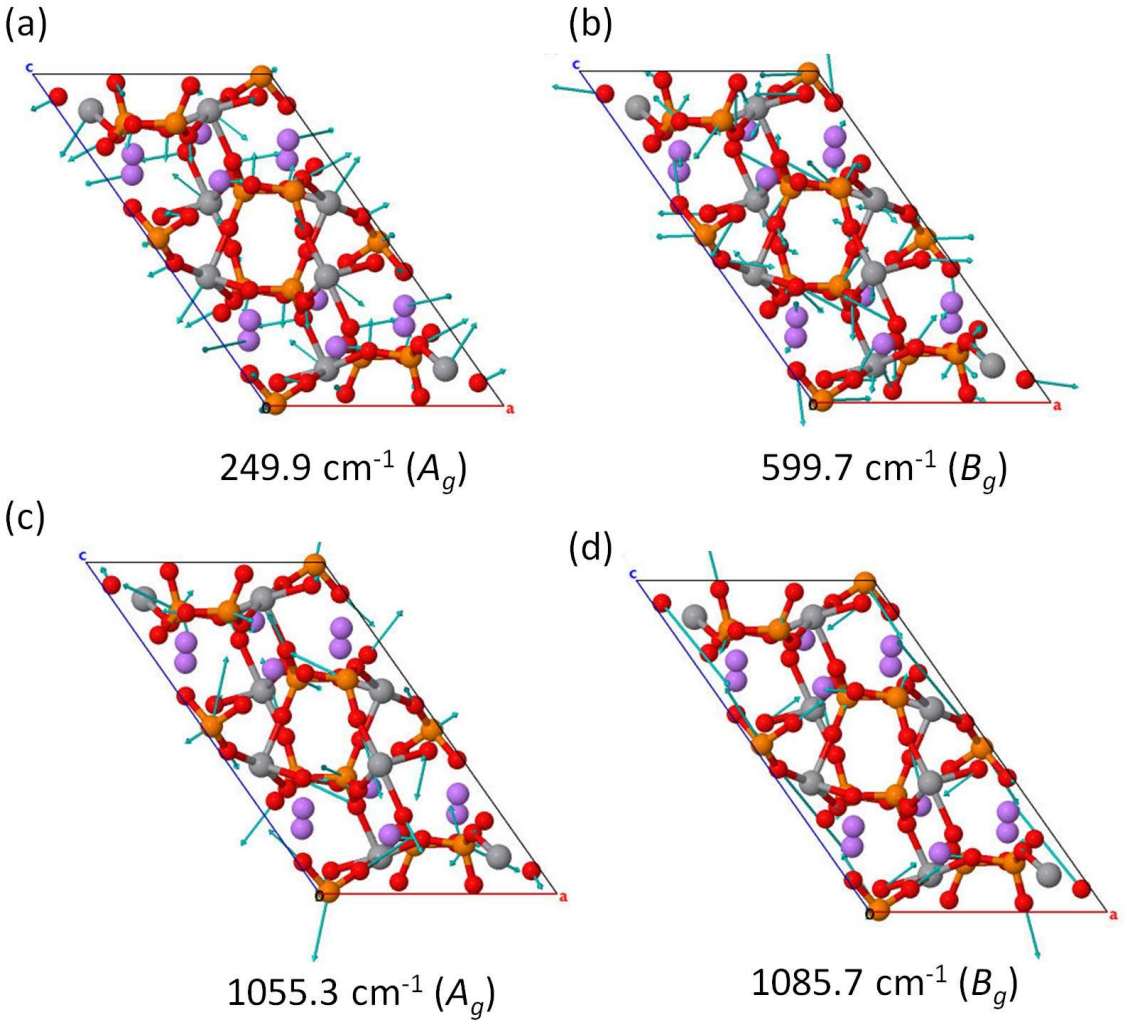

Figure 3.2 Eigenvectors for the (a) 294.9, (b) 599.7, (c) 1055.3 and (d) 1085.7 cm^{-1} vibrational modes for α-$Li_3V_2(PO_4)_3$.

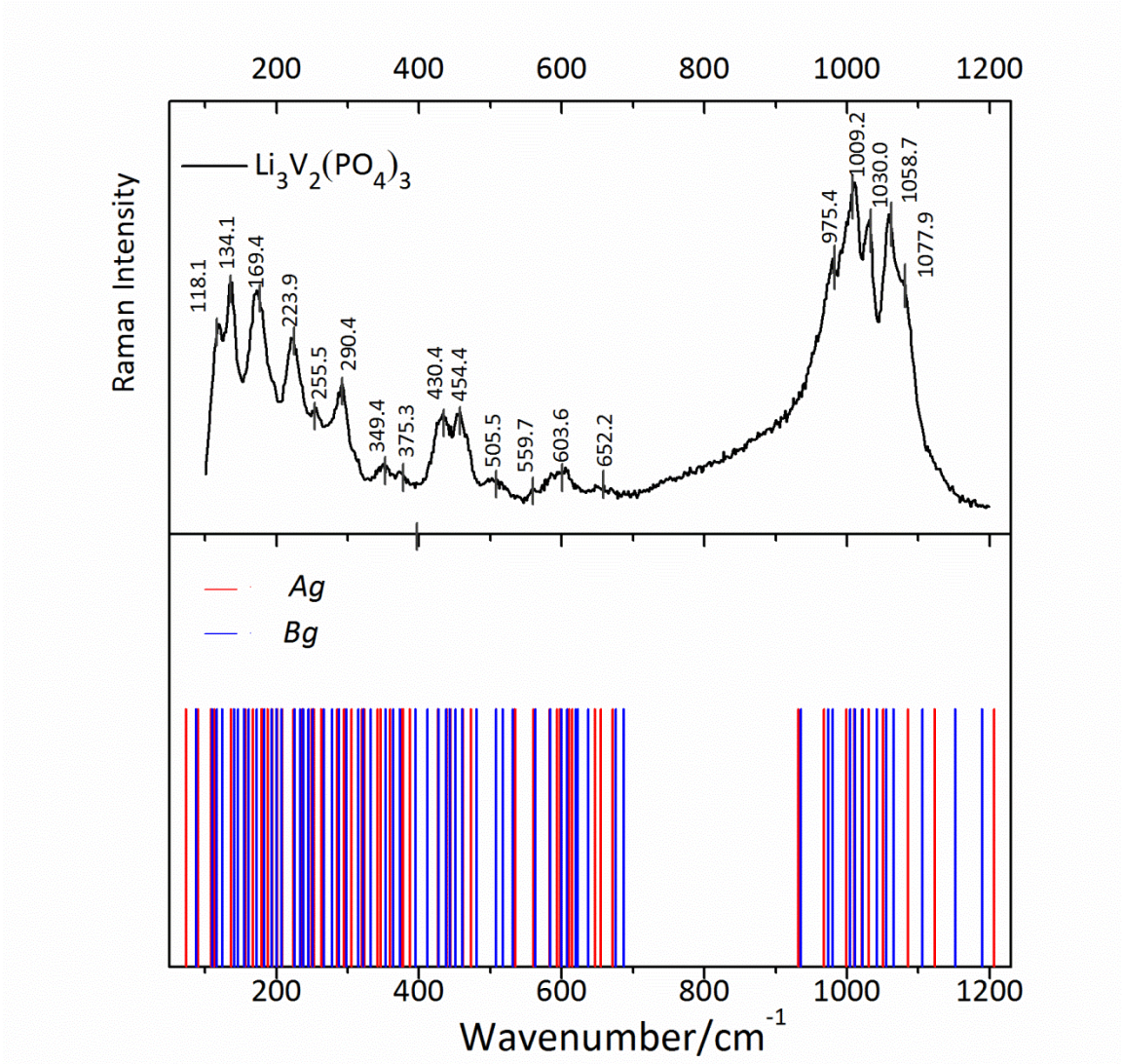

Figure 3.3 Observed (top) and calculated (bottom) Raman spectra for α-$Li_3V_2(PO_4)_3$ in the 50-1230 cm^{-1} wavenumber range. The observed spectrum above was acquired with a 50x objective at a power of 0.855 mW and a total acquisition time of 120 s at room temperature.

and PO_4 polyhedra) and external modes are vibrations of the atomic groups and crystal lattice.[17] For the $Li_3M_2(PO_4)_3$ compounds, the PO_4 valency bond vibrations occur between 1250-900 cm^{-1}, PO_4 deformation vibrations are in the 700-400 cm^{-1} region and the external lattice vibrations correspond to the low frequency region of 400-0 cm^{-1}. As expected, the PO_4 valency bond vibrations are the most intense peaks.

3.3.3 Vibrational Modes of α-$Li_3V_2(PO_4)_3$ as a Function of Laser Irradiation Power

Raman spectra of α-$Li_3V_2(PO_4)_3$ were taken at different laser irradiation powers to examine the phase stability of the material. At 0.067 mW, peaks centered at 1058.7, 1030.0, 1009.2, 975.4, 603.6, 454.4, 430.4, 290.4, 223.9, 169.4 and 134.1 cm^{-1} were detected as is shown in Figure 3.4(a). At 0.113 mW, additional peaks at 1077.9, 652.2, 559.7, 505.5, 375.3, 349.4, 255.5 and 118.1 cm^{-1} were detected. A gradual increase in power to 0.855 mW resulted in these peaks becoming sharper and, more intense with no additional features appearing in any of the spectra (Figure 3.4(a)). Therefore, it was concluded that within the 0.067-0.855 mW power range, the monoclinic phase was conserved.

Irradiation at 0.855 to 4.101 mW resulted in various changes of the Raman spectrum (Figure 3.4(b)-(c)). Because spectral changes occurred rapidly, the acquisition time was reduced six fold in this power range. Within the first scan (20 s); the originally sharp phosphate vibrations in the high region of the spectrum were replaced with two broad peaks at 1048 and 1001 cm^{-1}. Two originally distinct peaks at 454.4 and 430.3 cm^{-1} merged into a single peak. Additionally, a shoulder around 1130 cm^{-1} emerged and the lattice vibrations significantly diminished in intensity. By the fifth scan (Figure 3.4(b)) the shoulder at 1130 cm^{-1} continued to grow in intensity and experienced a slight blue shift. Two new peaks were found at 947 and 876 cm^{-1}. After 220 s (11 scans) the new

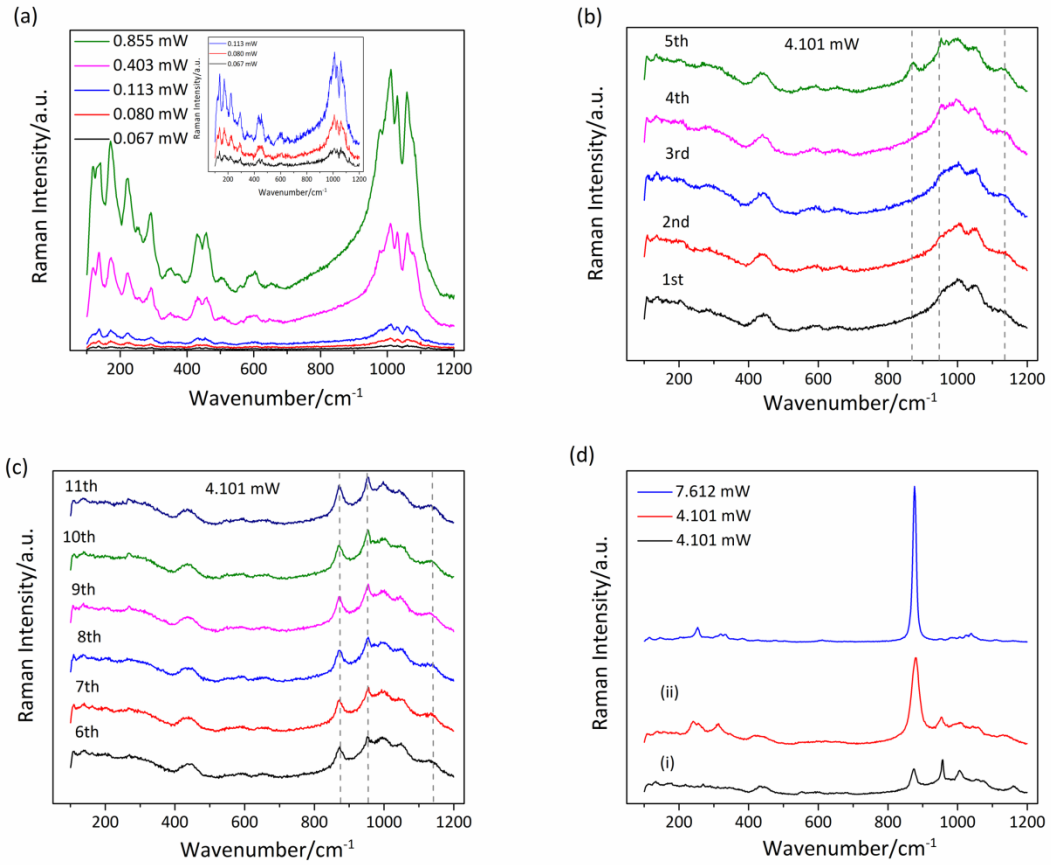

Figure 3.4 Raman spectra of α-$Li_3V_2(PO_4)_3$ at different laser irradiation powers with the 50x objective: (a) from 0.067-0.855 mW (120 s acquisition time), (b)-(c) 11 successive measurements at 4.101 mW, with each acquisition being 20 s, (d) continuous exposure at 4.101 mW with longer acquisitions of (i) 120 s and (ii) 300 s and the highest power measurement at 7.612 mW (120 s acquisition time).

features of the spectrum stabilized (the shoulder at 1130 cm^{-1} was now further blue shifted to 1140 cm^{-1}). In order to determine whether the features of the stabilized spectrum were irreversible, the power was reduced to 0.855 mW. After seven scans none of the general features changed (Figure 3.5(a)). Therefore, only one scan was conducted at the lower irradiation powers of 0.403 and 0.113 mW (Figure 3.5(b)). Clearly, the original spectrum was not recovered.

Continuous irradiation at 4.101 mW caused the 876 cm^{-1} mode to dramatically increase in intensity (Figure 3.4(d) i & ii). At the highest irradiation power of 7.612 mW, the intensity of the 876 cm^{-1} peak dominated the remaining spectral features of the spectrum (Figure 3.4(d)). Moreover, visually the original green powder became a much darker, olive green. Evidently, α-$Li_3V_2(PO_4)_3$ is not stable at an irradiation power of 4.101 mW or greater.

Similar power studies have been conducted on olivine $LiFePO_4$. Bai et al.[27] showed that the thermal effect of laser irradiation created two new peaks in the low-wavenumber region at 215 and 277 cm^{-1}. These peaks were associated with formation of α-Fe_2O_3.[28] Continual laser irradiation led to a broad background in the high-wavenumber region that the authors attributed to amorphous $FePO_4$. However, upon reversing the power of the laser, the amorphous background vanished and the most prominent peak centered at 950 cm^{-1} remained unchanged in intensity, showing that the basic structure was maintained throughout the course of the study. It could be assumed that comparable transformations occurred for α-$Li_3V_2(PO_4)_3$ possibly leading to the creation of V_2O_5 and amorphous $V_2(PO_4)_3$. The formation of these phase impurities created by laser irradiation on $Li_3V_2(PO_4)_3$ were indirectly investigated through thermal studies.

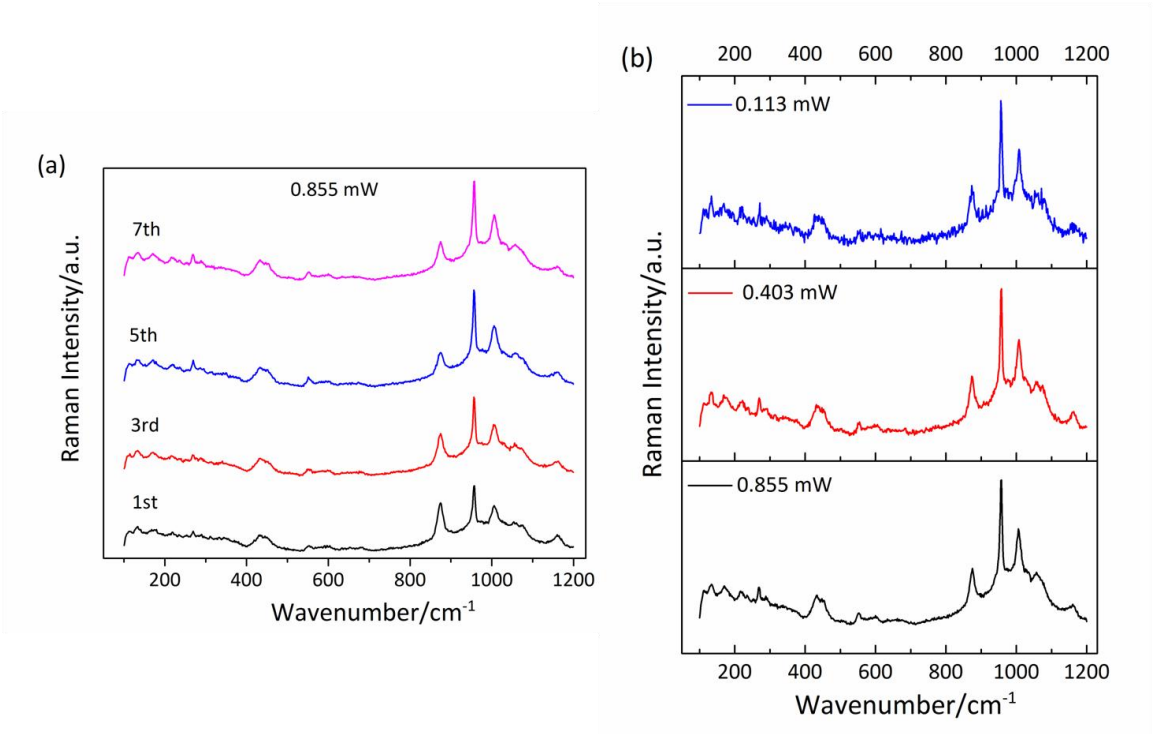

Figure 3.5 (a) 1st, 3rd, 5th and 7th Raman measurements of $Li_3V_2(PO_4)_3$ performed at 0.855 mW, intended to stabilize the intermediate, thermally degraded material after 4.101 mW exposure. (b) Raman measurements performed at 0.401 and 0.113 mW were followed to test the reversibility of the thermal damage. All spectra were taken using the 50x objective with an acquisition time of 120 s.

3.3.4 Thermal studies on α-$Li_3V_2(PO_4)_3$

In the confocal Raman microscope arrangement, a very high power density is concentrated on a small area of the sample. Absorption of radiation can cause the local temperature to increase by several hundreds of degrees. Consequently, as the irradiation power was increased, the local temperature of α-$Li_3V_2(PO_4)_3$ also increased. Having conducted the measurements in air, it is reasonable to suspect that the material is susceptible to oxidation at the higher irradiation powers and that oxidation brought about the changes in the Raman spectrum. *In situ* Raman heat treatment in air and in an inert atmosphere (N_2) clarified this using a temperature controlled heating stage.

A microscope heating stage permitted the acquisition of Raman spectra for α-$Li_3V_2(PO_4)_3$ from room temperature to 600 °C. No spectral changes were observed from 23.5 °C to 116.7 °C (Figure 3.6(a)) indicating that the monoclinic phase was preserved in air within this temperature range. At 125 °C the 1030 cm^{-1} peak and shoulder at 1079 cm^{-1} disappeared. These general features remained until reaching 202.0 °C, at which point more dramatic changes took place such as broadening of the 1009 cm^{-1} peak, merging of the 435 and 455 cm^{-1} peaks into a single peak, transformation of the 979 cm^{-1} peak into a shoulder and a significant diminishing of the lattice modes. The general features of the spectrum at 202.0 °C (Figure 3.6(b)) closely matched those of the first scan at 4.101 mW power in the irradiation power study (Figure 3.4(b)).

Further increase in heating temperature (Figure 3.6(c)) resulted in additional spectral changes. At 333.7 °C an additional peak at 1140 cm^{-1} can be seen that gradually grew in intensity with higher heating temperatures and experienced a slight blue shift once reaching 595.8 °C. Furthermore, at 595.8 °C a new peak at 876 cm^{-1} became the dominant mode of the spectrum. These changes are analogous to the spectral transitions seen during the irradiation power study (Figure 3.7(a)-(b)). However, the lower intensity

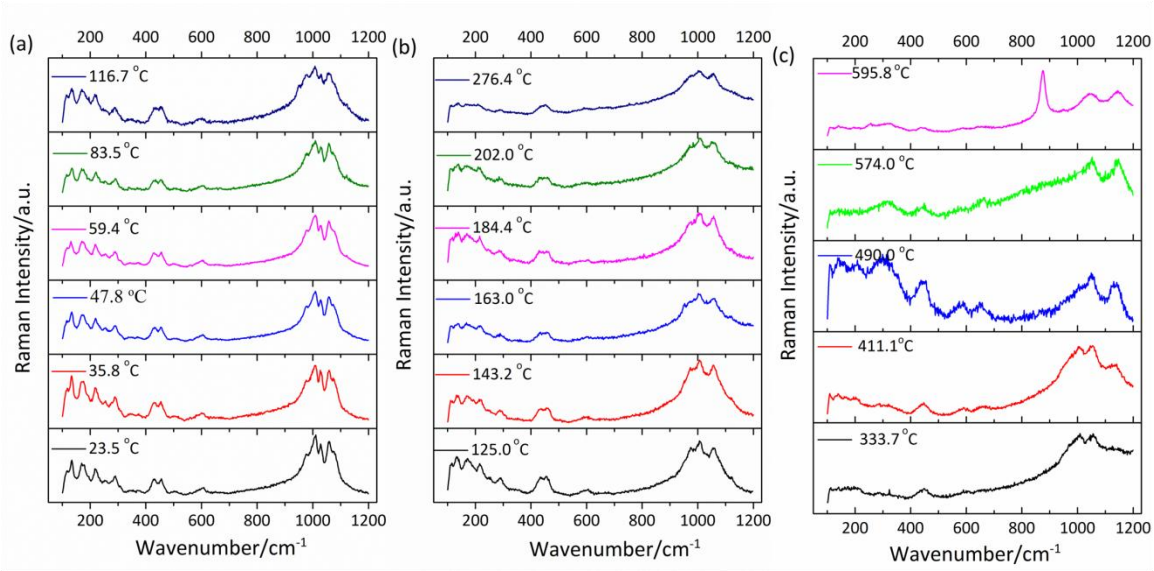

Figure 3.6 *In situ* Raman spectra of α-$Li_3V_2(PO_4)_3$ at different heating temperatures under air: (a) from 23.5-116.7 °C (b) 125.0-276.4 °C and (c) 333.7-595.8 °C taken with a 50x objective and a laser power of 0.855 mW for 300 s.

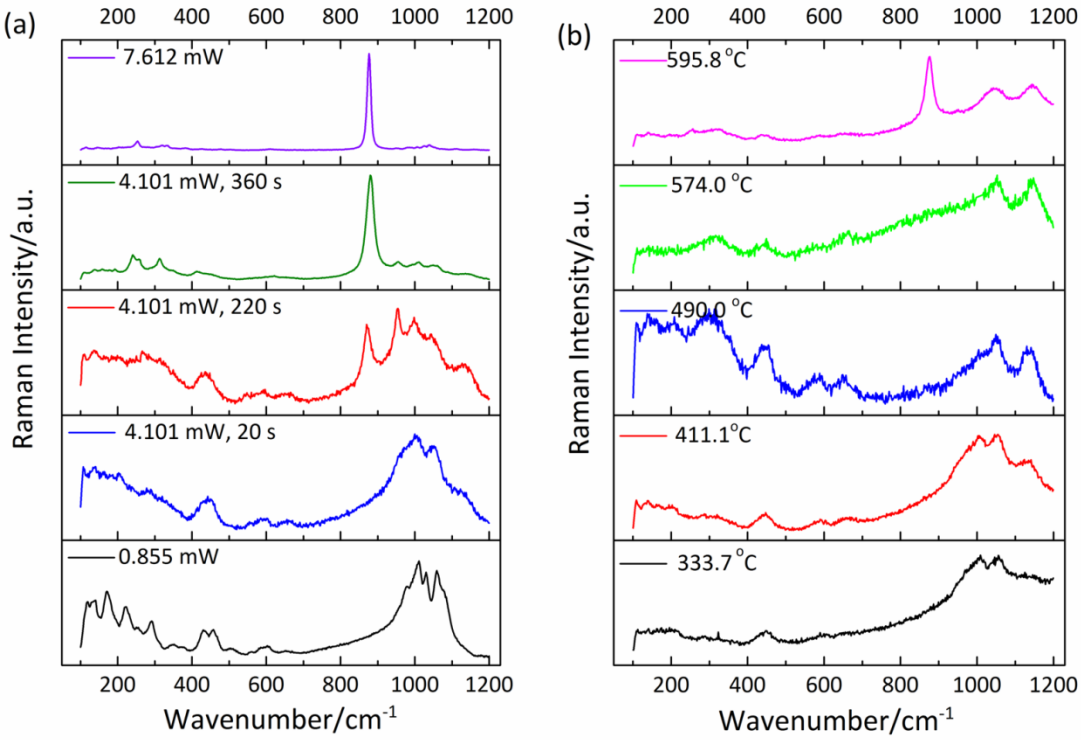

Figure 3.7 Comparison of the Raman spectra of α-$Li_3V_2(PO_4)_3$ at (a) 0.855, 4.101 and 7.612 mW laser power using the 50x objective, acquisition time of 120 s with measurements at (b) 333.7, 411.1, 490.0, 574.0 and 595.8 °C in air using the 50x objective with an acquisition time of 300 s.

of the 876 cm^{-1} mode at 595.8 °C as compared to the spectrum at 7.612 mW indicated two things: the local temperature of the sample under 7.612 mW power was greater than 600 °C and at 600 °C the material was not completely oxidized.

The *in situ* Raman heating experiment was repeated under a N_2 atmosphere. This experiment was done to confirm that α-$Li_3V_2(PO_4)_3$ underwent oxidation under either elevated temperatures or irradiation powers in air and to distinguish any spectral, and therefore structural changes, that could be unrelated to the oxidation reaction. Such structural changes include transformation of lattice symmetry, cell expansion/contraction and atomic disordering. Under N_2, the monoclinic phase is also retained within the 22.3-108. 2 °C temperature range (Figure 3.8(a)). Again, no appreciable peak broadening is noted. As in the heating experiment conducted in air, at 126.1 °C the 1030 cm^{-1} peak and shoulder at 1079 cm^{-1} disappeared. The same spectral characteristics detected at 202.0 °C in air were detected at 195.0 ° C in N_2, which included broadening of the 1009 cm^{-1} peak, merging of the 435 and 455 cm^{-1} modes into a single peak, transformation of the 979 cm^{-1} peak into a shoulder and lowered intensity of the lattice modes (Figure 3.8(b)). Increasing the temperature from 195.0-600.0 °C resulted in no further changes in the spectrum (Figure 3.8(c)). When the material was subsequently cooled down to room temperature the Raman spectrum exactly matched that of the initial α-$Li_3V_2(PO_4)_3$ (Figure 3.9).

$Li_3V_2(PO_4)_3$ is isotypic with $Li_3M_2(PO_4)_3$ where M = Fe, Sc. These crystals are found in the α-phase at room temperature and exhibit two structural phase changes at elevated temperatures (β and γ).[29–31] In the α → β transition, the MO_6 octahedra and PO_4 tetrahedra show a slightly higher symmetry, but the greatest distinction in the structure is the Li ion arrangement.[29] In the α-phase, Li ions are located in three unique positions Li(1), Li(2) and Li(3). The least energetically favorable, Li(3), is repositioned to a new location, Li(1s), which is related in symmetry to Li(1). During the high-temperature

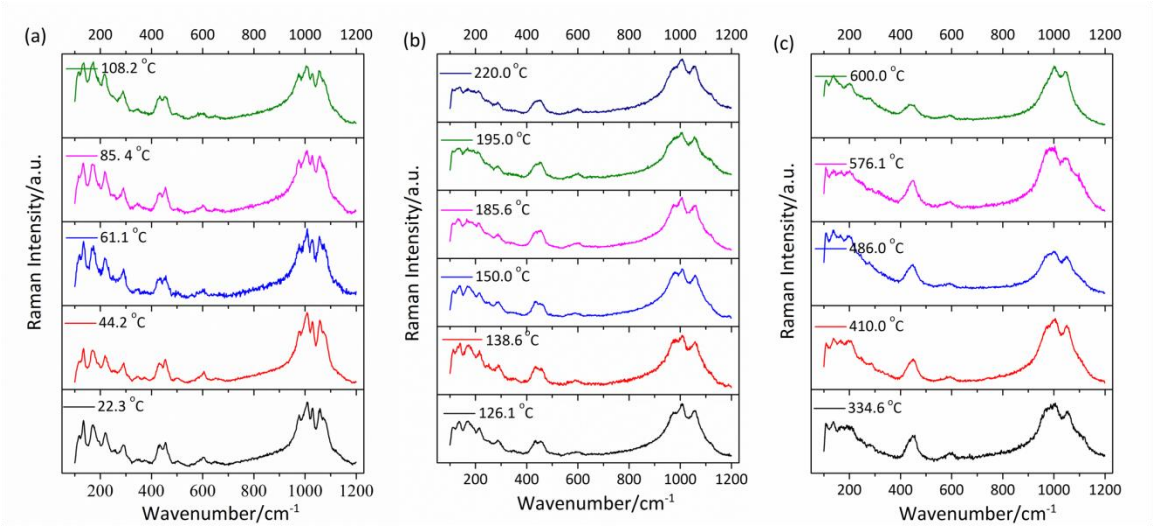

Figure 3.8 *In situ* Raman spectra of α-$Li_3V_2(PO_4)_3$ at different temperatures under N_2: (a) from 22.3-108.2 °C (b) 126.1-220.4 °C and (c) 334.6-600.0 °C taken with a 50x objective and a laser power of 0.855 mW for 300s.

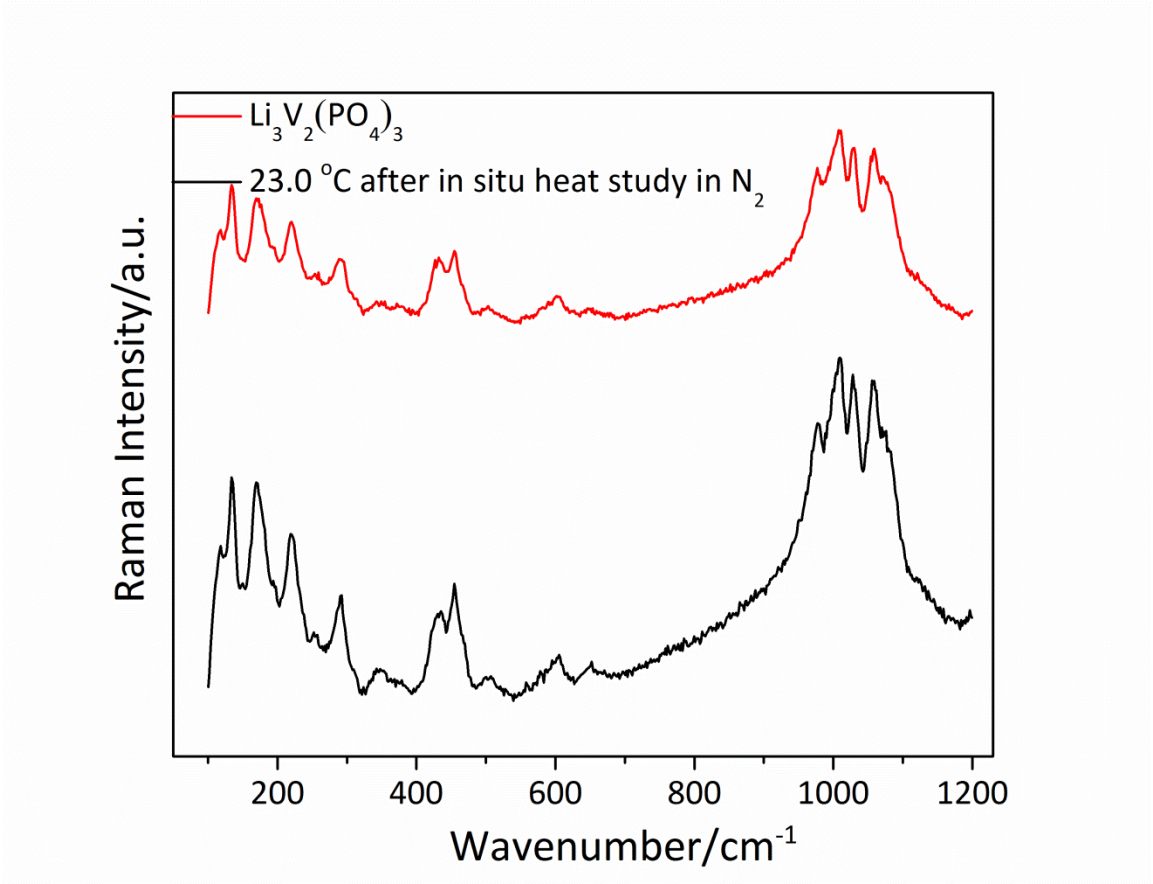

Figure 3.9 Raman measurements at 0.855 mW laser power using the 50x objective, acquisition time of 120 s of the original α-$Li_3V_2(PO_4)_3$ (red) as compared to the sample at room temperature after the *in situ* Raman heating experiments under N_2 (black) showing that the spectrum is reversible after heating the sample to 600 °C under an inert atmosphere.

transition from β → γ, more notable structural transformations occur. The MO_6 octahedra and PO_4 tetrahedra 3-D framework convert from the monoclinic to the orthorhombic structure and all of the Li ions are rearranged. The twelve Li ions of the unit cell are repositioned over three new crystallographic positions where two of the positions are only partially occupied. It is expected that α-$Li_3V_2(PO_4)_3$ also undergoes similar intermediate and high-temperature phase transitions. Differential scanning calorimetry (DSC) studies of α-$Li_3V_2(PO_4)_3$ were completed from 25 °C to 250 °C and then back to 25 °C for a total of three cycles. The first cycle was used to remove any adsorbed water from the material and next two cycles were completed to determine reversibility of the phases. As shown in Figure 3.10, two structural modifications occur at roughly 123 °C (β-phase) and 191 °C (γ-phase).[28, 29] All of the phase transitions were reversible upon cooling back to room temperature (Figure 3.10 & Figure 3.11(a)-(b)).

From the DSC plot, the temperature for the crystalline phase changes of $Li_3V_2(PO_4)_3$ occurred at 123 °C (α → β), 191 °C (β → γ) and from 191 °C and greater the γ-phase is predominant. Undeniably, these crystalline phase changes are responsible for the Raman spectral changes between 23 and 200 °C under N_2 and air (Figure 3.12). However, *in situ* XRD data provided by Bykov et al.[29] has shown evidence of high temperature twinning of α+β, β+γ and even of all three phases at once. Therefore, the spectra in Figure 3.12 may not exclusively represent a single phase. In the β → γ transition there is a more drastic change in structure as compared to the α → β transition. From the Raman spectral changes of the phases the opposite would be expected. Twinning of the phases could explain why the structural and Raman trends don't follow.

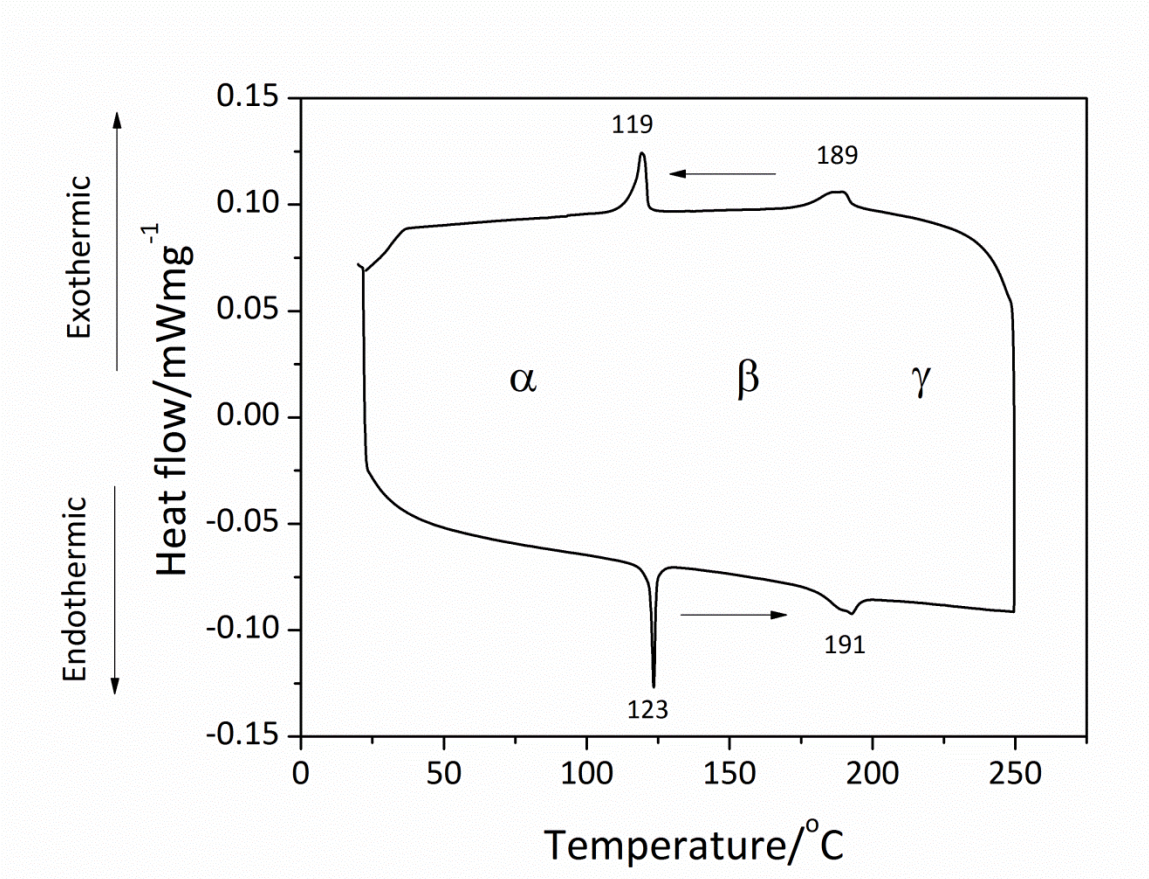

Figure 3.10 DSC curve of α-$Li_3V_2(PO_4)_3$ from 25-250 °C at a rate of 5 °C/min under a N_2 flow rate of 50.00 mL/min.

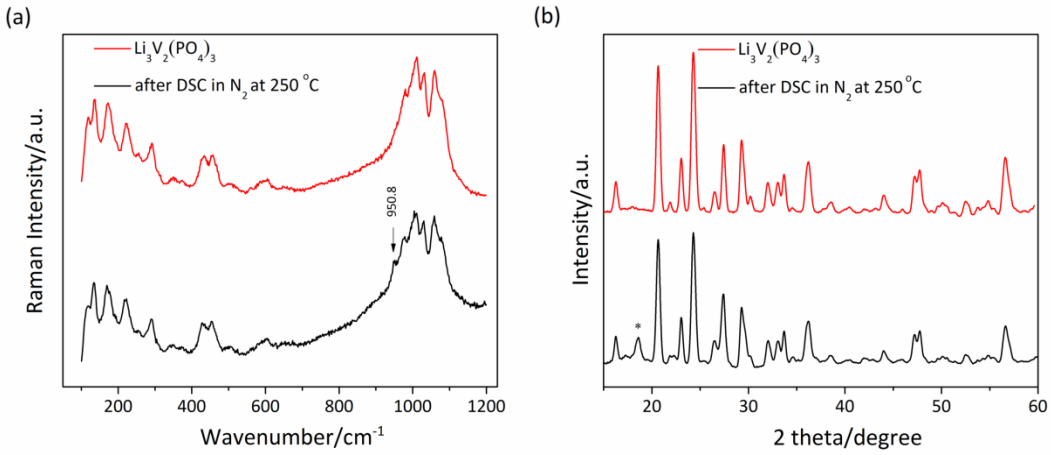

Figure 3.11 (a) Raman and (b) XRD measurements of the original $Li_3V_2(PO_4)_3$ (red) as compared to the sample after DSC analysis under N_2 at 250 °C (black), confirming the reversibility of the α-phase after cooling back to room temperature.

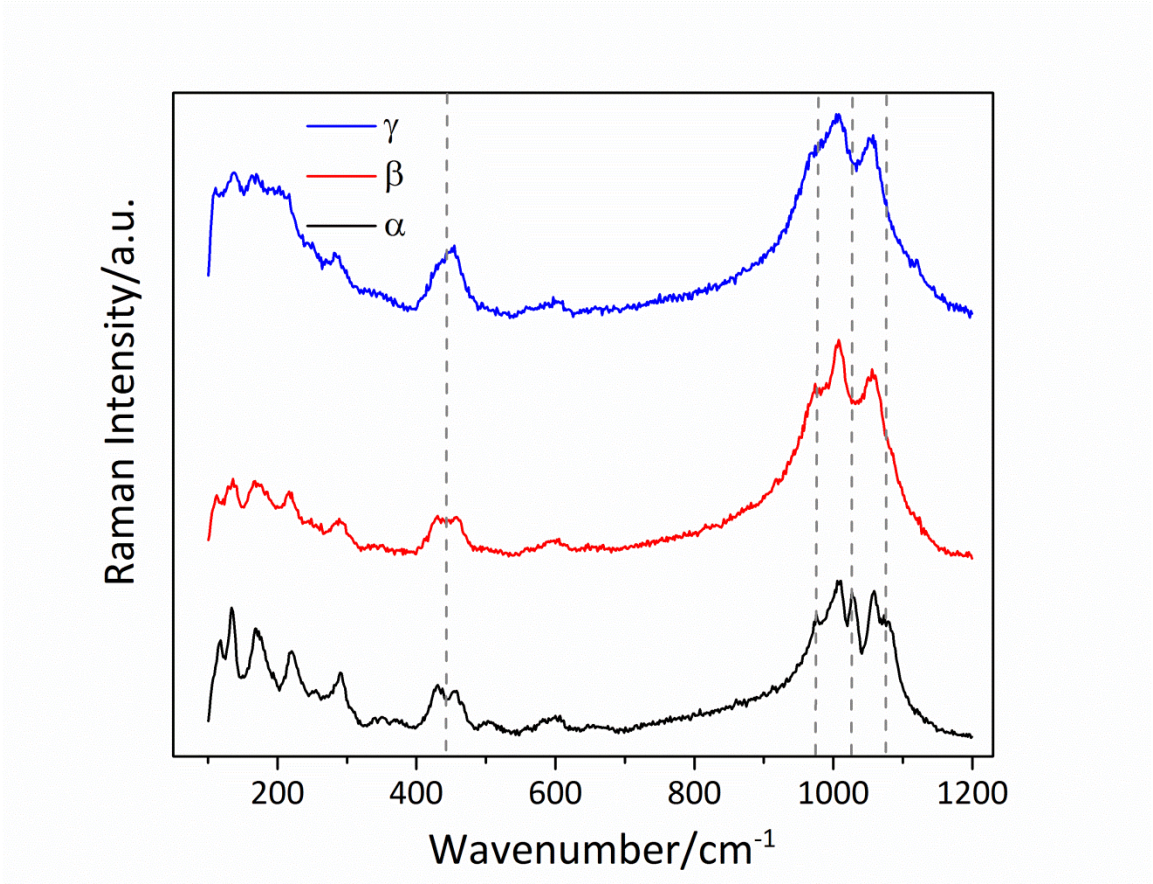

Figure 3.12 Raman spectra of the α, β and γ crystalline phases for α-$Li_3V_2(PO_4)_3$ under N_2.

No crystallographic phase transitions for $Li_3V_2(PO_4)_3$ occurred past 200 °C. Therefore, any Raman spectral changes past this temperature in air must have been induced by oxidation. To prove this hypothesis, TGA under an air flow was used to monitor the weight change of $Li_3V_2(PO_4)_3$ from 25 °C to 800 °C (Figure 3.13(a)). The original 4.437 mg sample initially lost 0.024 mg, corresponding to the evaporation of adsorbed water. After 330 °C the material began to oxidize, and by 800 °C had a ~4% increase in mass.[32] In this case, the originally loose, green powder had sintered into a single, large, olive colored particle.

XRD was conducted thereafter to determine phase impurities. No V_2O_5 was detected. Instead, the material was found to be triclinic $LiVOPO_4$ (P_1 space group) with no $Li_3V_2(PO_4)_3$ detected from the pattern (Figure 3.13(b)). The Raman spectrum included vibrational modes at 1116, 1039, 1028, 993, 956, 685, 615, 536, 332, 255, 148 and 119 cm^{-1} (Figure 3.13(c)). To the best of our knowledge, no Raman literature exists for triclinic α-$LiVOPO_4$. Raman data is, however, reported for rhombohedral β-$LiVOPO_4$.[33] Qualitatively speaking, the spectrum for β-$LiVOPO_4$ correlates well with the Raman spectrum of the oxidized $Li_3V_2(PO_4)_3$ material. The two spectra share the dominating spectral feature as an intense peak close to ~880 cm^{-1} that Baran et al.[33] assigned to the V=O stretching mode. However, the possibility of low concentrations for the partially delithiated phases $Li_{3-x}V_2(PO_4)_3$ $0 < x < 3$, possibly undetectable by XRD, cannot be ruled out. Interestingly, Kuo et al.[34] found through *in situ* XRD studies that α-$LiVOPO_4$ transforms into α-$Li_3V_2(PO_4)_3$ at temperatures above 600 °C under a reducing atmosphere. The present work has identified a new reaction. α-$Li_3V_2(PO_4)_3$ transforms into α-$LiVOPO_4$ at temperatures above 600 °C in oxidizing atmosphere.

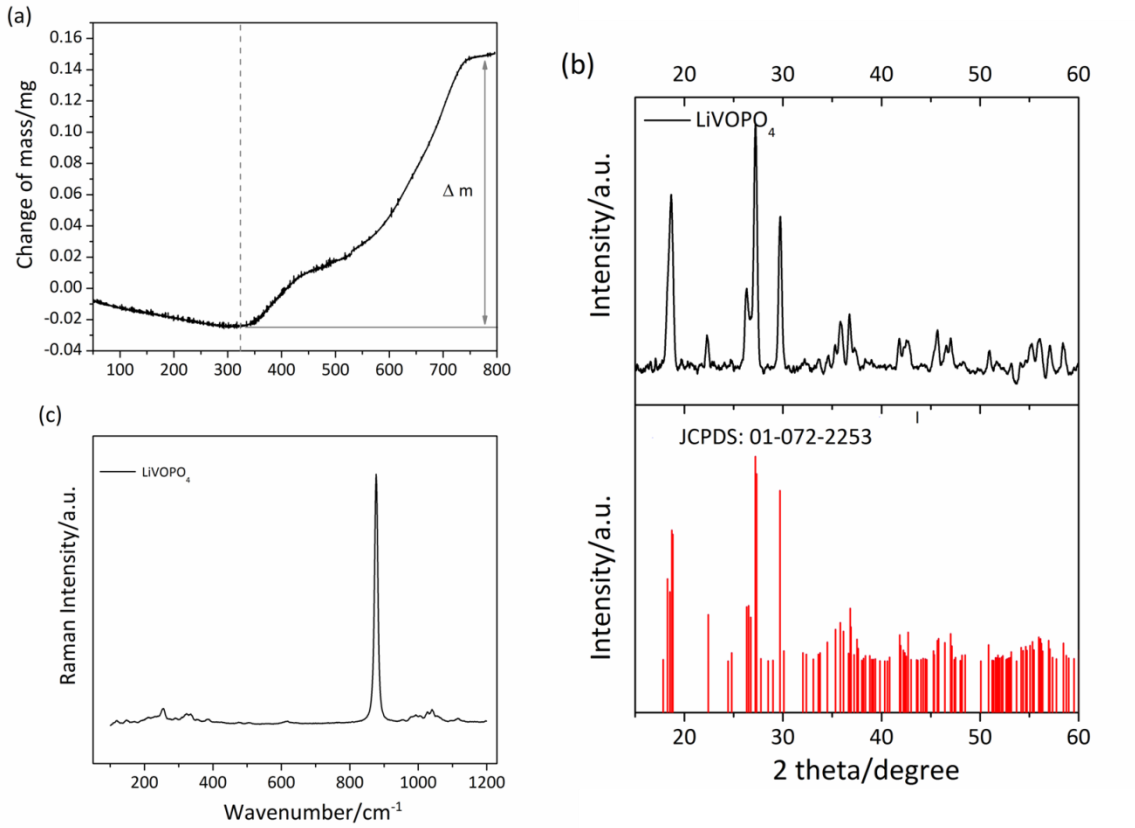

Figure 3.13 (a) TGA curve of α-$Li_3V_2(PO_4)_3$ under air from 25-800 °C. The first ramp was from 25 °C to 500 °C at a rate of 2.50 °C/min. The second ramp continued heating from 500 °C to 800 °C at a rate of 5.00 °C/min. (b) XRD and (c) Raman of the sample after the TGA analysis with the 50x objective at 0.855 mW power with a 120 s acquisition time identifying α-$LiVOPO_4$ as the product of oxidation.

Understanding the behavior of a species under laser irradiation and heating is critical for correct interpretation of micro-Raman experiments. Previously, Burba et al.[7] conducted Raman vibrational studies of α-$Li_3V_2(PO_4)_3$ in the hopes of conducting *in situ* spectroelectrochemical measurements of this material. This study was particularly interested in following the high frequency region of the spectrum assigned to PO_4 valency stretching modes, which are the most intense peaks in the spectrum. However, there were only four weak bands detected in the 1200-850 cm^{-1} region at 1142, 1055, 1011 and 973 cm^{-1}. The spectrum of α-$Li_3V_2(PO_4)_3$ at 411.1 °C also shows similarly broad peaks at 1138, 1053, 1005 and 977 cm^{-1} (Figure 3.8(c)). It is reasonable to suspect that the features found by Burba et al.[7] correspond to thermal degradation of the α-phase into the γ-phase, with the peak at 1138 cm^{-1} indicating oxidation.

3.4 CONCLUSIONS

In this paper we report the experimental Raman spectrum, along with the corresponding theoretical Raman spectrum and symmetry assignments for α-$Li_3V_2(PO_4)_3$ by DFT. Experimentally, only 19 of the 120 Raman modes predicted by factor group analysis were identified. As anticipated, the internal phosphate stretching modes located in the high frequency region contain the sharpest and most intense peaks, making it the prevailing feature of the spectrum. Like $LiFePO_4$, $Li_3V_2(PO_4)_3$ is unstable under certain laser irradiation powers ($\sim \geq 4$ mW) caused by rapid heating and temperature increase under micro-Raman measurements. From our Raman and thermal measurements it was found that the monoclinic phase experiences two thermally induced structural transformations to the β and γ-phases analogous to its isostructural counterparts, $Li_3Sc_2(PO_4)_3$ and $Li_3Fe_2(PO_4)_3$. Continuous heating under air results in oxidation of α-$Li_3V_2(PO_4)_3$ to α-$LiVOPO_4$. These experiments provide fundamental groundwork for

future *in situ* Raman studies of α-$Li_3V_2(PO_4)_3$ as a cathode for lithium-ion storage devices.

3.5 REFERENCES

(1) Yuan, L.-X.; Wang, Z.-H.; Zhang, W.-X.; Hu, X.-L.; Chen, J.-T.; Huang, Y.-H.; Goodenough, J. B. *Energy Environ. Sci.* **2011**, *4*, 269.

(2) Yin, S.-C.; Grondey, H.; Strobel, P.; Anne, M.; Nazar, L. F. *J. Am. Chem. Soc.* **2003**, *125*, 10402.

(3) Huang, H.; Yin, S.-C.; Kerr, T.; Taylor, N.; Nazar, L. F. *Adv. Mater.* **2002**, *14*, 1525.

(4) Lee, S.; Park, S. S. *J. Phys. Chem. C* **2012**, *116*, 25190.

(5) Baddour-Hadjean, R.; Pereira-Ramos, J.-P. *Chem Rev* **2009**, *110*, 1278.

(6) Morcrette, M.; Leriche, J.-B.; Patoux, S.; Wurm, C.; Masquelier, C. *Electrochem. Solid-State Lett.* **2003**, *6*, A80.

(7) Burba, C. M.; Frech, R. *Solid State Ion.* **2007**, *177*, 3445.

(8) Shu, J.; Shui, M.; Xu, D.; Gao, S.; Yi, T.; Wang, D. J.; Li, X.; Ren, Y. *Ionics* **2011**, *17*, 503.

(9) Burba, C. M.; Frech, R. *Appl. Spectrosc.* **2006**, *60*, 490.

(10) Kim, Y. A.; Kojima, M.; Muramatsu, H.; Umemoto, S.; Watanabe, T.; Yoshida, K.; Sato, K.; Ikeda, T.; Hayashi, T.; Endo, M.; Terrones, M.; Dresselhaus, M. S. *Small* **2006**, *2*, 667.

(11) Cahill, L. S.; Chapman, R. P.; Britten, J. F.; Goward, G. R. *J. Phys. Chem. B* **2006**, *110*, 7171.

(12) Yin, S.-C.; Grondey, H.; Strobel, P.; Huang, H.; Nazar, L. F. *J. Am. Chem. Soc.* **2002**, *125*, 326.

(13) Patoux, S.; Wurm, C.; Morcrette, M.; Rousse, G.; Masquelier, C. *Sel. Pap. Present. 11th Int. Meet. Lithium Batter.* **2003**, *119–121*, 278.

(14) Burba, C. M.; Frech, R. *J. Electrochem. Soc.* **2004**, *151*, A1032.

(15) Barj, M.; Lucazeau, G.; Delmas, C. *J. Solid State Chem.* **1992**, *100*, 141.

(16) Butt, G.; Sammes, N.; Tompsett, G.; Smirnova, A.; Yamamoto, O. *J. Power Sources* **2004**, *134*, 72.

(17) Kravchenko, V. V.; Mikhailov, V. I.; Sigarev, S. E. *Solid State Ion.* **1992**, *50*, 19.

(18) Paraguassu, W.; Freire, P. T. C.; Lemos, V.; Lala, S. M.; Montoro, L. A.; Rosolen, J. M. *J. Raman Spectrosc.* **2005**, *36*, 213.

(19) Kohn, W.; Becke, A. D.; Parr, R. G. *J. Phys. Chem.* **1996**, *100*, 12974.

(20) Heyd, J.; Scuseria, G. E.; Ernzerhof, M. *J. Chem. Phys.* **2003**, *118*, 8207.

(21) Kresse, G.; Furthmüller, J. *Comput. Mater. Sci.* **1996**, *6*, 15.

(22) Kresse, G.; Furthmüller, J. *Phys. Rev. B* **1996**, *54*, 11169.

(23) Blochl, P. E. *Phys. Rev. B* **1994**, *50*, 17953.

(24) Kresse, G.; Joubert, D. *Phys. Rev. B* **1999**, *59*, 1758.

(25) pyspglib for ASE, 2013. http://spglib.sourceforge.net/pyspglibForASE

(26) Canepa, P.; Hanson, R. M.; Ugliengo, P.; Alfredsson, M. *J. Appl. Crystallogr.* **2011**, *44*, 225.

(27) Bai, Y.; Yin, Y.; Yang, J.; Qing, C.; Zhang, W. *J. Raman Spectrosc.* **2011**, *42*, 831.

(28) Shebanova, O. N.; Lazor, P. *J. Raman Spectrosc.* **2003**, *34*, 845.

(29) Bykov, A. B.; Chirkin, A. P.; Demyanets, L. N.; Doronin, S. N.; Genkina, E. A.; Ivanov-Shits, A. K.; Kondratyuk, I. P.; Maksimov, B. A.; Mel'nikov, O. K.; Muradyan, L. N.; Simonov, V. I.; Timofeeva, V. A. *Solid State Ion.* **1990**, *38*, 31.

(30) Ohkawa, H.; Yoshida, K.; Saito, M.; Uematsu, K.; Toda, K.; Sato, M. *Chem. Lett.* **1999**, *28*, 1017.

(31) Sato, M.; Ohkawa, H.; Yoshida, K.; Saito, M.; Uematsu, K.; Toda, K. *Proc. 12th Int. Conf. Solid State* **2000**, *135*, 137.

(32) Kuang, Q.; Zhao, Y.; An, X.; Liu, J.; Dong, Y.; Chen, L. *Electrochimica Acta* **2010**, *55*, 1575.

(33) Baran, E. J.; Vassallo, M. B.; Lii, K. H. *J. Raman Spectrosc.* **1994**, *25*, 199.

(34) Kuo, H. T.; Bagkar, N. C.; Liu, R. S.; Shen, C. H.; Shy, D. S.; Xing, X. K.; Lee, J.-F.; Chen, J. M. *J. Phys. Chem. B* **2008**, *112*, 11250.

CHAPTER 4[3]

Electrode/Electrolyte Interface of Composite α-$Li_3V_2(PO_4)_3$ Cathodes in a Non-Aqueous Electrolyte for Lithium Ion Batteries and the Role of the Carbon Additive

4.1 INTRODUCTION

Lithium ion battery technology has been a key component to the success of the portable electronics market. Current research is in heavy pursuit of utilizing this technology for transportation and storage of renewable energies such as solar and wind power. However, the implementation of this technology for transportation and renewable energy applications still faces many challenges in terms of safety, cost, cycle life, energy and power.[1] These challenges are inherent to the active materials used as electrodes as well as the electrolyte for ionic conduction. Currently, transition-metal phosphates (TMPs) possess the highest potential in circumventing these challenges as cathodes for lithium ion batteries (LIBs). These materials have great inherent stability in their structures due to the P-O bond covalency in the metal phosphate framework. The chemical and thermal stability of TMPs make them of particular interest for application in plug-in hybrid electric vehicles (PHEVs). Of the TMPs, olivine $LiFePO_4$ is appealing because of the low toxicity and high abundance of the iron metal. However, $LiFePO_4$ has a low voltage plateau at around 3.4 V vs. Li/Li^+ which results in a comparable gravimetric energy density to the already commercially established $LiCoO_2$.[2]

Consequently, attempts have been made to create other TMPs that have higher operating voltages such as $LiCoPO_4$ (~4.8 V vs. Li/Li^+), $LiMnPO_4$ (~4.1 V vs. Li/Li^+),

[3]Reprinted with permission from Membreño, N.; Park, K..; Goodenough, J.B.; Stevenson, K.J. *J. Mater Chem* **2015**, DOI: 10.1021/acs.chemmater.5b00447. Published Online: April 3, 2015. Copyright 2015 American Chemical Society. Kyusung Park synthesized monoclinic $Li_3V_2(PO_4)_3$. John Goodenough supervised the synthesis of $Li_3V_2(PO_4)_3$. Keith Stevenson supervised XPS characterization of the SEI on $Li_3V_2(PO_4)_3$.

$LiNiPO_4$ (~5.2 V vs. Li/Li^+) and $Li_3V_2(PO_4)_3$ (~3.8 V vs. Li/Li^+ (average)).[3–6] Monoclinic (α) $Li_3V_2(PO_4)_3$ offers a higher voltage plateau than $LiFePO_4$ and has the highest specific gravimetric capacity of any of the TMPs. Additionally, V is a relatively abundant and nontoxic transition metal making it viable for large-scale applications. Structurally, the monoclinic lattice consists of $V_2(PO_4)_3$ lantern units that are positioned perpendicularly to one another. Three energetically distinct lithium ions are found within the interstitial voids of the $V_2(PO_4)_3$ structure.[7] Electrochemically, the extraction of these three lithium ions shows a complex series of two-phase transitions. Another room-temperature phase for $Li_3V_2(PO_4)_3$, the rhombohedral (NASICON) phase exists when synthesized through a distinct synthetic route. In this structure only two lithium ions can be deintercalated in a single two-phase transition. Therefore, the monoclinic phase (α) offers two advantages over the NASICON phase; higher gravimetric capacity and simpler synthetic preparation due to the fact that α-$Li_3V_2(PO_4)_3$ is the most thermodynamically stable phase.[7,8] For the remainder of this article the focus will be on the monoclinic phase of $Li_3V_2(PO_4)_3$.

$Li_3V_2(PO_4)_3$ can be operated in two electrochemical windows, 3.0-4.2 V vs. Li/Li^+ and 3.0-4.8 V vs. Li/Li^+.[8–11] In the 3.0-4.2 V vs. Li/Li^+ window only two lithium ions can be deintercalated/reintercalated into the structure resulting in a theoretical gravimetric capacity of 131 mAh/g. In the 3.0-4.8 V vs. Li/Li^+ window all three lithium ions can be deintercalated/reintercalated (197 mAh/g). However, a major limitation of operating in the larger electrochemical window is that it lies outside the stability window of most non-aqueous organic electrolytes employed in LIBs.[1,12] This could induce oxidative decomposition of the electrolyte. Decomposition products form a surface layer which consists of both insoluble organic species and soluble inorganic species on the surface of the electrode. This layer is called the solid electrolyte interphase (SEI) on anode electrodes. For anode materials in LIBs, the SEI is thought to form on the first discharge

and serves as a protective layer from further decomposition of the electrolyte. The anodic SEI is therefore directly related to the irreversible charge "loss", rate capability, cyclability and overall battery performance.[13] For that reason there have been many studies dedicated to understanding the chemical composition and formation mechanism of the SEI on anodes.[13–17]

However, with further development of higher voltage cathode materials researchers have now directed more attention to understanding the surface chemistry on positive electrodes. One of the most commonly employed electrolytes for LIBs is $LiPF_6$ in ethylene carbonate (EC)/ diethyl carbonate (DEC) which has an approximate stability window of 1.3-4.3 V vs. Li/Li^+.[1,12] Above that window the organic solvent molecules donate an electron to the cathode forming radical cation intermediates. These intermediates then react with other intermediate molecules through a dimerization reaction. The intermediates can also terminate through reactions with solvent molecules or from electron donation of the anode to form partially or fully decomposed products.[18,19] The surface chemistry on cathodes has been predominantly studied on lithium transition metal oxides ($Li_xM_yO_z$). These cathode materials can operate at voltages as high as 5 V where oxidation of the electrolyte is expected. However, it is believed that oxidative decomposition of the electrolyte is greatly suppressed on cathode electrodes by a passivation film that is formed spontaneously before starting the electrochemical reactions. Several mechanisms for the formation of this passivation layer have been proposed.[20,21] Yet it is clear that the LIB community has not reached a consensus on the surface chemistry of cathodes and its effects on battery performance still remain disputable. For the sake of this article, the surface chemistry formed on cathodes will also be referred to as the SEI.

Much less is known about the SEI of TMPs. The covalent bonding in TMPs makes the oxygen less reactive than that in transition metal oxides and therefore less reactive in LIB electrolytes. Most of the work on phosphates has specifically focused on $LiFePO_4$ which operates within the stability window of commonly employed non-aqueous LIB electrolytes. On $LiFePO_4$ the SEI has been described as thin and mainly consisting of salt decomposition products.[22,23] However, for TMPs that operate at high voltages such as $LiMPO_4$ (M = Co, Mn, Ni) and $Li_3V_2(PO_4)_3$ the SEI formed and its effects on lithium intercalation has been greatly neglected.

In these studies we have investigated the SEI of $Li_3V_2(PO_4)_3$ at two operating windows where the performance of this cathode greatly differs. One of the windows was restricted within the stability region of the electrolyte ($LiPF_6$ EC/DEC) and the other outside of those limits. Moreover, we performed aging studies on a $Li_3V_2(PO_4)_3$ composite electrode to understand the inherent stability of the electrode in the electrolyte. Furthermore, because previous studies have focused on understanding the SEI of composite electrodes that include a carbon additive and binder, the chemistry is convoluted. We therefore decided to study the surface chemistry of the individual components after electrochemistry and aging experiments. This methodology permits better understanding of the individual contributions that the components have on the surface chemistry of these composite electrodes. 4.2 Experimental Section

4.2.1 Preparation of α-$Li_3V_2(PO_4)_3$

The solid-state synthesis and characterization of micro-crystalline $Li_3V_2(PO_4)_3$ via X-ray diffraction (XRD) & scanning electron microscopy (SEM) has previously been described by our group.[24] The material can be indexed to the monoclinic space group $P2_1/n$ and ranges from 0.1-50 μm in size.

4.2.2 Electrochemical Analysis

$Li_3V_2(PO_4)_3$ was tested in the standard CR2032 coin-cell assembly. The cathode was made from a mixture of 85% α-$Li_3V_2(PO_4)_3$, 12% Super P® Li (TIMCAL) and 3% polytetrafluoroethylene (PTFE) (Acros Organics). The powder mixture was rolled into a thin sheet from which circular pellets of about 4 mg were punched. Coin cells were assembled with lithium metal as the anode, Celgard® as the separator and 1 M $LiPF_6$ in 1:1 EC/DEC as the electrolyte (Novolyte). The SEI on $Li_3V_2(PO_4)_3$ was monitored by galvanostatic charge/discharge experiments carried out with an Arbin BT2000 battery tester at a rate of C/20 with a potential window between 3.0 and either 4.2 or 4.8 V vs. Li/Li^+. The cells were cycled for 1,5,10 & 50 cycles. Additionally, a coin cell was aged at open-circuit potential (OCP) for a duration of 60 & 120 days to test for spontaneous SEI formation.

4.2.3 X-ray photoelectron spectroscopy (XPS)

Once galvanostatic cycling was completed, the OCP of each cell was monitored until reaching equilibrium ($\pm$ 0.01 V). The cells were then disassembled and the $Li_3V_2(PO_4)_3$ composite cathodes were washed 3 times with ~1 mL of DEC. Prior to analysis, each electrode was stored in a container within the glovebox (MBraun) maintained with an Ar atmosphere containing <0.1 ppm H_2O and <5.0 ppm O_2. The electrodes were transported from the glovebox to a Kratos Axis Ultra DLD XPS (Al Kα source), ultra-high-vacuum chamber using reduced oxidation interface (RoX) as previously described by our group.[17] This interface contains a set of built-in figures of merit that were used to verify that samples were not exposed to traces of oxygen (anoxic) and moisture (anhydrous) during transport. XPS measurements were taken on a 300 by 700 μm spot size. Survey scans were collected with a 1.0 eV resolution, 300 ms dwell time and 80 eV bandwidth. High-resolution scans of C 1s, O 1s, Li 1s, V 2p, P 2p, and F

1s regions were accumulated and averaged from 3 measurements with 0.1 eV resolution, 800 ms dwell time and 20 eV bandwidth. Spectra were analyzed with CasaXPS processing software (version 2.3.15, Casa Software Ltd.). High-resolution spectra were fit to determine the chemical compositions of the SEI. Relative sensitivity factors (RSFs) from the VISION software library (Kratos Analytical) were used to compare the areas under peaks associated with the various elements. Shirley backgrounds were used to fit the V and Li spectra. All other elements (nonmetals) were fit with linear backgrounds. All fits were the sum of multiple Voight functions, 30% Lorentzian and 70% Gaussian. All spectra were calibrated to the sp^2 carbon peak at 284.4 eV. However, absolute binding energies are slightly higher than found in the literature due to non-uniform charging effects of non-conducting micro-domains consisting of salt residuals and reduction products on the surface. When there was significant sample charging, the sample was neutralized with a low energy electron gun (<1.8 A). The amp setting used for the charge neutralizer was carefully selected since islands of insulating Teflon binder in the composite electrodes can result in artifacts and peak distortion at >1.8 A (Figure 4.1(a)-(b)). A Marquardt algorithm was used to fit the peaks of the components to the signal. 4.3 Results and Discussion

4.3.1 Electrochemistry of $Li_3V_2(PO_4)_3$

As shown in Figure 4.2(a) the charging profile (lithium deintercalation) of $Li_3V_2(PO_4)_3$ shows a complex series of two-phase transitions. The voltage plateaus in the charging curve correspond to phase transitions between the single phases of $Li_xV_2(PO_4)_3$:

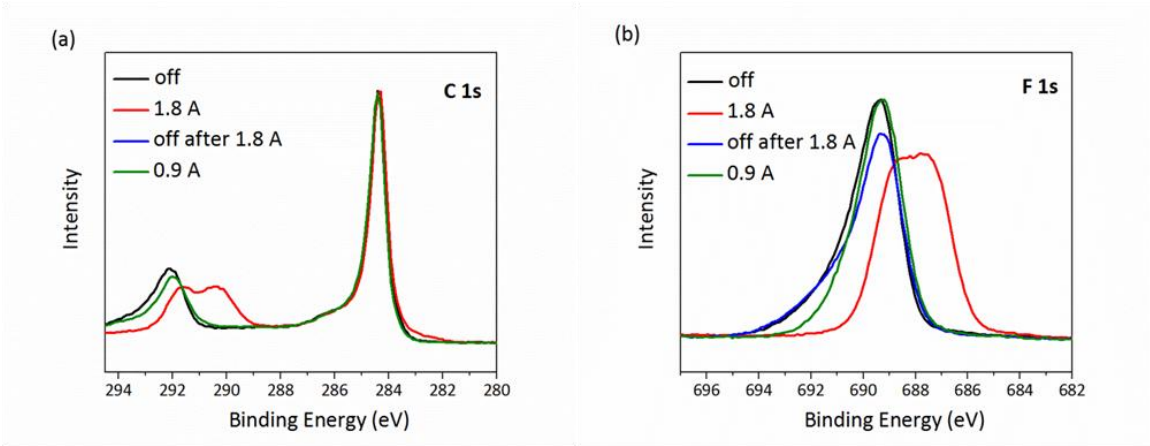

Figure 4.1 (a) C 1s & (b) F 1s spectra of Teflon binder without the charge neutralizer (black), with the charge neutralizer on at 1.8 A (red), without the charge neutralizer after being exposed to 1.8 A (blue) and with the charge neutralizer on at 0.9 A.

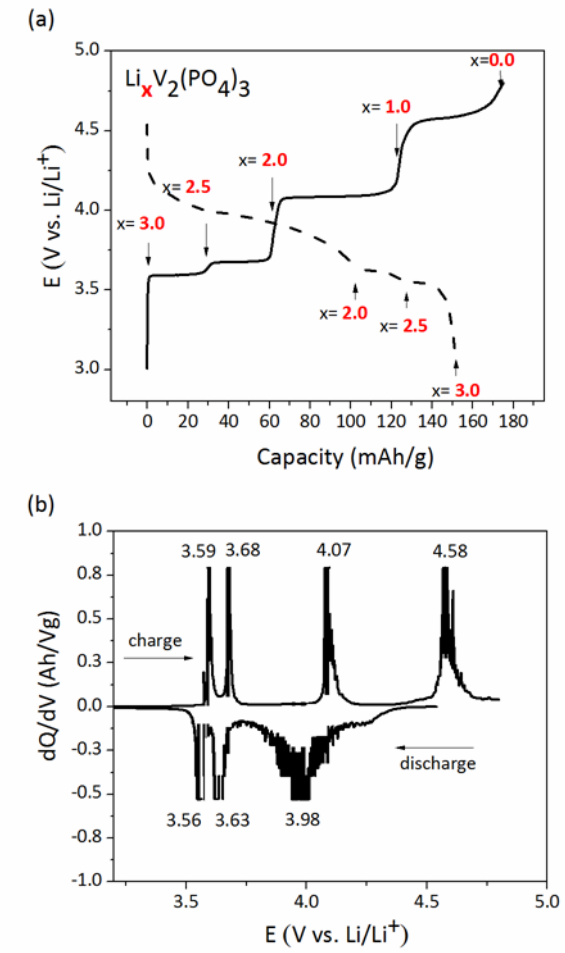

Figure 4.2 (a) Charge/discharge curve of composite $Li_3V_2(PO_4)_3$ electrode showing the stoichiometries of the different phases formed during charging (lithium deintercalation) and discharging (lithium reintercalation). (b) Incremental capacitance plot of the charge/discharge curve labeled with the potentials of the two-phase transitions.

x= 3.0, 2.5, 2.0, 1.0 and 0.0. It was found by Yin et al. that charge ordering and lithium site ordering drive these phase transitions.[7,25] Once the $V_2(PO_4)_3$ framework is completely delithiated, there is no valence ordering to drive the phase transitions and therefore solid solution behavior is seen (sloping voltage) during the reverse process of discharging (lithium reintercalation). When valence ordering is restored the phase transitions are again present.[7] Figure 4.2(b) is an incremental capacitance plot of the charge/discharge curve with the potentials of the two-phase transitions labeled. All three lithium's can be reversibly deintercalated and reintercalated from this material at even fast cycling rates.

However, after the first cycle, the voltage plateaus that indicate two-phase transitions begin to take on a slope-like characteristic (Figure 4.3(a)). Moreover, there is an increase in overpotential associated with the two-phase transitions with increasing cycle number. If the potential window is limited to 3.0-4.2 V vs. Li/Li^+ (Figure 4.3(b)), where only two lithium ions can be deintercalated, the phase transitions are reversible even after 40 cycles. In this electrochemical window an increase in overpotential with increasing cycle number can also be seen, but it is much less severe. The performance of $Li_3V_2(PO_4)_3$ also differs significantly in the two potential windows with respect to the charge capacity and the Coulombic efficiency (Figure 4.3(c)). From the galvanostatic cycling experiments, the initial gravimetric charge capacity (1^{st} cycle) in both electrochemical windows is close to the theoretical capacity (197 mAh/g in the 3.0-4.8 V vs. Li/Li^+ window and 131 mAh/g in the 3.0-4.2 V vs. Li/Li^+ window). However, with further cycling, the gravimetric charge capacity rapidly fades in the 3.0-4.8 V vs. Li/Li^+ window whereas in the 3.0-4.2 V vs. Li/Li^+ window it remains stable over multiple electrochemical cycles. Similarly, the Coulombic efficiency over multiple electrochemical cycles remains stable in the 3.0-4.2 V vs. Li/Li^+ window whereas in the

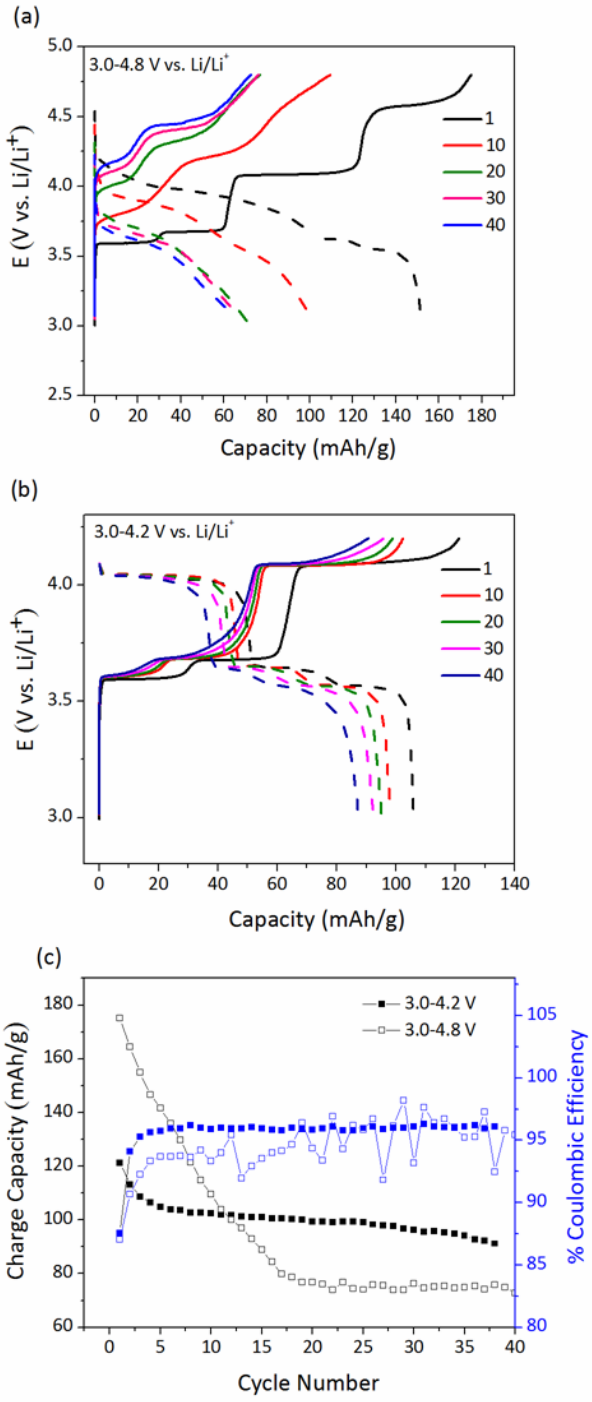

Figure 4.3 Charge/discharge curves of composite $Li_3V_2(PO_4)_3$ electrode in the (a) 3.0-4.8 V & (b) 3.0-4.2 V vs. Li/Li^+ window at 1 (black), 10 (red), 20 (green), 30 (magenta) & 40 (blue) cycles. (c) Comparison of the gravimetric charge capacity (black) and Coulombic efficiency (blue) vs. cycle number for $Li_3V_2(PO_4)_3$ at the two electrochemical windows: 3.0-4.8 V (empty square) & 3.0-4.2 V vs. Li/Li^+ (filled square).

3.0-4.8 V vs. Li/Li^+ window it fluctuates.One notable feature that is seen in both electrochemical windows is that the Coulombic efficiency is lowest in the 1st cycle and then increases after the second cycle. This irreversibility in the first cycle is thought to be attributed to the decomposition of the electrolyte forming a film on the surface of the electrode. This surface film has been referred to as the solid electrolyte interphase (SEI). The SEI on $Li_3V_2(PO_4)_3$ was prepared electrochemically by galvanostatic charge/discharge experiments in the 3.0-4.2 or 4.8 V vs. Li/Li^+ window prior to XPS characterization.

4.3.2 XPS Characterization of the SEI

The chemical composition of the SEI on $Li_3V_2(PO_4)_3$ composite electrodes was determined by XPS. High-resolution scans were collected from the C 1s, O 1s, Li 1s, P 2p, F 1s and V 2p energetic regions after 1, 5, 10 and 50 cycles. Spectra of the pristine composite electrode in the same energetic regions are included for comparison (Figure 4.4(a)-(f)). As mentioned in the experimental section, the composite electrode includes the active material, $Li_3V_2(PO_4)_3$, a conductive carbon additive and polytetrafluoroethylene (PTFE) binder. In Figure 4.4(a) the C 1s spectrum of the pristine electrode shows two major peaks. The peak of highest intensity at 284.4 eV corresponds to the sp^2 hybridized C-C bond from the carbon additive.[26,27] The peak of second highest intensity positioned at 292.4 eV is assigned to the CF_2 functional group of the PTFE binder (positioned at 689.4 eV in the F 1s spectrum).[28] From the C 1s spectrum of the pristine electrode, there is evidence of only slight oxidation of the graphitic carbon (the oxidized carbon peaks are more apparent in the O 1s spectrum). The following binding energies were experimentally determined for $Li_3V_2(PO_4)_3$: 55. 2 eV for Li 1s, 516.9 eV

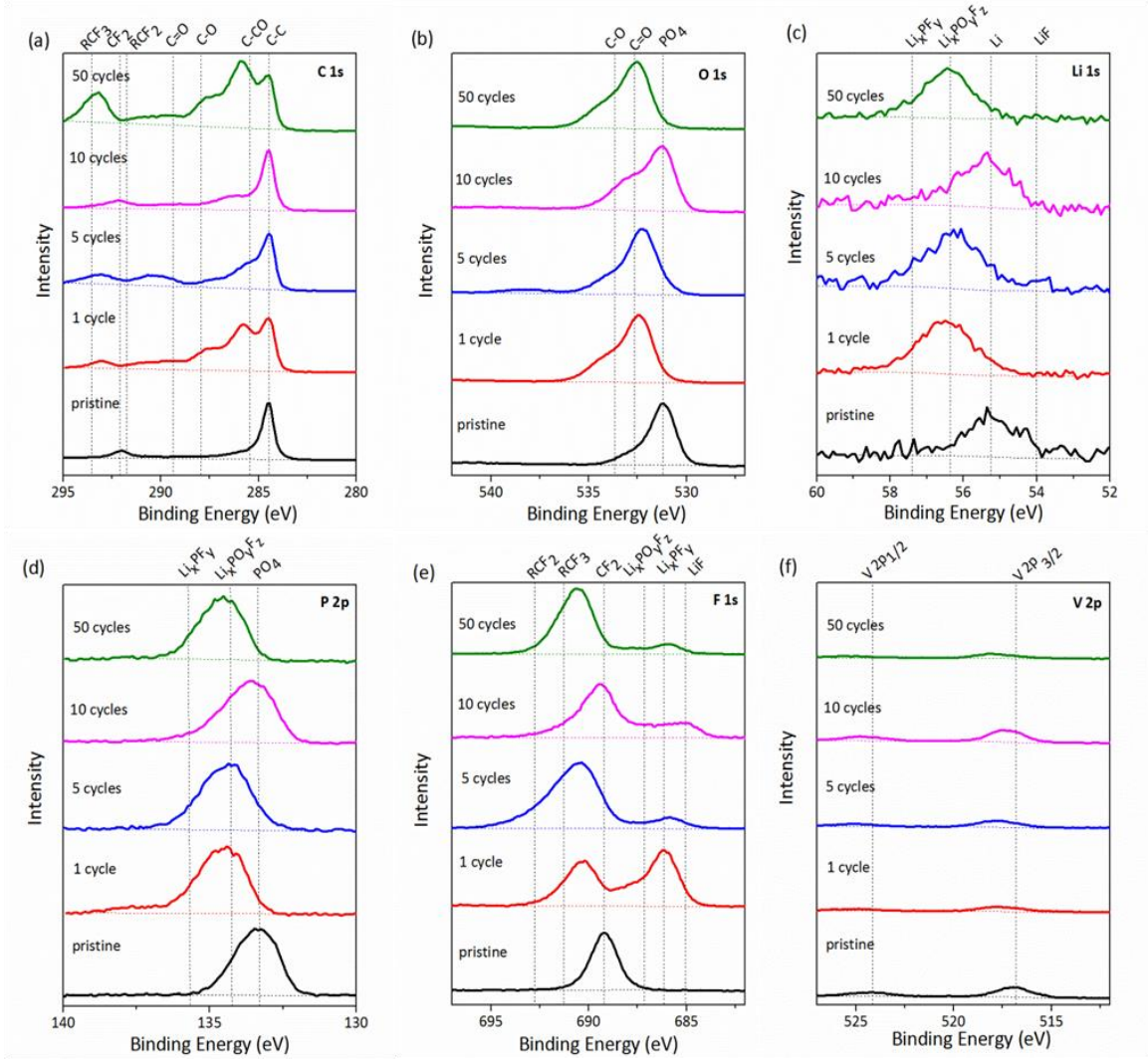

Figure 4.4 (a) C 1s (b) O 1s (c) Li 1s (d) P 2p (e) F 1s and (f) V 2p XPS spectra of a composite $Li_3V_2(PO_4)_3$ electrode after 0 (black), 1 (red), 5 (blue), 10 (magenta) and 50 (green) cycles in the 3.0-4.8 V vs. Li/Li^+ window.

for V $2p_{3/2}$ (524.2 eV V $2p_{1/2}$), 133.4 eV for P 2p and 531.1 eV for O 1s. These values match well with previous reports.[26,29] Since elements in the substrate (composite electrode) are also found on the surface, (SEI) fitting of the peaks must be carefully conducted to properly deconvolute the chemistry of these two regions. Figure 4.5(a)-(d) shows an example of curve fitting XPS spectra with functional group assignments.

Our group has previously characterized the SEI on crystalline silicon anodes.[17] Assignments for the polymeric species followed Beamson and Briggs.[28] Additionally, Verma et al.'s carbon anode SEI assignments were also followed, which include salt-decomposition products of $LiPF_6$.[13] Similarly, we followed the binding energy assignments reported in that work. For the C 1s spectra the peak of highest intensity was assigned to the C-C single bond corresponding to alkane and alkyl functional groups as well as residual adventitious carbon. Peaks adjacent to the C-C single bond at higher binding energies were assigned to carbon functionalities with higher oxidation states. Curve fitting of these components was included to account for the asymmetry of the C-C bond peak. The areas under the oxidized C 1s peaks were matched with the corresponding peak areas from the O 1s spectra to obtain quantitative data for the organic functionalities. Following the fits for the organic functionalities, the inorganic functionalities were fit in a similar manner. A more detailed explanation of peak fitting and binding energies of the different functionalities for the SEI on LIB electrodes can be found in our group's previous report.[17]

Figure 4.4(a)-(f) shows the XPS spectra for the $Li_3V_2(PO_4)_3$ composite electrode galvanostatically cycled in the 3.0-4.8 V vs. Li/Li^+ window. From the C 1s spectra (Figure. 4.4(a)) it is evident that components corresponding to the SEI film are formed after the first galvanostatic cycle. The C 1s and O 1s spectra primarily identify the

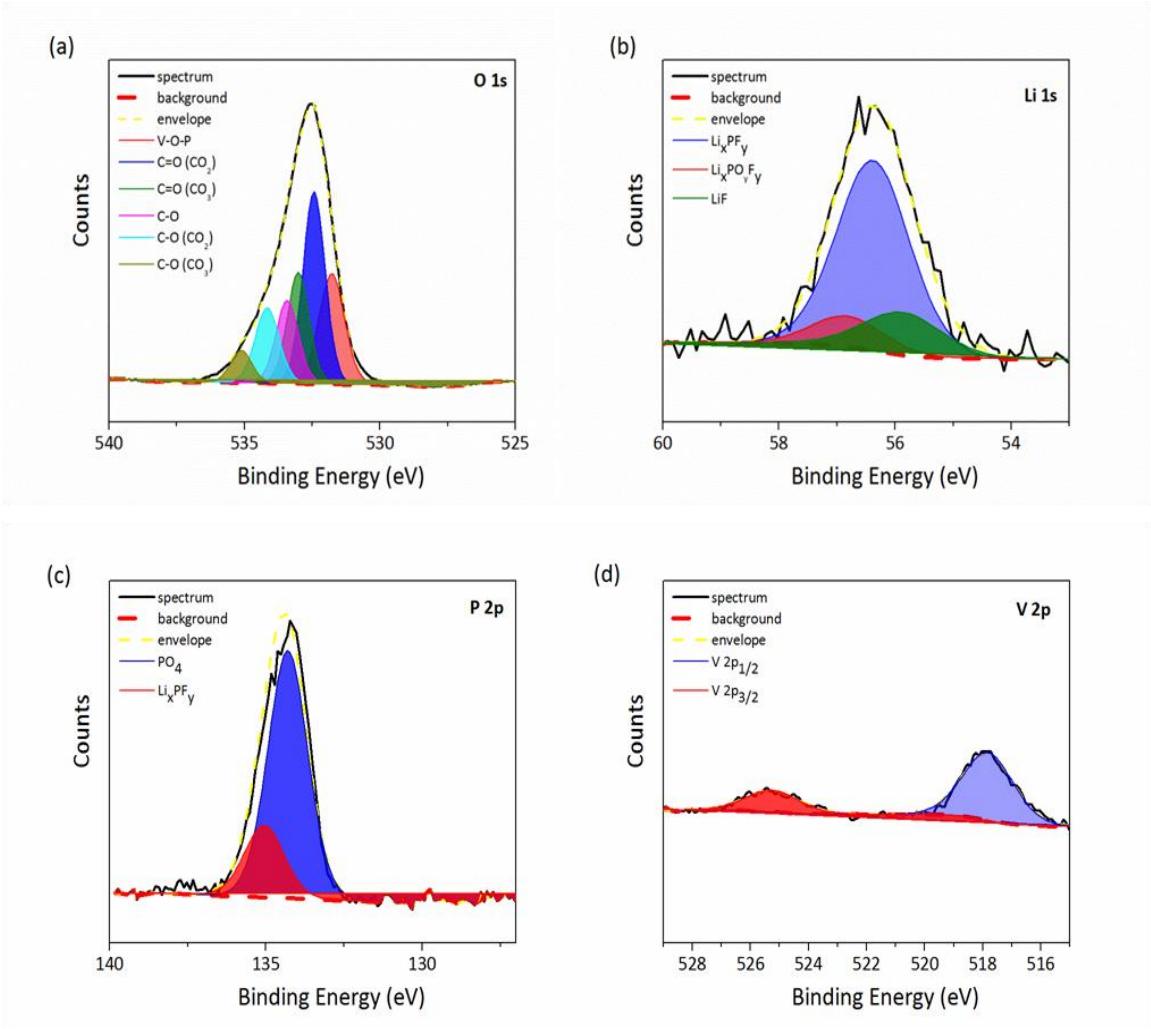

Figure 4.5 Deconvoluted (a) O 1s (b) Li 1s (c) P 2p and (d) V 2p XPS spectra of a composite $Li_3V_2(PO_4)_3$ electrode aged in the 1M $LiPF_6$ 1:1 EC/DEC electrolyte for 60 days.

organic, insoluble species that are contained on the surface of the SEI (Figure 4.4(a) and (b)). These species are identified as ethers, alkoxides, esters, carboxylates and carbonates. Furthermore, the C 1s and F 1s (Figure 4.4(a) and (f)) spectra identify fluoroalkane species. From the Li 1s, P 2p and F 1s spectra (Figure 4.4(c)-(e)) the inorganic species were determined to be LiF and degraded lithium salts ($Li_xPO_yF_z$ and Li_xPF_y). The reactions responsible for the spontaneous degradation of $LiPF_6$ in the presence of atmospheric moisture have been well-established.[30] After further galvanostatic cycling (5, 10 and 50 cycles) the same organic and inorganic functionalities are found with varying intensities indicating that the chemistry of the SEI does not vary qualitatively, but rather quantitatively. Additionally, V 2p spectra (Figure 4.4(f)) were collected for the cycled electrodes even though no vanadium-containing compounds are thought to be present in the SEI. However, due to the fact that the depth resolution of XPS is estimated to be 10 nm, the V 2p spectra can indicate a relative thickness of the SEI. Throughout the different galvanostatic cycles, the $V2p_{½}$ and $_{3/2}$ peaks are present indicating that the SEI thickness is less than 10 nm during the first 50 cycles. No trend in thickness can be seen with increasing cycle number. These results suggest that under these conditions the SEI film is self-limiting.

XPS spectra in the same energetic regions were collected for $Li_3V_2(PO_4)_3$ composite electrodes in the 3.0-4.2 V vs. Li/Li^+ window after galvanostatic cycling (Figure 4.6). The stability window for $LiPF_6$ DEC/EC electrolyte is thought to be between 1.3-4.5 V vs. Li/Li^+ and therefore no SEI formation is expected. Yet it has been reported that an SEI was found on $Li_3V_2(PO_4)_3$ electrodes through FT-IR characterization in this same potential window.[29] Researchers have claimed that the potential limit of anodic stability for non-aqueous electrolytes can depend on the cathode used because of varying catalytic effects from the metal. Our XPS results confirm that an SEI is formed on

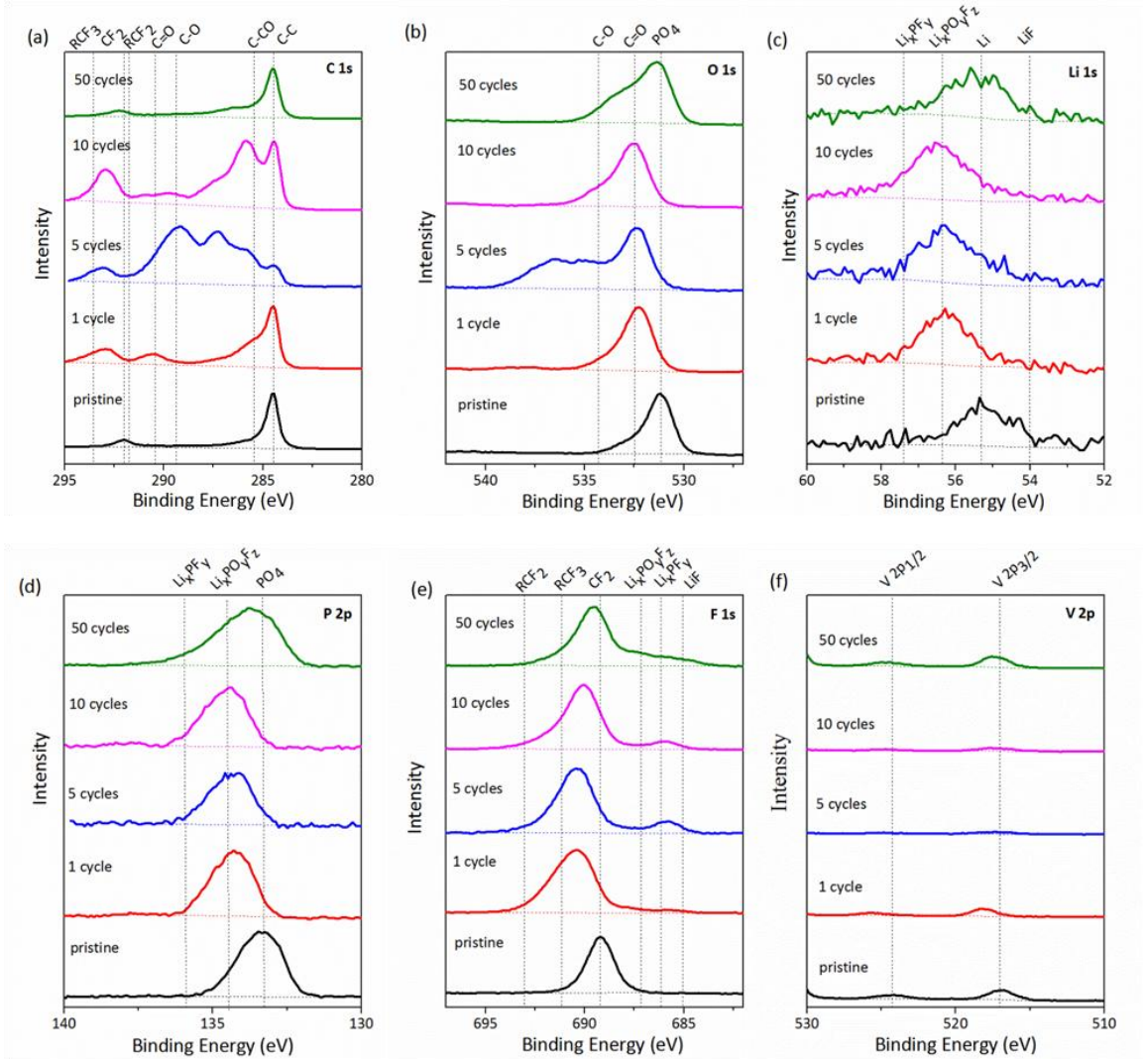

Figure 4.6 (a) C 1s (b) O 1s (c) Li 1s (d) P 2p (e) F 1s and (f) V 2p XPS spectra of a composite $Li_3V_2(PO_4)_3$ electrode after 0 (black), 1 (red), 5 (blue), 10 (magenta) and 50 (green) cycles in the 3.0-4.2 V vs. Li/Li^+ window.

$Li_3V_2(PO_4)_3$ composite electrodes in the 3.0-4.2 V vs. Li/Li^+ electrochemical window (Figure 4.6(a)-(f)). Figure 4. also shows that SEI growth begins after the first cycle with similar species present. The SEI thickness and composition (quantitatively) evolves with no particular pattern as noted in the 3.0-4.8 V vs. Li/Li^+ window.

4.3.3 SEI on Anode vs. Cathode

The SEI formed on anode materials for LIBs has been extensively studied. Mechanistically, the SEI is formed through the donation of an electron from the anode to a solvent molecule (such as EC and vinylene carbonate (VC)) reducing it into a radical anion intermediate through hemolytic ring opening. The intermediate radical molecule formed is then terminated through dimerization reactions with other solvent molecules as well as through reactions with other intermediate molecules.[15] Simultaneously, salt reduction takes place also depositing on the surface of the anode material. The thickness of the SEI may vary from tens to hundreds of Å.[13] Depth profiling studies have described the SEI on anodes as having multiple, but separate layers with distinct compositions.[22,31,32] Although, recent studies have described the SEI structure as a layer consisting of poly-hetero microphases.[33]

Although the SEI on anodes has been thoroughly studied for the past decades, little attention has been paid to the surface chemistry on cathodes. Surface studies are of particular importance for $Li_xM_yO_z$ cathodes that operate at high voltages of up to 5 V vs. Li/Li^+. At such high voltages, oxidative decomposition of the electrolyte takes place. From theoretical studies, it has been proposed that EC coordinates with the PF_6^- anion (due to its high dielectric constant) and therefore reaches the cathode most easily, resulting in preferential oxidation on the cathode. Radical cation $EC^{\cdot+}$ is formed from a one electron transfer from EC to the cathode. Several radical cations are possible from

the decomposition of $EC^{\cdot+}$ which are terminated by gaining one electron from the anode or solvent molecule forming alkyl carbonate oligomers.[18,19] Experimentally, the oxidation products have been found on metal electrodes (Au, Pt & Al) to include carboxyl and aldehyde groups as well as oligomers of alkyl carbonates.[34] With these metal, inert electrodes, no surface film arises after oxidative decomposition of the solvents. However, it is thought that unlike the inert electrodes, $Li_xM_yO_z$'s do form a surface film after decomposition of the electrolyte.[20,21,35–37]

Initially it was thought that the SEI was formed from an oxidation and precipitation reaction of the solvent molecules to form insoluble products as has been suggested from theoretical calculations. However, the surface chemistry of $Li_xM_yO_z$ cathodes has proven to be complex even before oxidative decomposition begins. Pristine $Li_xM_yO_z$ electrodes are thought to contain Li_2CO_3 on the surface which is formed from atmospheric CO_2 reacting with lithium ions from the electrode.[20] Thereafter, a surface passivation film is formed spontaneously after immediate contact with the electrolyte. This prevents the continuous oxidative decomposition of the electrolyte. Upon cycling, the surface film of these electrodes contains several species with $ROCO_2Li$ being the major product. Various mechanisms have been proposed for the formation of this passivation film. Some believe that a nucleophilic reaction takes place where the negatively charged oxygen (nucleophile) attacks a carbon atom (electrophile) from the solvent molecule.[35,36] Another less widely accepted mechanism suggests the possibility that $ROCO_2Li$ species formed on the anode saturate the solution and then reprecipitate on the cathode.[35] Lastly, it has been proposed that reduction products from the electrolyte form on the surface during spontaneous lithium deintercalation of the cathode.[21] Aging studies of $Li_xM_yO_z$ electrodes in the salt and solvents without applying an electrochemical bias have proven that these materials are intrinsically reactive with the

electrolyte. These spontaneous reactions have been primarily studied on $LiNiO_2$, $LiCoO_2$, $LiMn_2O_4$ and mixed-metal oxide electrodes by reflectance FTIR and XPS. However, the SEI chemistry as well as the formation mechanism still remains controversial. Some experimental evidence indicates that the SEI on $Li_xM_yO_z$ cathodes thickens with cycle number, time and temperature. For the SEI on anodes, an even slightly elevated temperature causes it to break down and has to be reformed on the subsequent reduction cycle. Because of these differing properties, it has been referred to as a solid permeable interface (SPI) instead of the term used for anodes, SEI.[20] Furthermore, depth profiling data describes the cathode SEI as consisting of polymer/polycarbonate nearest to the cathode surface followed by layers of LiF and degraded salt products (P_2O_5, Li_xPF_y and $Li_xPO_yF_z$) at the very top of the surface film.[20,38]

4.3.4 SEI on TMPs

The SEI of TMPs has recently been investigated. Of the TMPs the material of most interest $LiFePO_4$, operates within the stability window of common non-aqueous electrolytes. Therefore, no surface chemistry from oxidative decomposition is expected. However, TMPs such as $LiCoPO_4$ and $Li_3V_2(PO_4)_3$ operate well beyond the electrochemical window of the same electrolytes. Therefore, understanding the surface interface of metal phosphates is crucial. However, there are very few studies on these high-voltage phosphate materials. Edstrom and co-workers conducted non-destructive depth profiling of cycled $LiFePO_4$ electrodes. Their conclusion for the SEI on $LiFePO_4$ electrodes was that it was thin and mostly consisted of salts.[20] Depth profiling showed that further into the SEI more oxidized carbon species could be found which they attributed to either decomposed electrolyte species or to corrosion products of the additive carbon.[22] Castro et al. similarly investigated cycled $LiFePO_4$ electrodes focusing

mainly on the reversibility of the Fe^{2+}/Fe^{3+} couple via XPS measurements.[23] The SEI on $LiFePO_4$ was described as thin and consisting mostly of salt products which they attributed to the low reactivity of $LiFePO_4$. After 200 cycles the SEI was still seen to be present with some degree of dissolution and destabilization. Due to interfering peaks of the binder and of the phosphate group, no assignments were attempted for electrolyte decomposition products.

Literature on the SEI of $Li_3V_2(PO_4)_3$ is even more scarce. Chen et. al investigated the electrode/electrolyte interface of carbon coated $Li_3V_2(PO_4)_3$ in $LiPF_6$ based electrolytes specifically within the 3.0-4.3 V vs. Li/Li^+ region.[29] Capacity loss was only noted initially (first 10 cycles). Thereafter, the capacity remained stable for several hundreds of cycles. This observation was related to a progressive formation of SEI in the initial cycles that later stabilized. Through ex situ FTIR measurements, the species identified were $ROCO_2Li$, RCO_2Li, Li_xPF_y and $Li_xPO_yF_z$.

4.3.5 SEI on $Li_3V_2(PO_4)_3$

In this study we decided to investigate the SEI of $Li_3V_2(PO_4)_3$ in both electrochemical windows (3.0-4.2 & 4.8 V vs. Li/Li^+). This material shows drastically different electrochemical performance depending on the charging potential applied. At 4.8 V where carbonate-based electrolytes are no longer stable, oxidative decomposition is likely to take place. However, limiting the charge potential to 4.2 V maintains the stability of the electrolyte. Yet, Chen at al. identified that the surface chemistry of this material upon cycling up to 4.2 V is rich in species characteristically contained in an SEI layer. This led us to investigate the material at both operating windows to understand how the surface chemistry differed and how that directly relates to the difference in electrochemical performance. Furthermore, it has been widely accepted that $Li_xM_yO_z$

cathodes form an SEI spontaneously due to the basicity of the oxygen, yet to our knowledge aging studies have not been conducted on $Li_3V_2(PO_4)_3$ nor $LiFePO_4$ to determine how aging effects the surface during cycling. Our studies show that in the 3.0-4.2 V vs. Li/Li^+ window, the SEI remains thin (< 10nm) as was reported for $LiFePO_4$ in a similar voltage region. However, even in the wider 3.0-4.8 V vs. Li/Li^+ window, the V 2p signal is still present indicating that the SEI does not differ much in thickness. Similar to the SEI literature reported on $Li_3V_2(PO_4)_3$, these experiments identify $ROCO_2Li$ (carbonate) and RCO_2Li (carboxylate) species. In addition, alkoxide and ether products were identified. Degradation products from the electrolyte salt ($Li_xPO_yF_z$, Li_xPF_y and LiF) were also detected. $Li_xPO_yF_z$ and Li_xPF_y are highly soluble in the DEC solvent used for the soft wash of these electrodes after the galvanostatic studies and are therefore likely to vary in concentration from sample to sample mostly due to variations in sample prep. LiF, however, is highly insoluble in DEC and is therefore more representative of the quantity actually contained in the SEI.[39–41]Interestingly, fluorinated alkane species (RCF_2 & RCF_3) were also detected. However, it was found in our groups' previous work on the anodic SEI that fluorinated alkane species are formed from deleterious reactions between carbonated species with HF (formed as a contaminant from exposure to moisture).[17] The RO_x interface reduced these contaminants during the transfer process, but it cannot reduce the inevitable water that is retained in the composite electrode. These electrodes are highly porous and even after placing under vacuum or heating can still retain moisture allowing for the deleterious reactions. These chemical functionalities identified on the surface of $Li_3V_2(PO_4)_3$ are all very similar to what is typically seen on the anodic SEI. Li_2O is also commonly found on reductively formed SEI layers. Determining Li_2O was challenging on the surface of $Li_3V_2(PO_4)_3$. Reported values for the

Li (55.6 eV) and O 1s (531.3 eV) signal directly interfere with the Li and O signal of TMP electrodes.

4.3.6 Spontaneous Reactions Between $Li_3V_2(PO_4)_3$ & Electrolyte

Since the chemical composition of the SEI at both potential windows is similar in chemical composition, we decided to study a possible spontaneous reaction between the electrode and electrolyte as has been reported for $Li_xM_yO_z$ electrodes. When comparing transition metal oxides and phosphates one must note that the oxygen basicity differs. Due to the covalent bonding between the phosphorous and oxygen atom in TMPs, the oxygen is less basic or reactive. Therefore, the nucleophilic mechanism previously described for the oxides should not hold for $Li_3V_2(PO_4)_3$ and an SEI film is not expected to be present before electrochemical cycling. Aging studies were conducted on the composite electrode for 60 days. These electrodes were immersed in the pure electrolyte without any electrochemical bias applied. After completion of the aging experiment, the samples were prepared similarly for XPS analysis. The XPS results for the C and F 1s energetic regions are shown in Figure 4.7(a) and (b). The O 1s, Li 1s, P 2p and V 2p energetic regions are shown Figure 4.5(a)-(d). From the spectra, it is obvious that similar chemistry is formed spontaneously on the surface of this composite electrode upon being immersed in the electrolyte. This led us to speculate the role that the other components (binder & carbon) in the composite electrode may have on the surface chemistry. The same aging studies were conducted separately on the components. PTFE is well-known to be an electronically insulating material and therefore should not be reactive during electrochemical studies. Moreover, it is highly resistant to strong acids and bases. The aging studies on PTFE showed no change in the surface properties. Only residual adventitious carbon could be found. Handling of pure $Li_3V_2(PO_4)_3$ and Super P® Li

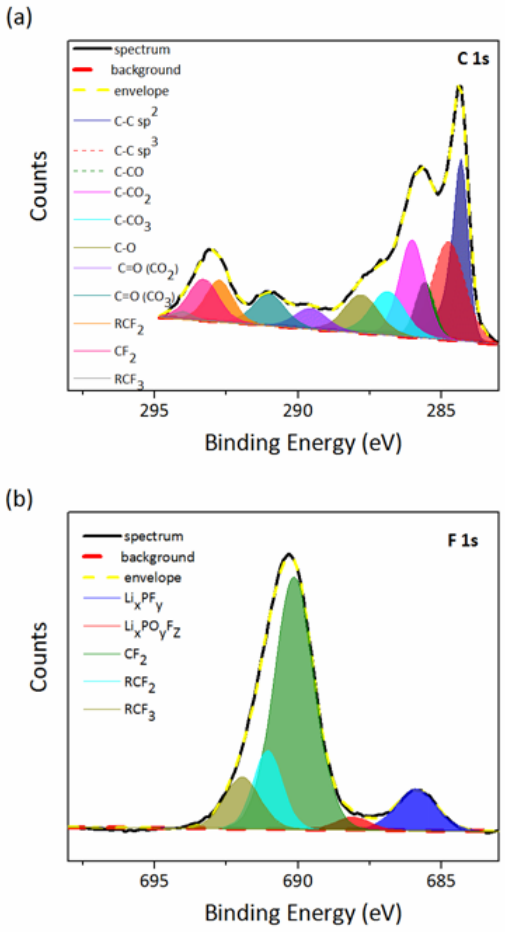

Figure 4.7 (a) C 1s and (b) F 1s XPS spectra of a composite $Li_3V_2(PO_4)_3$ electrode after being aged in 1 M $LiPF_6$ in 1:1 EC/DEC electrolyte for 60 days showing the spontaneous formation of the SEI.

carbon powders proved to be more challenging for XPS sample preparation and therefore had to be mixed with PTFE binder.

For the $Li_3V_2(PO_4)_3$/PTFE composite, no organic functional groups that correspond to electrolyte decomposition were detected after aging. The oxidized carbon functionalities found (C-O and C=O) are attributed to oxidized adventitious carbon that is originally present in the pure $Li_3V_2(PO_4)_3$ powder Figure 4.8(a)-(f)). Therefore, we did not see a catalytic effect from the vanadium metal in spontaneously decomposing the electrolyte as some have proposed. Figure 4.9 shows the C, O and F 1s spectra of the aged Super P® Li carbon /PTFE composite compared to the pristine Super P® Li carbon. We found all of the functional groups that were present on the composite electrode to also be contained on the Super P® Li carbon/PTFE material. This clearly shows that the electrolyte is inherently unstable on the carbon additive and that spontaneous decomposition of the electrolyte occurs on the additive carbon not the active material. The composite electrode is comprised of 85% active material, 12% Super P® Li carbon and 3% PTFE in bulk. However, comparing the surface atomic percentages of the composite electrode (Figure 4.10), we see that ~50% of the surface is composed of carbon (mostly from the Super P® Li additive). Super P® Li carbon is a high-surface area, nano-sized carbon black about 30 nm in size. In contrast, the active material is an aggregate of micron-sized particles. Therefore, most of the surface area of the composite electrode consists of the additive carbon and further reinforces the idea that the SEI on these composite electrodes is highly influenced by the conductive carbon. This changes the idea that the spontaneous formation of a passivation film on cathodes is induced by the oxygen in either the transition metal oxide or phosphate. From these results, we believe that part of the surface chemistry is from corrosion-like reactions, possibly from reaction of carbon with HF, a contaminant found in $LiPF_6$ based electrolytes. Corrosion

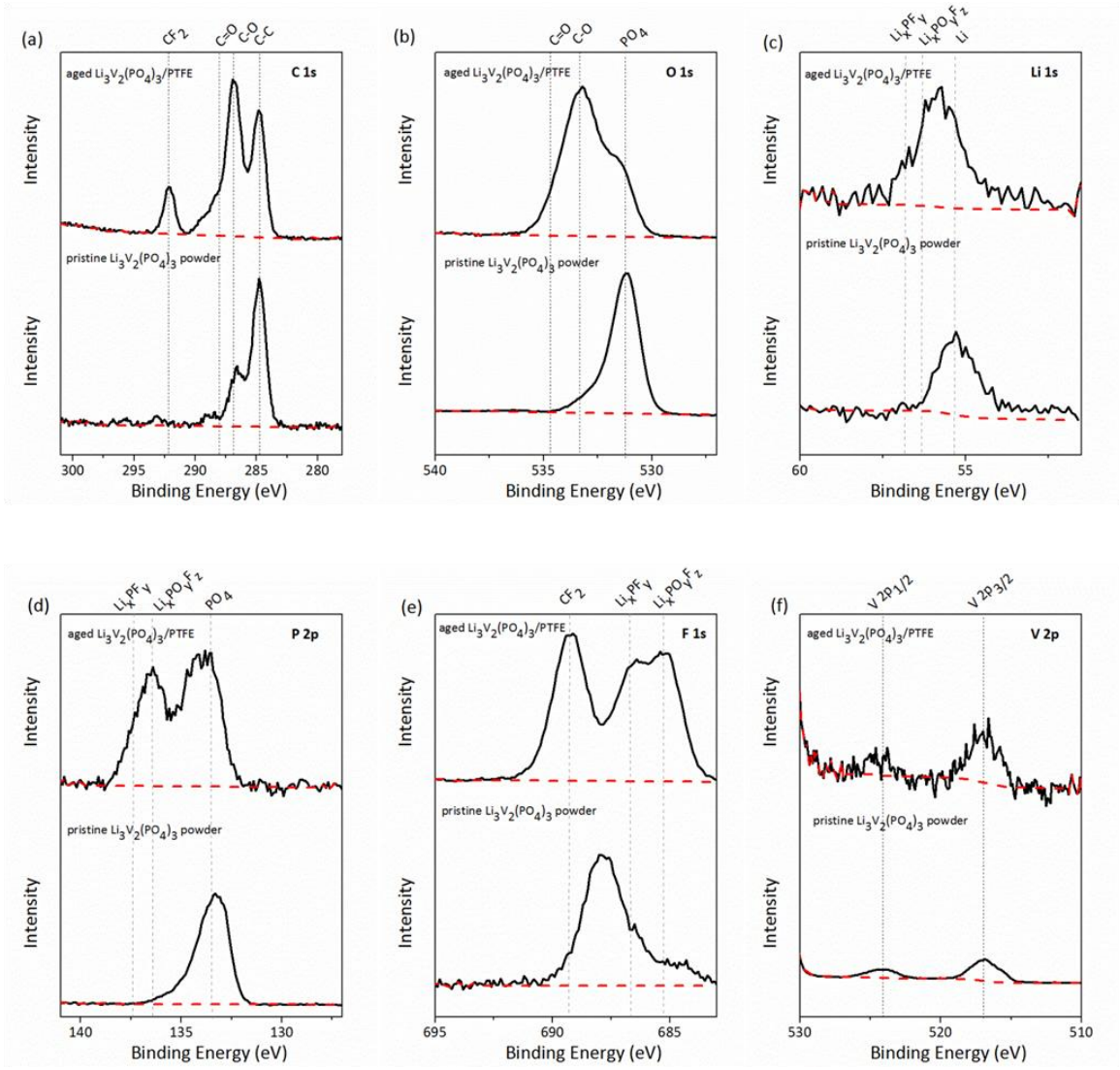

Figure 4.8 (a)-(f) (a) C 1s (b) O 1s (c) Li 1s (d) P 2p (e) F 1s and (f) V 2p XPS spectra of pristine $Li_3V_2(PO_4)_3$ compared to $Li_3V_2(PO_4)_3$/PTFE after being aged in 1 M $LiPF_6$ in 1:1 EC/DEC for 60 days.

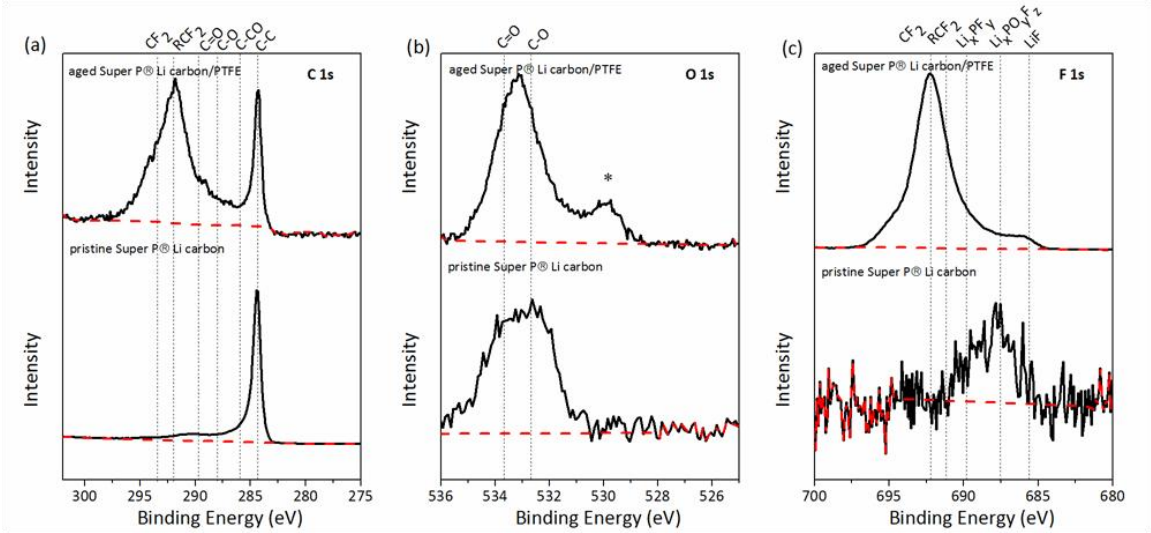

Figure 4.9 (a) C 1s (b) O 1s and (c) F 1s spectra of pristine Super P® Li carbon compared to Super P® Li carbon/PTFE after being aged in 1 M $LiPF_6$ in 1:1 EC/DEC electrolyte for 60 days showing the spontaneous formation of the SEI.

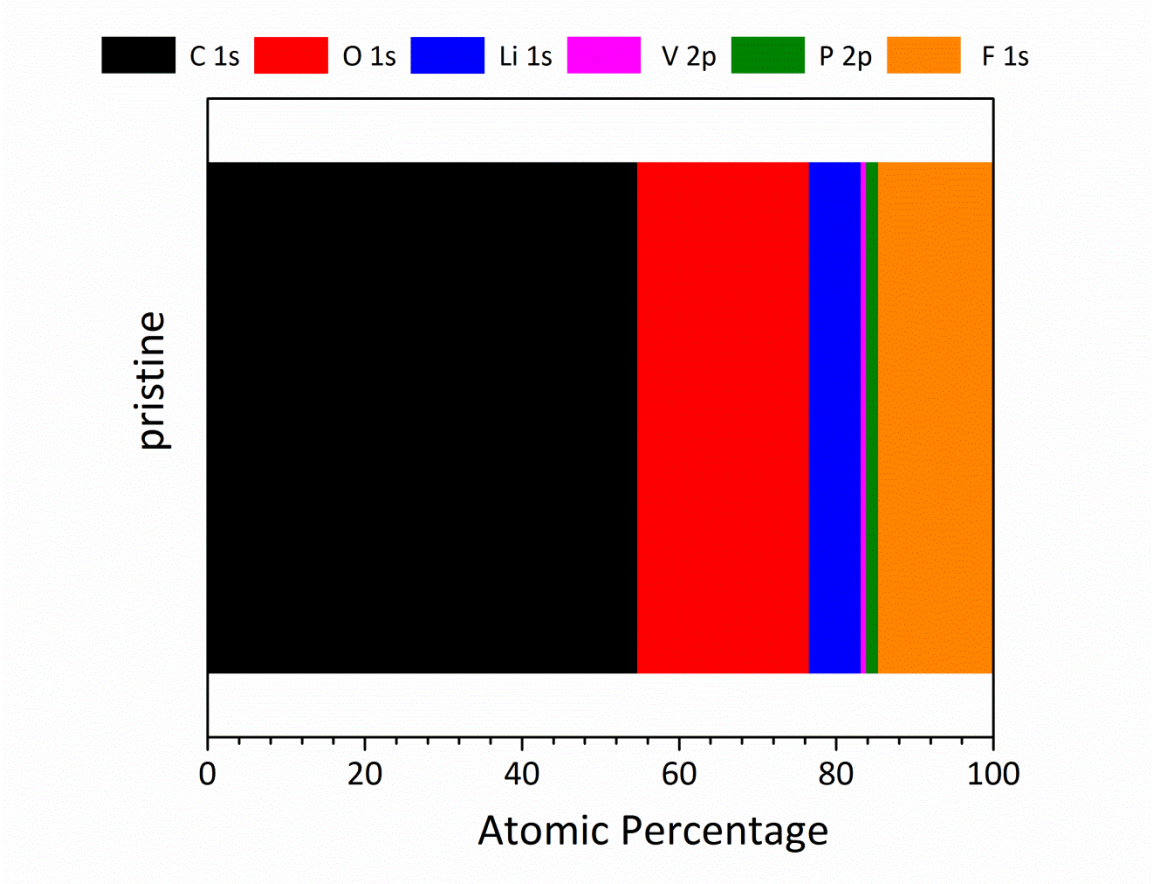

Figure 4.10 Percentages of the elements comprising the surface of pristine, composite $Li_3V_2(PO_4)_3$ electrode.

along with spontaneous polymerization reactions on the carbon surface lead to a complex surface chemistry before even performing electrochemical cycling studies.

We also tested the individual components by galvanostatically cycling them (1 cycle) to see whether oxidative decomposition would form an SEI layer on $Li_3V_2(PO_4)_3$/PTFE. Similarly to the aging studies, only oxidized adventitious carbon was found on $Li_3V_2(PO_4)_3$/PTFE, yet an SEI was found on Super P® Li /PTFE. We conclude from this work that the SEI is formed both spontaneously and electrochemically on Super P® Li carbon.

4.3.7 Limitations in Analyzing Composite Electrodes

Preparation of the $Li_3V_2(PO_4)_3$ composite electrode requires mixing dry powders thoroughly to make a micron thick electrode that is both porous and highly heterogeneous. From the SEM image of the pristine composite electrode (Figure 4.11(a)) it is evident that the surface consists of varying-size particles with differing morphologies that leads to a high-surface roughness. This roughness is unfavorable for XPS measurements. Non-uniform structures can lead to shadowing of either the X-ray source or the ejected core electrons.[42,43] This leads to a diminished intensity of the peaks analyzed thus not allowing accurate quantitative data collection of the surface chemistry. Spectra taken on three different areas on one of the samples shows that the SEI quantitatively changes from area to area (Figure 4.11(b) and (c)). Therefore, it is impossible to differentiate (quantitatively) the SEI on two or more composite electrodes with different electrochemical preparation of the SEI (either different electrochemical window applied or number of cycles). In Figures 4.4 & 4.6, what appears to be an evolving SEI is more than likely related to the shadowing effect leading to varied intensities because of the surface morphology. In order to circumvent this issue, model

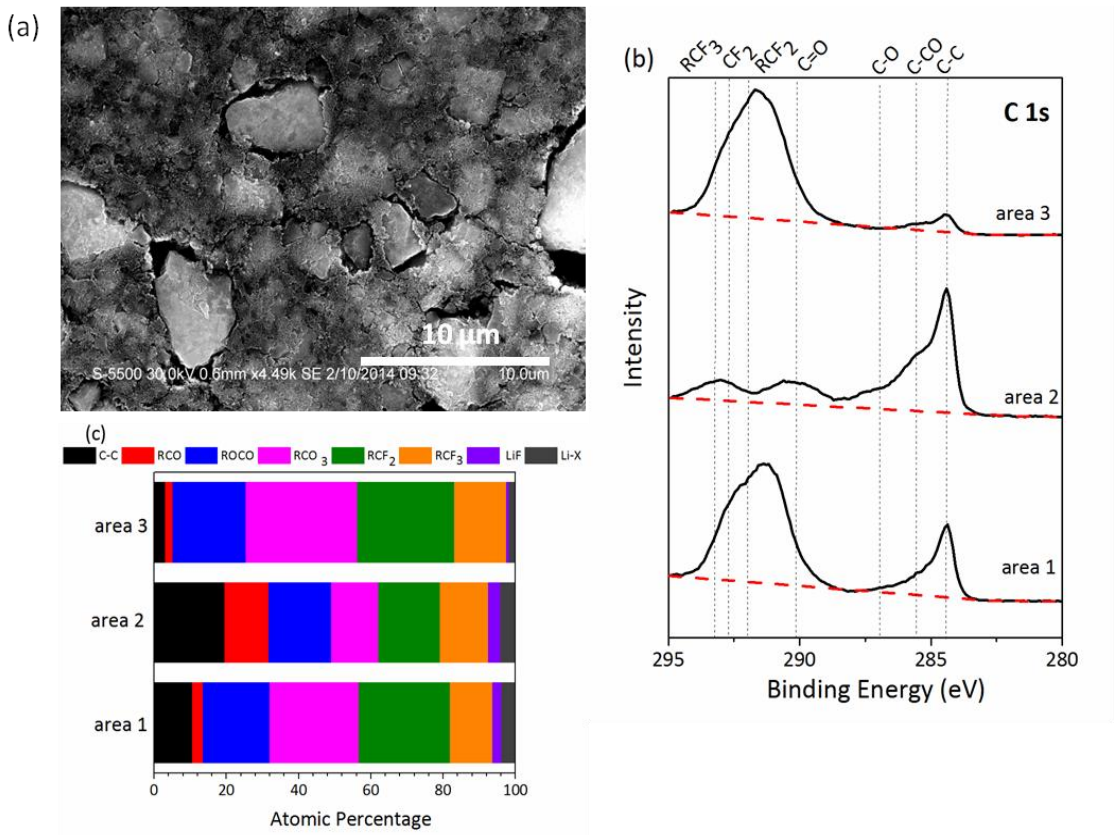

Figure 4.11 (a) SEM image of a pristine $Li_3V_2(PO_4)_3$ composite electrode. (b) C 1s spectra of three distinct areas (300 by 700 µm spot size) on a $Li_3V_2(PO_4)_3$ composite electrode after 5 cycles in the 3.0-4.8 V vs. Li/Li^+ window. (c) Percentages of the functionalities comprising the SEI on the three distinct areas. Functionalities include alkanes (C-C), alkoxides and ethers (RCO), lithium carboxylate and esters (ROCO), carbonates (RCO_3), difluoroalkanes (RCF_2), trifluoroalkanes (RCF_3), lithium fluoride (LiF) and degraded lithium salt products (Li-X, which possibly includes Li_xPF_y, and $Li_xPO_yF_z$).

like electrodes with a flat surface morphology must be used. Yet, to our knowledge there is only one such report that attempted to perform SEI studies on a flat cathode (spin coated $LiMn_2O_4$ on Pt substrates for in situ ellipsometry measurements).[44] In future studies we will attempt to study transition metal phosphates and oxides deposited on substrates through atomic layer deposition (ALD), which will not only provide a flat surface for high-resolution surface analytical measurements, but will also prevent spectral interference from the binder and carbon additive.

The heterogeneity of these composite electrodes also causes issues when interpreting the XPS results of the substrate. The individual $Li_3V_2(PO_4)_3$ particles are connected slightly differently to neighboring carbon and binder particles leading to differing electrical connectivity. This difference leads to some particles being more reactive than others towards lithium, resulting in differing states-of-charge as has been reported by several groups.[45,46] The shift in binding energy for the V 2p signal cannot be directly correlated to the electrochemical testing or formation of the SEI, but it may be inherently associated with the heterogeneous electrical connectivity in these electrodes.

4.4 CONCLUSIONS

In this work we investigated the surface chemistry of a composite $Li_3V_2(PO_4)_3$ electrode in a non-aqueous electrolyte after electrochemical cycling and aging. The galvanostatic cycling experiments were conducted in the stable 3.0-4.2 vs. Li/Li^+ window as well in the 3.0-4.8 vs. Li/Li^+ window. XPS studies of the cycled composite electrodes proved that an SEI film is formed on the surface at both potential windows. Quantitatively distinguishing the SEI of $Li_3V_2(PO_4)_3$ cycled in the two potential windows proved to be challenging due to the high-surface roughness and shadowing effect of these composite electrodes. A possible dissolution or instability of the SEI at high charging

potential (4.8 V vs. Li/Li^+) will be investigated in future work to help decipher the dissimilar performance of these electrodes in the two potential windows.

Moreover, a similar SEI forms on these composite electrodes if aged in the non-aqueous electrolyte without application of an electrochemical bias. We therefore report on a spontaneous SEI formed on a composite $Li_3V_2(PO_4)_3$ electrode. The chemical functional groups comprising the SEI is similar to those contained on the anode SEI. The organic species include ethers, alkoxides, esters, carboxylates and carbonates. Inorganic species found include LiF and degraded lithium salts ($Li_xPO_yF_z$ and Li_xPF_y).

Additional aging studies on the individual components of the composite electrode (active material, binder, carbon additive) revealed that the spontaneous SEI is predominantly formed on the carbon additive. This observation dismisses the mechanism previously proposed for ($Li_xM_yO_z$) cathodes where the basic oxygen performs a nucleophilic attack on the electrophilic carbon of the organic solvent contained in the electrolyte. We conclude that transition metal phosphates have less basic and therefore more stable oxygen that does not participate in these deleterious reactions with organic solvents. However, LIB cathodes traditionally contain micron-sized active material particles mixed with nano-conductive carbon, which has a higher surface-area-to-volume ratio. Therefore, most of the surface species of these composite electrodes, exposed to the electrolyte, is from the carbon additive. The carbon additive spontaneously reacts with the non-aqueous electrolyte to form an SEI similar in chemical composition to the SEI formed on the electrodes after electrochemical cycling. We believe the spontaneous reactions occur from corrosion-like reactions of the carbon material with HF as well as spontaneous polymerization of the solvent molecules.

These studies prove that the properties of the carbon additive are crucial in the formation of the SEI for cathode electrodes in LIBs. Moreover, the properties of the

carbon material must be well-understood and controlled in order to form a desired SEI on these electrodes. In future work, mechanistic studies for the SEI will be conducted on model electrodes for high-resolution surface spectroscopy studies.

4.5 REFERENCES

(1) Goodenough, J. B.; Kim, Y. *Chem. Mater.* **2009**, *22*, 587.

(2) Yuan, L.-X.; Wang, Z.-H.; Zhang, W.-X.; Hu, X.-L.; Chen, J.-T.; Huang, Y.-H.; Goodenough, J. B. *Energy Environ. Sci.* **2011**, *4*, 269.

(3) Sharabi, R.; Markevich, E.; Borgel, V.; Salitra, G.; Gershinsky, G.; Aurbach, D.; Semrau, G.; Schmidt, M. A.; Schall, N.; Stinner, C. *J. Power Sources* **2012**, *203*, 109.

(4) Pivko, M.; Bele, M.; Tchernychova, E.; Logar, N. Z.; Dominko, R.; Gaberscek, M. *Chem. Mater.* **2012**, *24*, 1041.

(5) Wolfenstine, J.; Allen, J. *J. Power Sources* **2005**, *142*, 389.

(6) Rui, X.; Yan, Q.; Skyllas-Kazacos, M.; Lim, T. M. *J. Power Sources* **2014**, *258*, 19.

(7) Yin, S.-C.; Grondey, H.; Strobel, P.; Anne, M.; Nazar, L. F. *J. Am. Chem. Soc.* **2003**, *125*, 10402.

(8) Huang, H.; Yin, S.-C.; Kerr, T.; Taylor, N.; Nazar, L. F. *Adv. Mater.* **2002**, *14*, 1525.

(9) Su, J.; Wu, X.-L.; Lee, J.-S.; Kim, J.; Guo, Y.-G. *J. Mater. Chem. A* **2013**, *1*, 2508.

(10) Patoux, S.; Wurm, C.; Morcrette, M.; Rousse, G.; Masquelier, C. *Sel. Pap. Present. 11th Int. Meet. Lithium Batter.* **2003**, *119–121*, 278.

(11) Jiang, T.; Wang, C.; Chen, G.; Chen, H.; Wei, Y.; Li, X. *Solid State Ion.* **2009**, *180*, 708.

(12) Xu, K. *Chem. Rev.* **2004**, *104*, 4303.

(13) Verma, P.; Maire, P.; Novák, P. *Electrochimica Acta* **2010**, *55*, 6332.

(14) Aurbach, D.; Zinigrad, E.; Cohen, Y.; Teller, H. *Proc. Symp. Mater. Adv. Batter. Fuel Cells Organised Conjunction Int. Conf. Mater. Adv. Technol. ICMAT 2001* **2002**, *148*, 405.

(15) Balbuena, Perla B.; Wang, Yixuan. *Lithium-Ion Batteries: Solid-Electrolyte Interphase*; Imperial College Press, 2004.

(16) Pérez-Villar, S.; Lanz, P.; Schneider, H.; Novák, P. *Electrochimica Acta* **2013**, *106*, 506.

(17) Schroder, K. W.; Celio, H.; Webb, L. J.; Stevenson, K. J. *J. Phys. Chem. C* **2012**, *116*, 19737.

(18) Xing, L.; Li, W.; Wang, C.; Gu, F.; Xu, M.; Tan, C.; Yi, J. *J. Phys. Chem. B* **2009**, *113*, 16596.

(19) Borodin, O.; Behl, W.; Jow, T. R. *J. Phys. Chem. C* **2013**, *117*, 8661.

(20) Edström, K.; Gustafsson, T.; Thomas, J. O. *Polym. Batter. Fuel CellsSelection Pap. First Int. Conf.* **2004**, *50*, 397.

(21) Ostrovskii, D.; Ronci, F.; Scrosati, B.; Jacobsson, P. *J. Power Sources* **2001**, *103*, 10.

(22) Malmgren, S.; Rensmo, H.; Gustafsson, T.; Gorgoi, M.; Edström, K. *ECS Trans.* **2010**, *25*, 201.

(23) Castro, L.; Dedryvère, R.; Ledeuil, J.-B.; Bréger, J.; Tessier, C.; Gonbeau, D. *J. Electrochem. Soc.* **2012**, *159*, A357.

(24) Membreño, N.; Xiao, P.; Park, K.-S.; Goodenough, J. B.; Henkelman, G.; Stevenson, K. J. *J. Phys. Chem. C* **2013**, *117*, 11994.

(25) Yin, S.-C.; Grondey, H.; Strobel, P.; Huang, H.; Nazar, L. F. *J. Am. Chem. Soc.* **2002**, *125*, 326.

(26) Dedryvère, R.; Maccario, M.; Croguennec, L.; Le Cras, F.; Delmas, C.; Gonbeau, D. *Chem. Mater.* **2008**, *20*, 7164.

(27) Strzemiecka, B.; Voelkel, A.; Donate-Robles, J.; Martín-Martínez, J. M. *Appl. Surf. Sci.* **2014**, *316*, 315.

(28) Beamson, G.; Briggs, D. *High Resolution of organic polymers: The Scienta ESCA 300 database*; John Wiley & Sons: Chichester, U.K., 1992; Vol. 15.

(29) Chen, Y.; Zhang, D.; Bian, X.; Bie, X.; Wang, C.; Du, F.; Jang, M.; Chen, G.; Wei, Y. *Electrochimica Acta* **2012**, *79*, 95.

(30) Aurbach, D.; Markovsky, B.; Shechter, A.; Ein-Eli, Y.; Cohen, H. *J. Electrochem. Soc.* **1996**, *143*, 3809.

(31) Andersson, A. .; Henningson, A.; Siegbahn, H.; Jansson, U.; Edström, K. *Sel. Pap. Present. 11th Int. Meet. Lithium Batter.* **2003**, *119–121*, 522.

(32) Eshkenazi, V.; Peled, E.; Burstein, L.; Golodnitsky, D. *Solid State Ion.* **2004**, *170*, 83.

(33) Peled, E.; Bar Tow, D.; Merson, A.; Gladkich, A.; Burstein, L.; Golodnitsky, D. *Proc. 10th Int. Meet. Lithium Batter.* **2001**, *97–98*, 52.

(34) Moshkovich, M.; Cojocaru, M.; Gottlieb, H. .; Aurbach, D. *J. Electroanal. Chem.* **2001**, *497*, 84.

(35) Aurbach, D.; Markovsky, B.; Levi, M. .; Levi, E.; Schechter, A.; Moshkovich, M.; Cohen, Y. *J. Power Sources* **1999**, *81–82*, 95.

(36) Aurbach, D. *J. Power Sources* **2000**, *89*, 206.

(37) Zhang, S. S.; Xu, K.; Jow, T. R. *Electrochem. Solid-State Lett.* **2002**, *5*, A92.

(38) Chang, L.-S.; Lin, Y.-C.; Su, C.-Y.; Wu, H.-C.; Pan, J.-P. *Appl. Surf. Sci.* **2011**, *258*, 1279.

(39) Tasaki, K.; Harris, S. J. *J. Phys. Chem. C* **2010**, *114*, 8076.

(40) Tasaki, K.; Goldberg, A.; Lian, J.-J.; Walker, M.; Timmons, A.; Harris, S. J. *J. Electrochem. Soc.* **2009**, *156*, A1019.

(41) Jones, J.; Anouti, M.; Caillon-Caravanier, M.; Willmann, P.; Sizaret, P.-Y.; Lemordant, D. *Fluid Phase Equilibria* **2011**, *305*, 121.

(42) Chatelier, R. C.; St John, H. A. W.; Gengenbach, T. R.; Kingshott, P.; Griesser, H. J. *Surf. Interface Anal.* **1997**, *25*, 741.

(43) Artyushkova, K.; Fulghum, J. E. *Surf. Interface Anal.* **2004**, *36*, 1304.

(44) Lei, J.; Li, L.; Kostecki, R.; Muller, R.; McLarnon, F. *J. Electrochem. Soc.* **2005**, *152*, A774.

(45) Chueh, W. C.; El Gabaly, F.; Sugar, J. D.; Bartelt, N. C.; McDaniel, A. H.; Fenton, K. R.; Zavadil, K. R.; Tyliszczak, T.; Lai, W.; McCarty, K. F. *Nano Lett.* **2013**, *13*, 866.

(46) Nanda, J.; Remillard, J.; O'Neill, A.; Bernardi, D.; Ro, T.; Nietering, K. E.; Go, J.-Y.; Miller, T. J. *Adv. Funct. Mater.* **2011**, *21*, 3282.

CHAPTER 5[4]

Future Direction: Novel *In Situ* Raman Microscopy Test Cell for Lithium Ion Batteries

5.1 INTRODUCTION

Raman spectroscopy is a vibrational technique that provides structural information on inorganic and organic compounds at the level of atomic bonds.[1] By coupling a microscope to the Raman spectrometer the spatial resolution can be minimized to less than a micron (dependent on the wavelength of the radiation source and numerical aperture of the objective). This has allowed the Raman spectroscopic technique to become more applicable to the characterization of various materials that includes polymers, ceramics, inorganic solids, semiconductor and battery materials.[2]

The high sensitivity of Raman microscopy allows for the detection of changes in bond lengths, bond angles, coordination, lithium dynamics, local disorder and cation ordering which makes it a great probe for electrode materials in lithium ion batteries (LIBs).[2] Moreover, it is a nondestructive technique, does not require sample preparation and because it is insensitive to strong infrared (IR) absorbers such as glass, measurements can be acquired through optically transparent materials permitting *in situ* investigations. This is an important aspect to studying lithium battery materials since bulk and surface chemistry can be highly reactive with the atmosphere. The ability to focus on small areas when using Raman microscopy makes it advantageous in studying lithium battery electrodes since they are often composites that not only contain active material but also binder and a conductive additive. The small focusing area thus allows for each component to be probed individually. This also permits 2-D and 3-D mapping.[2]

[4] I would like to acknowledge Alexa Marsh and Souvik Banerjee for their assistance with the *in situ* Raman microscopy measurements.

When comparing *in situ* and *ex situ* Raman microscopy there are different advantages and disadvantages for the two. Both can prevent atmospheric contamination and to different levels provide mechanistic information on the lithiation chemistry of LIBs. However, a greater signal to noise (S/N) is achieved with *ex situ* Raman microscopy because the electrolyte and soluble products formed on the surface can be removed prior to analysis.[3,4] However, treating the sample prior to analysis can make it more susceptible to unwanted chemical change at the surface and/or bulk through contamination. In addition, some of the products formed through lithiation reactions are kinetically unstable (i.e. conversion reaction products) making it challenging to accurately determine the correct phase. Therefore, *in situ* Raman microscopy provides the best mechanism by which to accurately study lithiation dynamics.

A few home-built, *in situ* Raman microscopy test cells have been reported. Two basic models have been devised. The first type is based on traditional electrochemical test cell designs such as a coin cell[5–8] or Swagelok cell.[9] The only modification of the test cell is that an optical window is inserted. The second type uses a polymer test cell with a built in optical window. The LIB components are stacked in a sandwich arrangement (lithium, separator, working electrode).[4,10,11]In these stacked arrangements some pressure mechanism (such as a spring) is implemented to obtain good electrical contact between the cathode and anode. In both types of *in situ* cells the large pressures used require a thick optical window that will not break under such constraints. This increases the path length of the scattered photon as well as the background from the glass, greatly diminishing the S/N. Moreover, these designs provide a fixed distance between the optical window and electrode. Fixing this distance limits the range of microscope objectives that can be used (different working distances) during analysis. It also limits the types of LIB electrodes analyzed. For example, wafers and electrodeposited materials are

much thicker (millimeters) than traditional powder composite electrodes (microns). These thicker electrodes would not fit in these design types due to size constraints.

Of the *in situ* Raman microscopy reports very few provide technical details on the *in situ* cell itself. The features and necessary design components for optimal Raman scattering and electrochemical measurements are also not reported. In this report we t provide details on the features and components that are essential for simultaneous electrochemical and Raman microscopy measurements. Some of the challenges with the current design are also addressed as well as future directions to optimize *in situ* Raman microscopy measurements.

5.2 EXPERIMENTAL SECTION

5.2.1 Materials for the test cell

The test cell is based on poly(chlorotrifluoro ethylene) (PCTFE). In comparison to the traditionally used poly(tetrafluoro ethylene) (PTFE), PCTFE has a significantly lower permeability coefficient for oxygen and moisture.[12] This facilitates slow rate electrochemical investigations without significant contamination from the atmosphere.

Double seal, Viton® or Teflon® o-rings were used to seal components of the cell base from the atmosphere. For the optical window, an o-ring with a lower durometer measurement of 55 D was used to facilitate the application of pressure on the fragile, optical window. These fluoroelastomer o-rings are compatible with $LiPF_6$ based electrolytes for LIBs which commonly contain hydrofluoric acid as a contaminant.

All metallic components of the test cell, which includes the rods, screws, helicoils and shaft were made of 304 stainless steel (the material commonly used for coin cells).

The optical window is a circular glass cover slide, 0.17 mm in thickness and modified to 10 mm diameter. Sapphire and quartz can also be used as optical windows for LIB *in situ* Raman microscopy test cells.

5.2.2 Full cell construction

The test cell is a modular design composed of three main pieces: top piece, lid and base (Figure 5.1). Figure 5.2(a) shows the top piece (0.76" diameter, 0.11" thickness) which houses the glass optical window that is sealed from the atmosphere by a Teflon® o-ring (1 mm width, 8 mm I.D.). The top piece is then assembled onto the lid of the test cell with 6, 2-56 x 1/4" screws.

The lid (2.26" diameter, .33" thickness) (Figure 5.2(b)) contains two stainless rods that serve as connections for the pseudo reference and counter lithium electrodes. A double seal Viton® o-ring (1/16" width, 1 3/8" I.D.) is placed between the lid and base and sealed from the atmosphere by closing it with 3, 8-32 x 3/4" screws.

The working electrode is mounted on a stainless steel threaded shaft (0.37" diameter, 2.64" long) (5.2 (c) and(d)) centered in the base (2.26" diameter, 1.26" thickness) of the cell (Figure 5.2(e) and (f)). Good electrical contact is maintained by adhering the electrode to the shaft with a circular stainless steel frame using 4, 0-80 x 5/32" screws (Figure 5.2(c)). The inner circle of the frame has a diameter of 4 mm which leaves 12.6 mm^2 active area exposed to the electrolyte. The threaded shaft allows the position of the electrode to be changed in the vertical direction of the base during *in situ* Raman microscopy experiments. This is essential for electrode materials that experience a significant change in volume during lithiation (conversion and alloying materials) and may need to be refocused during the experiment. Additionally, as opposed to conventional *in situ* cells that offer a fixed distance between the current collector and the

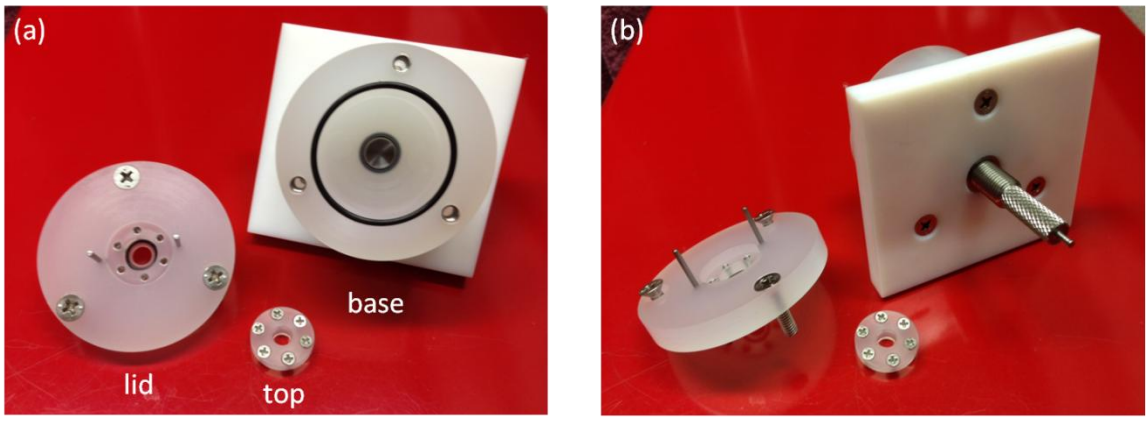

Figure 5.1 Front (a) and back view (b) of the three main components (top piece, lid and base) of the *in situ* Raman microscopy test cell.

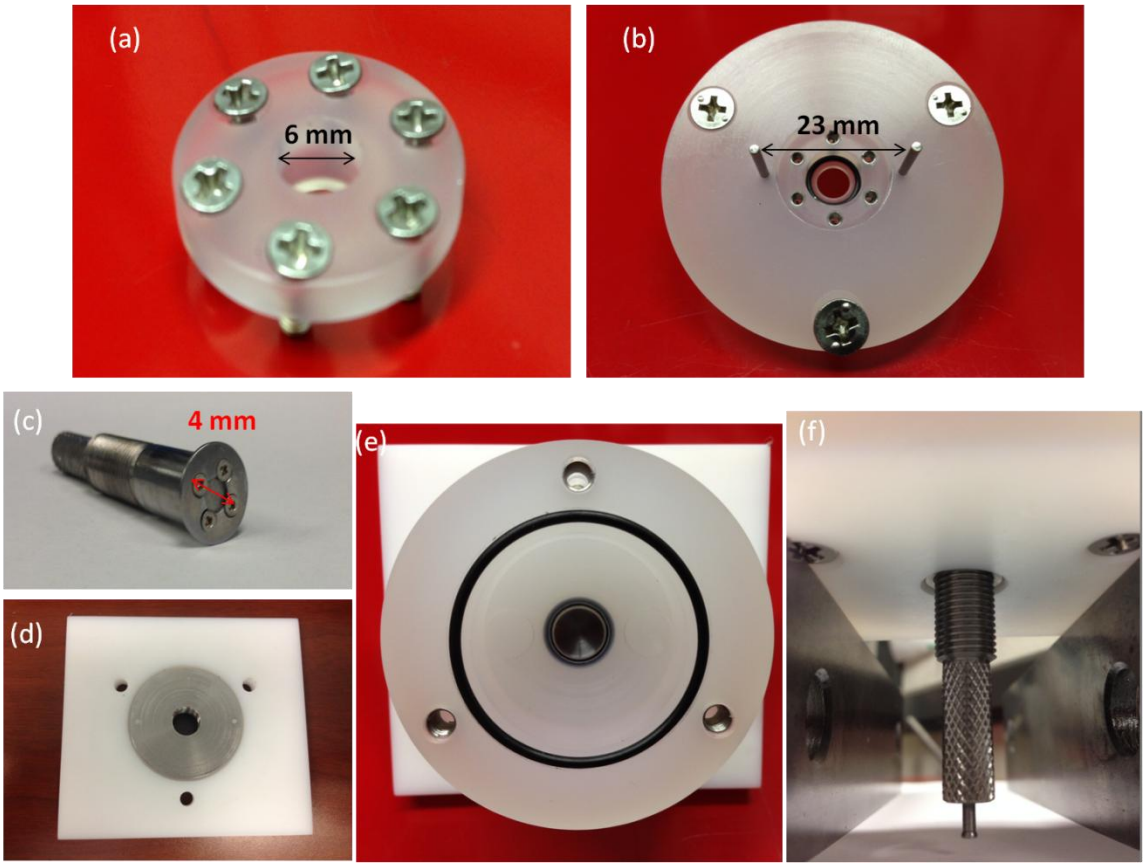

Figure 5.2 Images of the individual (a) top piece, (b) lid, (c) shaft (with frame), (d) and threading apparatus for the shaft of the *in situ* Raman microscopy test cell. Top (e) and bottom view (f) of the shaft assembled in the base of the *in situ* Raman microscopy test cell.

the optical window, this movable shaft can be adjusted to fit electrodes of various thicknesses. Figure 5.3 shows an image of the fully assembled cell.

5.2.3 Titanium Metallocene O_2 indicator

Titanium (III) metallocene compounds provide a useful aid for determining the relative concentration of O_2. $[TiCp_2N(CCH_3)_2]^+$ (where Cp is cyclopentadienyl, C_5H_5) was synthesized following a procedure by Nieter Burgmayer.[13] The original deep blue solution changes to a yellow color upon exposure to molecular oxygen indicating a change in oxidation state from Ti^{3+} to Ti^{4+}.[13] When the solution is exposed to trace levels of molecular oxygen the color changes gradually from a dark blue to an olive green. At high concentrations of O_2 it will turn to yellow. If the solution remains dark blue the O_2 concentration can be estimated to be well below 5 ppm. If the solution turns into an olive green color the solution is less than 5 ppm. Once yellow, the O_2 concentrations is considered to be well above 5 ppm.

5.2.4 Electrode Materials

The $LiFePO_4$ electrode was a composite of 85% carbon coated $LiFePO_4$ (Hydro-Québec, 200-300 nm), 3 wt.% carbon black, 3 wt.% carbon fiber (VGCF®) and 5 wt.% polyvinylidene fluoride (PVDF) binder. To fabricate the electrodes PVDF pellets were dissolved in N-Methyl-2-pyrrolidone (NMP) solvent to make a 10 mg/mL solution. The $LiFePO_4$ and carbon powders were then dissolved in the PVDF in NMP solution and stirred for 12 h to make an ink like slurry. The slurry was then deposited on Al foil (current collector) at 40 °C and heated in a vacuum oven at 80 °C for 12 h. From the electrode sheet circular pellets of about ~4 mg were punched.

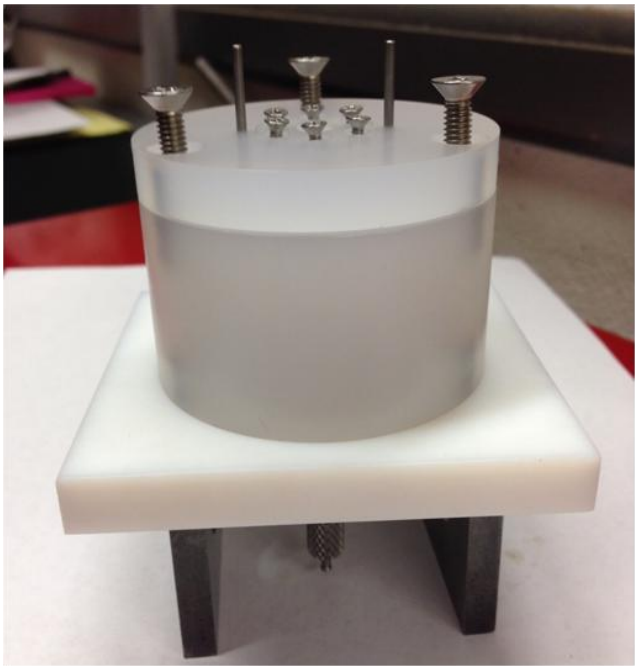

Figure 5.3 Image of the assembled *in situ* Raman microscopy test cell.

Similarly a composite of 90% carbon black (Super P® Li) and 10% PVDF was fabricated to test the electrochemical activity of carbon black at high operating potentials.

Electrodeposited TiO_2 was prepared by a recipe previously developed by Cambridge NanoTech. Tetrakis dimethylamido titanium (TDMAT) (200 °C) was used as the Ti-containing precursor. Room temperature water vapor (H_2O) was used as the O-containing precursor. N_2 was used as the both the purge and carrier gas. Each Atomic Layer Deposition (ALD) cycle consisted of a 0.1 s TDMAT pulse and a 0.015 s H_2O pulse, with 5 s N_2 purges between each pulse. 24 nm thick films were achieved with 500 cycles. After ALD, the layered electrodes were annealed in air at 400 °C for 1 hour, with a 5 °C/min thermal ramp rate. The substrate for these TiO_2 films were opaque pyrolyzed photoresist films (PPFs) deposited onto 1 in sq x 1 mm thick quartz slides. The preparation of these opaque PPF films can be found elsewhere.[14]

All electrode materials were tested in half-cell configurations. $LiFePO_4$, Super P® Li and TiO_2 individually served as the working electrodes. Two pieces of lithium foil were used as the pseudo counter and reference electrodes. The electrolyte was a 1 M solution of $LiPF_6$ in 1:1 ethylene carbonate (EC) in diethyl carbonate (DEC). Cyclic voltammograms (CVs) of the electrode materials were obtained on a CH 440 potentiostat.

5.2.5 Raman Microscopy Measurements

Raman spectra were acquired with a Renishaw inVia microscope system having a 514.5 nm Ar^+ laser in the backscattering configuration. For *ex situ* analysis, the beam was focused with a 50x objective lens resulting in approximately a 1.3 μm spot diameter under air. For *in situ* analysis the beam was focused with a long working distance (L) 15x objective lens.

5.3 RESULTS AND DISCUSSION

5.3.1 Oxygen test

To test the hermetic seal of the *in situ* Raman microscopy test cell a colorimetric titanium (III) metallocene compound was used. The titanium (III) metallocene indicator dried to a dark, olive-green color after remaining in the test cell for 48 hrs (Figure 5.4). This indicates that the O_2 level remained lower than 5 ppm during that period. This permits for slow rate, *in situ* experiments.

5.3.2 Electrochemical Performance

The first CV of the commercial $LiFePO_4$ composite at a scan rate of 0.05 mV/s electrode (Figure 5.5(a)) shows an anodic peak at 3.57 V vs. Li/Li^+ corresponding to the intercalation (charging) of lithium. The cathodic peak is centered at 3.28 V vs. Li/Li^+ corresponding to the reverse process, deintercalation of lithium (discharging). This agrees well with previous reports on $LiFePO_4$ that have shown the charge and discharge peaks to be centered at around 3.45 V vs. Li/Li^+.[15] The third through fifth cycles at the faster scan rate of 0.5 mV/s shows that the lithiation/delitaition of $LiFePO_4$ remains reversible (Figure 5.5(a)).

Raman microscopy measurements of the pristine $LiFePO_4$ composite electrode are shown in Figure 5.5(a). In the 100-1200 cm^{-1} wavenumber region it can be seen that only one vibrational mode at 949 cm^{-1} is identified.[6] This mode corresponds to the internal, symmetric stretch of the PO_4 group and is the peak of highest intensity in the spectrum of $LiFePO_4$. No other vibrational modes for $LiFePO_4$ can be detected. At high wavenumbers (Figure 5.6(b)) the D (1349 cm^{-1}) and G (1601 cm^{-1}) bands for graphitic carbon are detected.[10] These high intensity D and G-bands prevent detection of the modes for the inorganic $LiFePO_4$ crystals.[6]

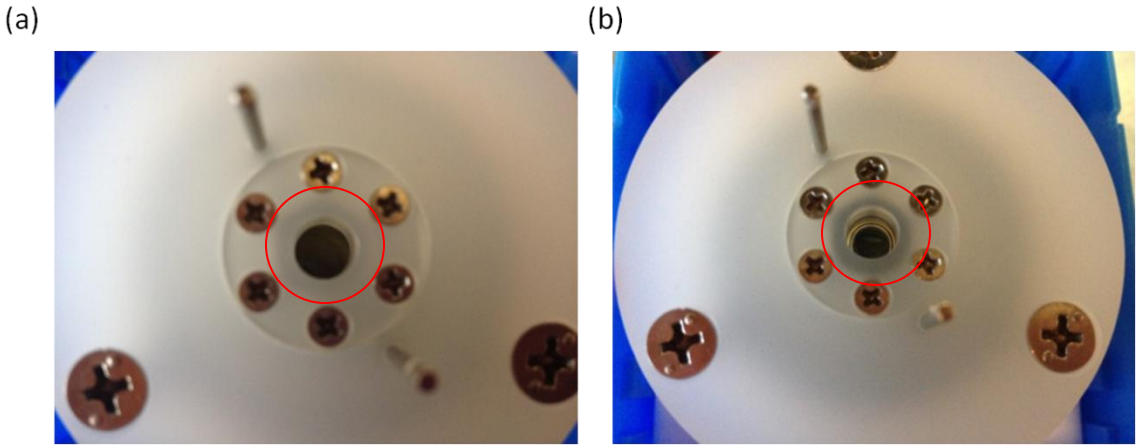

Figure 5.4 Top view images of the *in situ* Raman microscopy test cell right after assembly (a) and after 48 hours showing that the O_2 concentration in the cell roughly remained at less than 5 ppm as indicated by the olive-green color of the titanium (III) metallocene. The titanium (III) metallocene can be seen through the optical window circled in red.

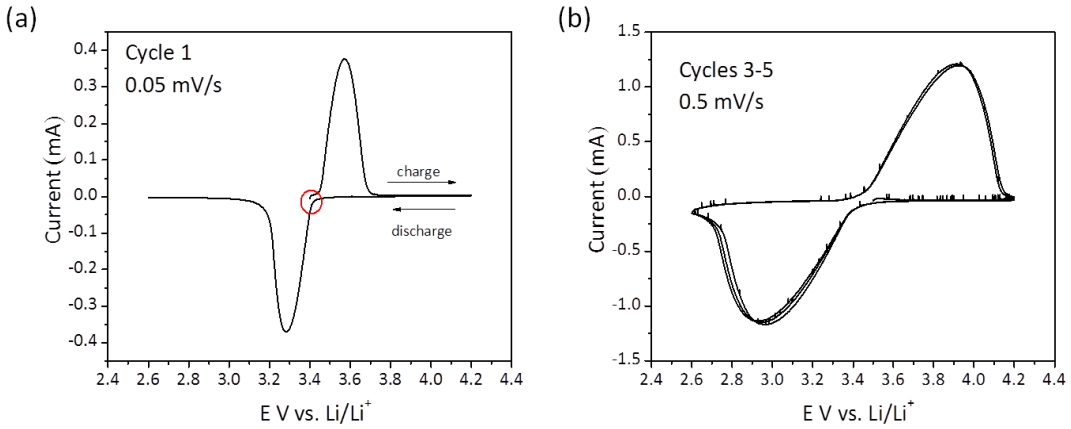

Figure 5.5 CVs of a composite $LiFePO_4$ electrode at a scan rate of 0.05 mV/s (a) and 0.5 mV/s (b). The first cycle shows an anodic peak at 3.57 V vs. Li/Li^+ (intercalation) and a cathodic peak at 3.28 V vs. Li/Li^+. The redox reactions are reversible over multiple CV cycles (3^{rd}-5^{th} cycles).

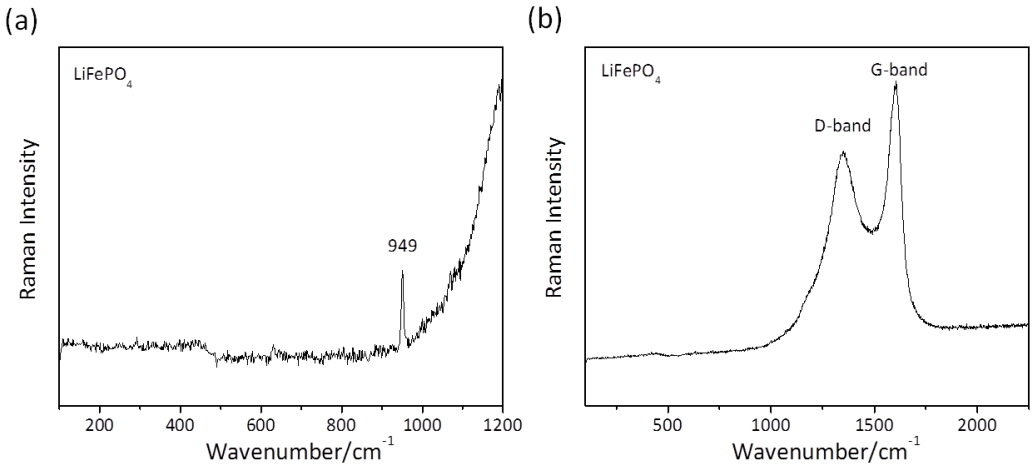

Figure 5.6 Raman microscopy of the composite $LiFePO_4$ electrode in the (a) 100-1200 cm^{-1} wavenumber region where the 949 cm^{-1} internal mode is detected and no other modes can be identified. (b) A scan in the 100-2250 cm^{-1} wavenumber region shows the high intensity D and G-bands corresponding to the graphitic carbon. Both spectra were acquired with a 50x objective at a power of 0.855 mW and a total acquisition time of 120 s at room temperature.

5.3.3 *In situ* Raman microscopy of a carbon black material at high operating potentials

Recently Kostecki and co-workers investigated the electrochemical properties of carbon black additives at high potentials in $LiPF_6$ based electrolytes.[10] CV, Raman microscopy, X-ray diffraction (XRD) and Scanning Electron Microscopy (SEM) experiments showed that these carbon black materials (normally used in cathode electrode formulations) intercalate PF_6^- at potentials above 4.0 V vs. Li/Li^+. After complete intercalation/deintercalation of PF_6^-, exfoliation of the graphitic domains in the carbon black was noted. This resulted in particle swelling and decohesion (SEM), loss of carbon from the electrode (SEM) and loss of crystallinity (XRD, Raman). Moreover, after multiple CV cycles the current response becomes purely capacitive.[10] *In situ* Raman microscopy measurements were performed on carbon black in a potential window of 2.6-4.9 V vs. Li/Li^+. The D and G-bands were monitored to note structural changes. At 4.2 V vs. Li/Li^+ the band intensity begins to diminish and at 4.8 V vs. Li/Li^+ the bands almost completely disappear. At both potentials broadening is also seen. On the reverse scan, at potentials below 3.5 V vs. Li/Li^+ the D and G-bands were partially restored showing that the intercalation process is not completely reversible.[10] A similar *in situ* Raman microscopy experiment was reproduced in this novel test cell as proof of concept. Super P® Li was tested as the carbon black material (Figure 5.7). The pristine spectrum of Super P® Li shows similar D and G-bands positioned at 1348 and 1580 cm^{-1} respectively (Figure 5.7(a)). The CV of Super P® Li in the potential window of 2.6-4.9 V vs. Li/Li^+ shows a similar current response to that reported by Kostecki and co-workers. Anodic current begins at about 3.5 V vs. Li/Li^+. Additional anodic peaks are seen at 3.8, 4.2 and 4.5 V vs. Li/Li^+ followed by a sharp rise in current at 4.8 V vs. Li/Li^+. The anodic current continued on the reverse scan until about 4.2 V vs. Li/Li^+. A single cathodic peak was

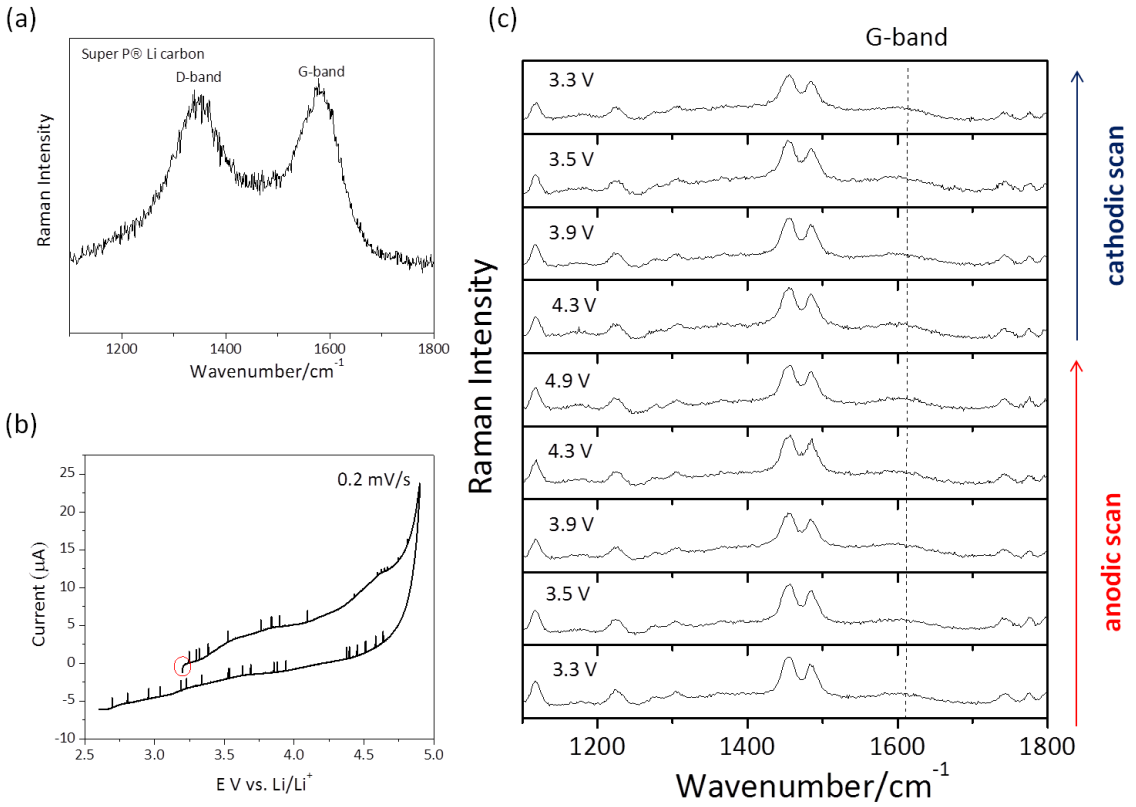

Figure 5.7 (a) Raman microscopy of pristine Super P® Li carbon black. This spectrum was acquired with a 50x objective at a power of 0.855 mW and a total acquisition time of 60 s at room temperature. (b) CV of Super P® Li in 1M $LiPF_6$ in 1:1 EC/DEC from 2.6 to 4.9 V vs. Li/Li^+ at a scan rate of 0.2 mV/s. (c) *In situ* Raman microscopy of Super P® Li in the 1100-1800 cm^{-1} wavenumber region.

detected at 3.8 V vs. Li/Li^+. However, from the *in situ* Raman microscopy data (Figure 5.7(c)) it is difficult to see any spectral changes in the D and G-bands as noted by Kostecki and co-workers. The spectra are difficult to interpret because the Raman and fluorescence signal from the electrolyte (Figure 5.8) drown out signal from the Super P® Li electrode. A comparison of the pristine super P® Li, of super P® Li at 3.3 V vs. Li/Li^+ in the *in situ* Raman microscopy test cell and of the pure electrolyte shows that the D-band cannot be detected (Figure 5.9). Furthermore, it is unclear whether the Raman mode around 1590 cm^{-1} in the *in situ* spectrum corresponds to the electrolyte or the G-band of the super P® Li carbon black. Identifying Raman modes of any LIB electrode at high wavenumbers where the fluorescence intensity is highest is challenging and can lead to inconclusive results.

5.3.4 ALD deposited TiO_2 as a model electrode

As was noted with the composite $LiFePO_4$ electrodes, obtaining signal from the active material is challenging because of the overpowering signal from the carbon additive. ALD LIB materials offer a simpler, cleaner spectrum of the active material that can facilitate *in situ* spectroscopic measurements.[14] In Figure 5.10(a) the Raman spectrum of pristine TiO_2 (500 cycles, ~25 nm) deposited by ALD is shown. Raman modes were detected at 144, 398, 518 and 636 cm^{-1} indicating formation of the anatase phase.[16] CVs of the ALD TiO_2 sample show two cathodic peaks at 1.9 and 1.3 V vs. Li/Li^+ (Figure 5.10(b)). Based on previous reports these peaks correspond well with the lithiation of nanosized anatase. A Li-poor phase ($Li_{0.05}TiO_2$) that retains the anatase original space group ($I4_1/amd$) is first formed. A Li-rich phase ($Li_{0.5}TiO_2$) with a new space group (*Imma*) is then formed. Nanosized TiO_2 forms the fully lithiated phase ($LiTiO_2$).[17] For the delithiation reaction a single anodic peak is p at 2.5 V vs. Li/Li^+.

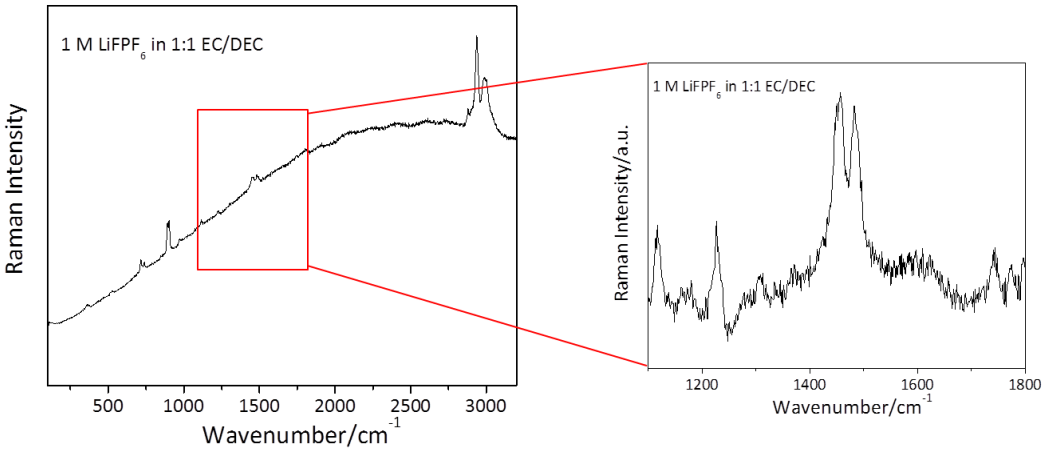

Figure 5.8 Raman microscopy spectra of 1 M $LiPF_6$ in 1:1 EC/DEC in the 100-3200 cm^{-1} wavenumber region showing the various Raman modes of the electrolyte as well as the high intensity fluorescence background. A spectrum in the wavenumber region of interest (1100-1800 cm^{-1}) for analysis of Super P® Li is also shown.

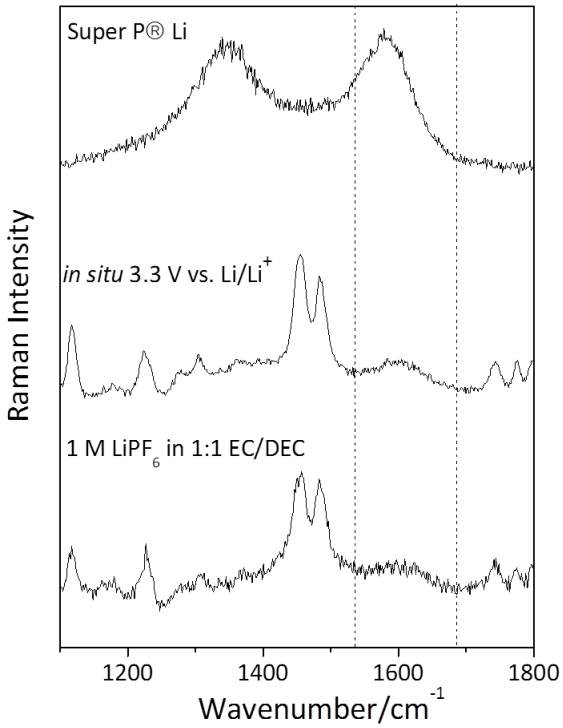

Figure 5.9 Comparison of the Raman microscopy spectra of pristine super P® Li, of super P® Li at 3.3 V vs. Li/Li^+ in the *in situ* Raman microscopy test cell and of the pure 1M $LiPF_6$ in 1:1 EC/DEC electrolyte.

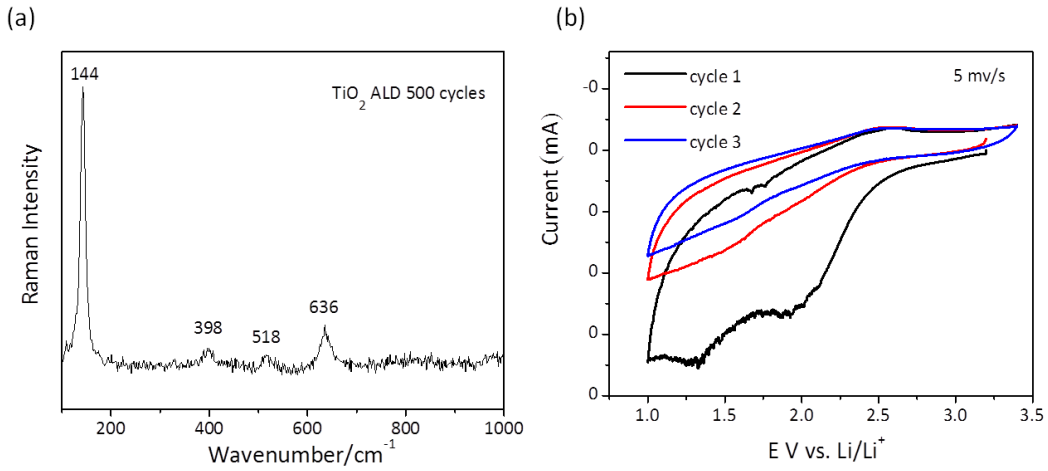

Figure 5.10 (a) Raman microscopy spectrum of ALD deposited TiO_2 (500 cycles, ~25 nm) on an OPPF substrate. (b) 1st-3rd CV cycles of ALD deposited TiO_2 at a scan rate of 5 mV/s in 1M $LiPF_6$ in 1:1 EC/DEC electrolyte.

The lithiation/delithiation of ALD deposited TiO_2 is not repeatable for the second and third CV cycles. This could be due to a connection problem between TiO_2 and the shaft, which was not an issue for the more conductive $LiFePO_4$ composite electrode.

5.4 CONCLUSIONS

A novel *in situ* Raman microscopy test cell was designed. The necessary criteria and components for optimal spectroelectrochemical measurements are addressed. The test cell is a modular design that can easily be assembled (mostly outside of the glovebox) and offers the ability to interchange the optical window. All test cell materials are chemically compatible with LIB chemistry. The design offers a hermetic seal with a concentration of 5 ppm or lower of O_2 for up to 48 hrs. Moreover, the movable shaft permits refocusing of LIB materials during operation which is beneficial when there is a large change in volume.

In future work, some of the challenges related to the intense fluorescence background will be circumvented by implementing nitrate and perchlorate based electrolytes. Some modifications will also be made to the current design in order to increase the S/N of the active material, such as decreasing the path length of the cell (distance between the working electrode to the microscope objective). This will increase the counts of Raman scattered photons detected. Lastly, a Pt coating will be implemented on the top of the shaft (via electron beam physical vapor deposition sputtering) to obtain a better connection to model LIB electrodes for optimal electrochemical measurements. This optimized test cell design can help to answer some mechanistic questions about LIB materials previously studied in our group. In particular, we are interested in probing the surface and bulk properties of composite and model $Li_3V_2(PO_4)_3$ electrodes at high charging potentials where a solid electrolyte interphase (SEI) is formed. We are also

interested in understanding physical chemistry properties of LIB electrolytes at high charging and low discharging potentials to gain a more fundamental understanding of the reaction mechanisms of the SEI.

5.5 REFERENCES

(1) Skoog, D. A.; Holler, J.; Crouch, S. R. *Principles of Instrumental Analysis*, 6th ed.; Cengage Learning: Boston, 2006.

(2) Baddour-Hadjean, R.; Pereira-Ramos, J.-P. *Chem Rev* **2009**, *110* (3), 1278.

(3) Dylla, A. G.; Stevenson, K. J. *J. Mater. Chem. A* **2014**, *2* (47), 20331.

(4) Shu, J.; Shui, M.; Xu, D.; Gao, S.; Yi, T.; Wang, D.; Li, X.; Ren, Y. *Ionics* **2011**, *17* (6), 503.

(5) Murugesan, S.; Harris, J. T.; Korgel, B. A.; Stevenson, K. J. *Chem. Mater.* **2012**, *24* (7), 1306.

(6) Wu, J.; Dathar, G.K.P.; Sun, C.; Theivanayagam, M.G.; Applestone, D.; Dylla, A.G.; Manthiram, A.; Goodenough, J.B.; Stevenson, K.J. *Nanotechnology* **2013**, *24* (42), 424009/1.

(7) Kim, Y. A.; Kojima, M.; Muramatsu, H.; Umemoto, S.; Watanabe, T.; Yoshida, K.; Sato, K.; Ikeda, T.; Hayashi, T.; Endo, M.; Terrones, M.; Dresselhaus, M. S. *Small* **2006**, *2* (5), 667.

(8) Burba, C. M.; Frech, R. *Appl. Spectrosc.* **2006**, *60* (5), 490.

(9) Gross, T.; Giebeler, L.; Hess, C. *Rev. Sci. Instrum.* **2013**, *84* (7), 073109.

(10) Syzdek, J.; Marcinek, M.; Kostecki, R. *J. Power Sources* **2014**, *245* (0), 739.

(11) Lei, J.; McLarnon, F.; Kostecki, R. *J. Phys. Chem. B* **2005**, *109* (2), 952.

(12) Sturm, P.; Leuenberger, M.; Sirignano, C.; Neubert, R. E. M.; Meijer, H. A. J.; Langenfelds, R.; Brand, W. A.; Tohjuma, Y. *J. Geophys. Res.* **2004**, *109* (d4), D04309/1.

(13) Burgmayer, S. J. N. *J. Chem. Educ.* **1998**, *75* (4), 460.

(14) Charlton, M. PhD Dissertation, The University of Texas at Austin: Austin, 2015.

(15) Yu, D. Y. W.; Fietzek, C.; Weydanz, W.; Donoue, K.; Inoue, T.; Kurokawa, H.; Fujitani, S. *J. Electrochem. Soc.* **2007**, *154* (4), A253.

(16) Ricci, P. C.; Carbonaro, C. M.; Stagi, L.; Salis, M.; Casu, A.; Enzo, S.; Delogu, F. *J. Phys. Chem. C* **2013**, *117* (15), 7850.

(17) Dambournet, D.; Belharouak, I.; Amine, K. *Chem. Mater.* **2010**, *22* (3), 1173.

Appendix

Table A.1 VASP-DFT calculations of the 120 Raman wavenumbers and symmetry assignments for α-$Li_3V_2(PO_4)_3$.

Table S1. Raman modes for $Li_3V_2(PO_4)_3$ in units of cm^{-1}		
Number	Calculated	Assignment
1	1206.7	A_g
2	1189.5	B_g
3	1152.1	B_g
4	1123.3	A_g
5	1106.3	B_g
6	1085.7	A_g
7	1065.5	*Bg*
8	1055.3	*Bg*
9	1051.2	*Ag*
10	1041.7	*Bg*
11	1030.4	*Ag*
12	1021.6	*Bg*
13	1021.5	*Ag*
14	1011.2	*Bg*
15	1011.0	*Ag*
16	1010.2	*Ag*
17	1004.7	*Bg*
18	999.3	*Ag*

19	980.2	*Bg*
20	974.0	*Bg*
21	974.0	*Ag*
22	968.0	*Ag*
23	935.9	*Bg*
24	932.0	*Ag*
25	686.9	*Bg*
26	676.0	*Bg*
27	671.6	*Ag*
28	654.9	*Ag*
29	646.7	*Ag*
30	637.4	*Bg*
31	622.9	*Bg*
32	620.0	*Bg*
33	614.9	*Ag*
34	610.7	*Ag*
35	607.9	*Bg*
36	599.7	*Bg*
37	597.8	*Ag*
38	593.7	*Ag*
39	584.5	*Bg*
40	583.3	*Ag*
41	563.2	*Bg*
42	560.4	*Ag*

43	534.9	*Ag*
44	531.6	*Bg*
45	517.3	*Bg*
46	517.2	*Ag*
47	508.3	*Ag*
48	507.9	*Bg*
49	480.9	*Bg*
50	472.9	*Ag*
51	461.7	*Ag*
52	460.7	*Ag*
53	460.5	*Bg*
54	451.2	*Bg*
55	444.5	*Ag*
56	443.1	*Bg*
57	439.2	*Ag*
58	438.0	*Bg*
59	427.5	*Bg*
60	426.7	*Ag*
61	412.1	*Bg*
62	394.8	*Bg*
63	387.1	*Ag*
64	377.9	*Ag*
65	376.5	*Ag*
66	373.1	*Bg*

67	364.2	*Bg*
68	359.6	*Ag*
69	353.1	*Bg*
70	346.1	*Ag*
71	342.0	*Ag*
72	332.2	*Bg*
73	323.2	*Ag*
74	322.0	*Bg*
75	320.2	*Ag*
76	315.1	*Bg*
77	305.6	*Ag*
78	298.0	*Bg*
79	294.9	*Ag*
80	288.1	*Bg*
81	285.6	*Ag*
82	278.0	*Bg*
83	266.4	*Bg*
84	263.1	*Ag*
85	252.7	*Ag*
86	251.1	*Bg*
87	249.3	*Ag*
88	245.2	*Bg*
89	237.7	*Bg*
90	236.7	*Ag*

91	233.6	*Bg*
92	225.9	*Bg*
93	224.3	*Ag*
94	208.5	*Ag*
95	207.2	*Bg*
96	201.3	*Ag*
97	200.0	*Bg*
98	194.0	*Ag*
99	193.3	*Bg*
100	187.7	*Ag*
101	182.9	*Bg*
102	180.7	*Ag*
103	179.3	*Ag*
104	172.6	*Bg*
105	167.6	*Ag*
106	161.4	*Bg*
107	156.5	*Ag*
108	154.7	*Bg*
109	146.2	*Bg*
110	140.6	*Bg*
111	140.6	*Ag*
112	136.2	*Ag*
113	124.0	*Bg*
114	116.8	*Bg*

115	113.2	*Ag*
116	110.0	*Bg*
117	108.5	*Ag*
118	90.3	*Ag*
119	87.5	*Bg*
120	73.5	*Ag*

.

References

Chapter 1

(1) Wigley, T. M. L.; Raper, S. C. B. *Science* **2001**, *293* (5529), 451.

(2) Winter, M.; Brodd, R. J. *Chem. Rev.* **2004**, *104* (10), 4245.

(3) Karden, E.; Shinn, P.; Bostock, P.; Cunningham, J.; Schoultz, E.; Kok, D. *Sel. Pap. Ninth Eur. Lead Battery Conf. Ninth Eur. Lead Battery Conf.* **2005**, *144* (2), 505.

(4) Armand, M.; Tarascon, J.-M. *Nature* **2008**, *451* (7179), 652.

(5) Thackeray, M. M.; Wolverton, C.; Isaacs, E. D. *Energy Environ. Sci.* **2012**, *5* (7), 7854.

(6) Tarascon, J.-M.; Armand, M. *Nature* **2001**, *414* (6861), 359.

(7) Etacheri, V.; Marom, R.; Elazari, R.; Salitra, G.; Aurbach, D. *Energy Environ. Sci.* **2011**, *4* (9), 3243.

(8) Whittingham, M. S. *Chem. Rev.* **2004**, *104* (10), 4271.

(9) Whittingham, M. S. *Chem. Rev.* **2014**, *114* (23), 11414.

(10) Goodenough, J. B.; Kim, Y. *Chem. Mater.* **2010**, *22* (3), 587.

(11) Xu, K. *Chem. Rev.* **2004**, *104* (10), 4303.

(12) Okubo, M.; Hosono, E.; Kim, J.; Enomoto, M.; Kojima, N.; Kudo, T.; Zhou, H.; Honma, I. *J. Am. Chem. Soc.* **2007**, *129* (23), 7444.

(13) Yersak, T. A.; Yan, Y.; Stoldt, C.; Lee, S.-H. *ECS Electrochem. Lett.* **2012**, *1* (1), A21.

(14) Liu, D.; Zhu, W.; Trottier, J.; Gagnon, C.; Barray, F.; Guerfi, A.; Mauger, A.; Groult, H.; Julien, C. M.; Goodenough, J. B.; Zaghib, K. *RSC Adv.* **2014**, *4* (1), 154.

(15) Yuan, L.-X.; Wang, Z.-H.; Zhang, W.-X.; Hu, X.-L.; Chen, J.-T.; Huang, Y.-H.; Goodenough, J. B. *Energy Environ. Sci.* **2011**, *4* (2), 269.

(16) Watanabe, T.; Ikeda, Y.; Ono, T.; Hibino, M.; Hosoda, M.; Sakai, K.; Kudo, T. *Proc. Second Int. Symp. Soft Solut. Process. 2000* **2002**, *151* (1–4), 313.

(17) Jiajun, C. *Materials* **2013**, *6* (1), 156.

(18) Harrison, K. L.; Bridges, C. A.; Segre, C. U.; Varnado, C. D.; Applestone, D.; Bielawski, C. W.; Paranthaman, M. P.; Manthiram, A. *Chem. Mater.* **2014**, *26* (12), 3849.

(19) Rui, X.; Yan, Q.; Skyllas-Kazacos, M.; Lim, T. M. *J. Power Sources* **2014**, *258* (0), 19.

(20) Jiang, T.; Pan, W.; Wang, J.; Bie, X.; Du, F.; Wei, Y.; Wang, C.; Chen, G. *Electrochimica Acta* **2010**, *55* (12), 3864.

(21) Qiao, Y. Q.; Tu, J. P.; Xiang, J. Y.; Wang, X. L.; Mai, Y. J.; Zhang, D.; Liu, W. L. *Electrochimica Acta* **2011**, *56* (11), 4139.

(22) Ko, Y. N.; Koo, H. Y.; Kim, J. H.; Yi, J. H.; Kang, Y. C.; Lee, J.-H. *15th Int. Meet. Lithium Batter. IMLB* **2011**, *196* (16), 6682.

(23) Lee, S.; Park, S. S. *J. Phys. Chem. C* **2012**, *116* (48), 25190.

(24) Mai, L.; Li, S.; Dong, Y.; Zhao, Y.; Luo, Y.; Xu, H. *Nanoscale* **2013**, *5* (11), 4864.

(25) Pan, A.; Choi, D.; Zhang, J.-G.; Liang, S.; Cao, G.; Nie, Z.; Arey, B. W.; Liu, J. *J. Power Sources* **2011**, *196* (7), 3646.

(26) Chen, Q.; Zhang, T.; Qiao, X.; Li, D.; Yang, J. *J. Power Sources* **2013**, *234* (0), 197.

(27) Qiao, Y. Q.; Wang, X. L.; Mai, Y. J.; Xiang, J. Y.; Zhang, D.; Gu, C. D.; Tu, J. P. *J. Power Sources* **2011**, *196* (20), 8706.

(28) Chen, Y.; Zhang, D.; Bian, X.; Bie, X.; Wang, C.; Du, F.; Jang, M.; Chen, G.; Wei, Y. *Electrochimica Acta* **2012**, *79* (0), 95.

(29) Yoon, J.; Muhammad, S.; Jang, D.; Sivakumar, N.; Kim, J.; Jang, W.-H.; Lee, Y.-S.; Park, Y.-U.; Kang, K.; Yoon, W.-S. *J. Alloys Compd.* **2013**, *569* (0), 76.

(30) Burba, C. M.; Frech, R. *Solid State Ion.* **2007**, *177* (39–40), 3445.

(31) Zhang, L.-L.; Liang, G.; Peng, G.; Zou, F.; Huang, Y.-H.; Croft, M. C.; Ignatov, A. *J. Phys. Chem. C* **2012**, *116* (23), 12401.

(32) Skoog, D. A.; Holler, J.; Crouch, S. R. *Principles of Instrumental Analysis*, 6th ed.; Cengage Learning: Boston, 2006.

(33) Schroder, K. W.; Celio, H.; Webb, L. J.; Stevenson, K. J. *J. Phys. Chem. C* **2012**, *116* (37), 19737.

(34) Baddour-Hadjean, R.; Pereira-Ramos, J.-P. *Chem Rev* **2009**, *110* (3), 1278.

(35) Arumugam Manthiram. In *Battery Applications*; The University of Texas at Austin; pp 68–82.

(36) Besenhard, J. O. *Carbon* **1976**, *14* (2), 111.

(37) Besenhard, J. O.; Fritz, H. P. *Angew. Chem. Int. Ed. Engl.* **1983**, *22* (12), 950.

(38) Aldon, L.; Kubiak, P.; Womes, M.; Jumas, J. C.; Olivier-Fourcade, J.; Tirado, J. L.; Corredor, J. I.; Pérez Vicente, C. *Chem. Mater.* **2004**, *16* (26), 5721.

(39) McDowell, M. T.; Lee, S. W.; Nix, W. D.; Cui, Y. *Adv. Mater.* **2013**, *25* (36), 4966.

(40) Cabana, J.; Monconduit, L.; Larcher, D.; Palacín, M. R. *Adv. Mater.* **2010**, *22* (35), E170.

(41) Bernardi, J. *Ph. D. Thesis dissertation*; University of Montpellier: Montpellier, France, 2008.

(42) Boyanov, S.; Bernardi, J.; Gillot, F.; Dupont, L.; Womes, M.; Tarascon, J.-M.; Monconduit, L.; Doublet, M.-L. *Chem. Mater.* **2006**, *18* (15), 3531.

(43) Boyanov, S.; Womes, M.; Monconduit, L.; Zitoun, D. *Chem. Mater.* **2009**, *21* (15), 3684.

(44) Silva, D. C. C.; Crosnier, O.; Ouvrard, G.; Greedan, J.; Safa-Sefat, A.; Nazar, L. F. *Electrochem. Solid-State Lett.* **2003**, *6* (8), A162.

(45) Doe, R. E.; Persson, K. A.; Meng, Y. S.; Ceder, G. *Chem. Mater.* **2008**, *20* (16), 5274.

(46) Hall, J. W.; Membreno, N.; Wu, J.; Celio, H.; Jones, R. A.; Stevenson, K. J. *J. Am. Chem. Soc.* **2012**, *134* (12), 5532.

(47) Membreño, N.; Xiao, P.; Park, K.-S.; Goodenough, J. B.; Henkelman, G.; Stevenson, K. J. *J. Phys. Chem. C* **2013**, *117* (23), 11994.

(48) Wu, J.; Dathar, G.K.P.; Sun, C.; Theivanayagam, M.G.; Applestone, D.; Dylla, A.G.; Manthiram, A.; Goodenough, J.B.; Stevenson, K.J. *Nanotechnology* **2013**, *24* (42), 424009/1.

Chapter 2

(1) (a) Karden, E.; Ploumen, S.; Fricke, B.; Miller, T.; Snyder, K. *J. Power Sources* **2007**, *168*, 2. (b) Kennedy, B.; Patterson, D.; Camilleri, S. *J. Power Sources* **2000**, *90*, 156. (c) Scrosati, B.; Garche, J. *J. Power Sources* **2010**, *195*, 2419. (d) Kang, B.; Ceder, G. *Nature* **2009**, *458*, 190.

(2) Biensan, P.; Simon, B.; Pere, J. P.; de Guibert, A.; Broussely, M.; Bodet, J. M.; Perton, F. *J. Power Sources* **1999**, *81*, 906.

(3) Choi, N.-S.; Profatilova, I. A.; Kim, S.-S.; Song, E.-H.; *Thermochim. Acta*, **2008**, *480*, 10.

(4) Haxel, G. B.; Hedrick, J. B.; Orris, G. J.; *Rare Earth Elements-Critical Resources for High Technology*; Fact Sheet 087-02; U.S. Geological Survey: Reston, VA, 2002.

(5) (a) Bruce, P. G.; Scrosati, B.; Tarascon, J.-M. *Angew. Chem. Int. Ed.* **2008**, *47*, 2930. (b) Guo, J.; Liu, Q.; Wang, C.; Zachariah, M. R. *Adv. Funct. Mater*. **2011**, *22*, 803.

(6) Guo, Y.-G.; Hu, J.-S.; Wan, L.-J. *Adv. Mater.* **2008**, *20*, 2878.

(7) Wang, Y.; Cao, G. *Adv. Mater.* **2008**, *20*, 2251.

(8) (a) Gillot, F.; Bichat, M. P.; Favier, F.; Morcrette, M.; Doublet, M. L.; Monconduit, L. *Electrochim. Acta* **2004**, *49*, 2325. (b) Pralong, V.; Souza, D. C. S.; Leung, K. T.; Nazar, L. F. *Electrochem. Commun.* **2002**, *4*, 516. (c) Souza, D. C. S.; Pralong, V.; Jacobson, A. J.; Nazar, L. F. *Science* **2002**, *296*, 2012. (d) Doublet, M.-L.; Lemoigno, F.; Gillot, F.; Monconduit, L. *Chem. Mater.* **2002**, *14*, 4126. (e) Bichat, M.-P.; Gillot, F.; Monconduit, L.; Favier, F.; Morcrette, M.; Lemoigno, F.; Doublet, M.-L. *Chem. Mater.* **2004**, *16*, 1002. (f) Gillot, F.; Monconduit, L.; Doublet, M.-L. *Chem. Mater.* **2005**, *17*, 5817. (g) Bichat, M.-P.; Pascal, J.-L.; Gillot, F.; Favier, F. *Chem. Mater.* **2005**, *17*, 6761. (h) Boyanov, S.; Bernardi, J.; Gillot, F.; Dupont, L.; Womes, M.; Tarascon, J.-M.; Monconduit, L.; Doublet, M.-L. *Chem. Mater.* **2006**, *18*, 3531. (i) Gillot, F.; Menetrier, M.; Bekaert, E.; Dupont, L.; Morcrette, M.; Monconduit, L.; Tarascon, J. M. *J. Power Sources* **2007**, *172*, 877. (j) Boyanov, S.; Annou, K.; Villevieille, C.; Pelosi, M.; Zitoun, D.; Monconduit, L. *Ionics*, **2008**, *14*, 183. (k) Villevieille, C.; Robert, F.; Taberna, P. L.; Bazin, L.; Simon, P.; Monconduit, L. *J. Mater. Chem.* **2008**, *18*, 5956. (l) Kim, M. G.; Lee, S.; Cho, J. *J. Electrochem. Soc.* **2009**, *156*, A89. (m) Boyanov, S.; Bernardi, J.; Bekaert, E.; Menetrier, M.; Doublet, M.-L.; Monconduit, L. *Chem. Mater.* **2009**, *21*, 298. (n) Kim, M. G.; Cho, J. *J. Electrochem. Soc.* **2009**, *156*, A277. (o) Mauchamp, V.; Moreau, P.; Monconduit, L.; Doublet, M.; Boucher, F.; Ouvard, G. *J. Phys. Chem. C* **2007**, *111*, 3996. (p) Xiang, J. Y.; Wang, X. L.; Zhong, J.; Zhang, D.; Tu, J. P. *J. Power Sources* **2011**, *196*, 379. (q) Xiang, J. Y.; Wang, X. L.; Xia, X. H.; Zhong, J.; Tu, J. P. *J. Alloys Compd.* **2011**, *509*, 157.

(9) (a) Boyanov, S.; Zithoun, D.; Menetrier, M.; Jumas, J. C. ; Womes, M.; Monoconduit, L. *J. Phys. Chem. C*, **2009**, *113*, 21441-21452. (b) Boyanov, S.; Womes, M.; Jumas, J. C.; Monoconduit, *Hyperfine Interact*, **2008**, *187*, 57-69. (c) Silva, D. C. C.;Crosnier, O.; Ouvrard, G.; Greedan, J.; Safa-Sefat, A.; Nazar, L. F. *Electrochem and Solid State Lett.* **2003**, *6*, A162-A165.

(10) (a) Brock, S. L.; Senevirathne, K. *J. Solid State Chem.* **2008**, *181*, 1552. (b) Stamm, K. L.; Brock, S. L. *J. Alloys and Compounds*, **2008**, *453*, 476. (c) Senevirathne, K.; Burns, A. W.; Bussell, M. E.; Brock, S. L. *Adv. Funct. Mater.* **2007**, *17*, 3933. (d) Gregg, K. A.; Perera, S. C.; Lawes, G.; Shinozaki, S.; Brock, S. L. *Chem. Mater.* **2006**, *18*, 879. (e) Somaskandan, K.; Tsoi, G. M.; Wenger, L.

E.; Brock, S. L. *Chem. Mater.* **2005**, *17*, 1190. (f) Aitken, J. A.; Ganzha-Hazen, V.; Brock, S. L. *J Solid State Chem.* **2005**, *178*, 970. (g) Perera, S. C.; Brock, S. L. Mat. Res. Soc. Symp. Proc. 2003, 755, DD5.91-DD6.12.6. (h) Perera, S. C.; Fodor, P. S.; Tsoi, G. M.; Wenger, L. E.; Brock, S. L. *Chem. Mater.* **2003**, *15*, 4034. (i) Perera, S. C.; Tsoi, G.; Wenger, L. E.; Brock, S. L. *J. Am. Chem. Soc.* **2003**, *125*, 13960. (j) Stamm, K. L.; Garno, J. C.; Liu, G-Y.; Brock, S. L. *J. Am. Chem. Soc.* **2003**, *125*, 4038. (k) Muthuswamy, E.; Brock, S. L. *J. Am. Chem. Soc.* **2010**, *132*, 15849. (l) Muthuswamy, E.; Brock, S. L. *Chem. Commun.* **2011**, *47*, 12334.

(11) (a) Henkes, A. E.; Schaak, R. E. *Inorg. Chem.* **2008**, *47*, 671. (b) Henkes, A. E.; Vasquez, Y.; Schaak, R. E. *J. Am. Chem. Soc.* **2007**, *129*, 1896. (c) Henkes, A. E.; Schaak, R. E. *Chem. Mater*. **2007**, 19, 4234.

(12) Qian, C.; Kim, F.; Ma, L.; Tsui, F.; Yang, P.; Liu, J. *J. Am. Chem. Soc.* **2004**, *126*, 1195.

(13) Wang, M.; McDonald, R.; Mar, A. *Inorg. Chem.* **2000**, *39*, 4936.

(14) (a) Kleinke, H.; Franzen, H. F. J. Solid State Chem. 1997, 131, 379-386. (b) Kleinke, H.; Franzen, H. F. *J. Am. Chem. Soc*. **1997**, *119*, 12824.

(15) Chen, L.; Huang, M.; Gu, Y.; Shi, L.; Yang, Z.; Qian, Y. *Materials Letters*, **2004**, *58,* 3337.

(16) Liu, S.; Qian, Y.; Xu, L. *Solid State Communications*, **2009**, *149*, 438.

(17) Barry, B. M.; Gillan, E. G. *Chem. Mater.* **2008**, *20*, 2618.

(18) George, P. P.; Pol, V. G.; Gedanken, A. *J. Nanoparticle Research,* **2007**, *9*, 1187.

(19) (a) Davidson, P. J.; Lappert, M. F.; Pearce, R. *Chem. Rev.* **1976,** *76,* 219-242. (b) Schrock, R. R.; Parshall, G. W. *Chem. Rev.* **1976,** *76,* 243.

(20) Lappert, M. F.; Power, P. P.; Protchenko, A.; Seeber, A.; John Wiley and Sons Pub., **2008**, Ch.6 pp 149.

(21) Literature from the 19th and early 20th centuries contains evidence that PH_3 will react with salts of Cr, U, Mn, Ni, Co and Fe to form metal phosphides, however these materials are poorly characterized and these reactions do not appear to have been investigated in the modern era. See for example *Gmelins Handbuch der Anorganischen Chemie*, Part C, **1965**, *16*, 45.

(22) **Caution:** Phosphine is a highly poisonous and reactive gas. All operations must be performed by highly trained personnel under rigorous exclusion of air.

(23) Alyea, E. C.; Bradley, D. C.; Copperthwaite, R. G. *Dalton Trans.* **1972**, 1580.

(24) Celio, H.; Johnson, A. J. University of Texas, Austin, TX. Unpublished work, 2012.

(25) Grosvenor, A. P.; Cavell, R. G.; Mar, A. *Struct. Bond.* **2009,** *133,* 4.

(26) Grosvenor, A. P.; Wik, S. D.; Cavell, R. G.; Mar, A. *Inorg. Chem.* **2005,** *44,* 8988.

(27) Myers, C. E.; Franzen, H. F.; Anderegg, J. W. *Inorg. Chem.* **1985,** *24,* 1822.

(28) Wagner, C. D.; Naumkin, A. V.; Kraut-Vass, A.; Allison, J. W.; Powell, C. J.; Rumble, J. R., Jr. *NIST X-ray Photoelectron Spectroscopy (XPS) Database, Version 3.5.* http://srdata.nist.gov/xps/ Default.aspx (Accessed July 2011).

(29) Nemoshkalenko, V. V.; Didyk, V. V.; Krivitskii, V. P.; Senkevich, A. I. *Zh. Neorg. Khim.* **1983,** *28,* 2182-2186. (30) Ohkawa, H.; Yoshida, K.; Saito, M.; Uematsu, K.; Toda, K.; Sato, M. *Chem. Lett.* **1999**, *28*, 1017.

(30) Cyclability is defined as the coulomic efficiency between lithation and delithation. In specific terms the coulombic efficiency of battery is the ratio of integrated charge associated with charging compared to the charge that can be extracted from the battery during discharging. The losses that reduce coulombic efficiency are primarily due to the loss in charge due to secondary reactions, such as the electrolysis of solvent or other surface redox reactions in the battery.

(31) Qian, C.; Kim, F.; Ma, L.; Tsui, F.; Yang, P.; Liu, J. *J. Am. Chem. Soc.* **2004**, *126*, 1195.

(32) Balaya, P.; Bhattacharyya, A. J.; Jamnik, J.; Zhukovskii, Yu. F.; Kotomin, E. A.; Maier, J. *J. Power Sources* **2006**, *159*, 171.

(33) Maier, J. *J. Power Sources* **2007**, *174*,569.

Chapter 3

(1) Yuan, L.-X.; Wang, Z.-H.; Zhang, W.-X.; Hu, X.-L.; Chen, J.-T.; Huang, Y.-H.; Goodenough, J. B. Energy Environ. *Sci.* **2011**, *4*, 269.

(2) Yin, S.-C.; Grondey, H.; Strobel, P.; Anne, M.; Nazar, L. F. *J. Am. Chem. Soc.* **2003**, *125*, 10402.

(3) Huang, H.; Yin, S.-C.; Kerr, T.; Taylor, N.; Nazar, L. F. *Adv. Mater.* **2002**, *14*, 1525.

(4) Lee, S.; Park, S. S. *J. Phys. Chem. C* **2012**, *116*, 25190.

(5) Baddour-Hadjean, R.; Pereira-Ramos, J.-P. *Chem Rev* **2009**, *110*, 1278.

(6) Morcrette, M.; Leriche, J.-B.; Patoux, S.; Wurm, C.; Masquelier, C. *Electrochem. Solid-State Lett.* **2003**, *6*, A80.

(7) Burba, C. M.; Frech, R. *Solid State Ion.* **2007**, *177*, 3445.

(8) Shu, J.; Shui, M.; Xu, D.; Gao, S.; Yi, T.; Wang, D. J.; Li, X.; Ren, Y. *Ionics* **2011**, *17*, 503.

(9) Burba, C. M.; Frech, R. *Appl. Spectrosc.* **2006**, *60*, 490.

(10) Kim, Y. A.; Kojima, M.; Muramatsu, H.; Umemoto, S.; Watanabe, T.; Yoshida, K.; Sato, K.; Ikeda, T.; Hayashi, T.; Endo, M.; Terrones, M.; Dresselhaus, M. S. *Small* **2006**, *2*, 667.

(11) Cahill, L. S.; Chapman, R. P.; Britten, J. F.; Goward, G. R. *J. Phys. Chem. B* **2006**, *110*, 7171.

(12) Yin, S.-C.; Grondey, H.; Strobel, P.; Huang, H.; Nazar, L. F. *J. Am. Chem. Soc.* **2002**, *125*, 326.

(13) Patoux, S.; Wurm, C.; Morcrette, M.; Rousse, G.; Masquelier, C. *Sel. Pap. Present. 11th Int. Meet. Lithium Batter.* **2003**, *119–121*, 278.

(14) Burba, C. M.; Frech, R. *J. Electrochem. Soc.* **2004**, *151*, A1032.

(15) Barj, M.; Lucazeau, G.; Delmas, C. *J. Solid State Chem.* **1992**, *100*, 141.

(16) Butt, G.; Sammes, N.; Tompsett, G.; Smirnova, A.; Yamamoto, O. *J. Power Sources* **2004**, *134*, 72.

(17) Kravchenko, V. V.; Mikhailov, V. I.; Sigarev, S. E. *Solid State Ion.* **1992**, *50*, 19.

(18) Paraguassu, W.; Freire, P. T. C.; Lemos, V.; Lala, S. M.; Montoro, L. A.; Rosolen, J. M. *J. Raman Spectrosc.* **2005**, *36*, 213.

(19) Kohn, W.; Becke, A. D.; Parr, R. G. *J. Phys. Chem.* **1996**, *100*, 12974.

(20) Heyd, J.; Scuseria, G. E.; Ernzerhof, M. *J. Chem. Phys.* **2003**, *118*, 8207.

(21) Kresse, G.; Furthmüller, J. *Comput. Mater. Sci.* **1996**, *6*, 15.

(22) Kresse, G.; Furthmüller, J. *Phys. Rev. B* **1996**, *54*, 11169.

(23) Blochl, P. E. *Phys. Rev. B* **1994**, *50*, 17953.

(24) Kresse, G.; Joubert, D. *Phys. Rev. B* **1999**, *59*, 1758.

(25) pyspglib for ASE, 2013. http://spglib.sourceforge.net/pyspglibForASE

(26) Canepa, P.; Hanson, R. M.; Ugliengo, P.; Alfredsson, M. *J. Appl. Crystallogr.* **2011**, *44*, 225.

(27) Bai, Y.; Yin, Y.; Yang, J.; Qing, C.; Zhang, W. *J. Raman Spectrosc.* **2011**, *42*, 831.

(28) Shebanova, O. N.; Lazor, P. *J. Raman Spectrosc.* **2003**, *34*, 845.

(29) Bykov, A. B.; Chirkin, A. P.; Demyanets, L. N.; Doronin, S. N.; Genkina, E. A.; Ivanov-Shits, A. K.; Kondratyuk, I. P.; Maksimov, B. A.; Mel'nikov, O. K.; Muradyan, L. N.; Simonov, V. I.; Timofeeva, V. A. *Solid State Ion.* **1990**, *38*, 31.

(30) Ohkawa, H.; Yoshida, K.; Saito, M.; Uematsu, K.; Toda, K.; Sato, M. *Chem. Lett.* **1999**, *28*, 1017.

(31) Sato, M.; Ohkawa, H.; Yoshida, K.; Saito, M.; Uematsu, K.; Toda, K. *Proc. 12th Int. Conf. Solid State* **2000**, *135*, 137.

(32) Kuang, Q.; Zhao, Y.; An, X.; Liu, J.; Dong, Y.; Chen, L. *Electrochimica Acta* **2010**, *55*, 1575.

(33) Baran, E. J.; Vassallo, M. B.; Lii, K. H. *J. Raman Spectrosc.* **1994**, *25*, 199.

(34) Kuo, H. T.; Bagkar, N. C.; Liu, R. S.; Shen, C. H.; Shy, D. S.; Xing, X. K.; Lee, J.-F.; Chen, J. M. *J. Phys. Chem. B* **2008**, *112*, 11250.

(1) Goodenough, J. B.; Kim, Y. *Chem. Mater.* **2009**, *22*, 587.

(2) Yuan, L.-X.; Wang, Z.-H.; Zhang, W.-X.; Hu, X.-L.; Chen, J.-T.; Huang, Y.-H.; Goodenough, J. B. *Energy Environ. Sci.* **2011**, *4*, 269.

(3) Sharabi, R.; Markevich, E.; Borgel, V.; Salitra, G.; Gershinsky, G.; Aurbach, D.; Semrau, G.; Schmidt, M. A.; Schall, N.; Stinner, C. *J. Power Sources* **2012**, *203*, 109.

(4) Pivko, M.; Bele, M.; Tchernychova, E.; Logar, N. Z.; Dominko, R.; Gaberscek, M. *Chem. Mater.* **2012**, *24*, 1041.

(5) Wolfenstine, J.; Allen, J. *J. Power Sources* **2005**, *142*, 389.

(6) Rui, X.; Yan, Q.; Skyllas-Kazacos, M.; Lim, T. M. *J. Power Sources* **2014**, *258*, 19.

(7) Yin, S.-C.; Grondey, H.; Strobel, P.; Anne, M.; Nazar, L. F. *J. Am. Chem. Soc.* **2003**, *125*, 10402.

(8) Huang, H.; Yin, S.-C.; Kerr, T.; Taylor, N.; Nazar, L. F. *Adv. Mater.* **2002**, *14*, 1525.

(9) Su, J.; Wu, X.-L.; Lee, J.-S.; Kim, J.; Guo, Y.-G. *J. Mater. Chem. A* **2013**, *1*, 2508.

(10) Patoux, S.; Wurm, C.; Morcrette, M.; Rousse, G.; Masquelier, C. *Sel. Pap. Present. 11th Int. Meet. Lithium Batter.* **2003**, *119–121*, 278.

(11) Jiang, T.; Wang, C.; Chen, G.; Chen, H.; Wei, Y.; Li, X. *Solid State Ion.* **2009**, *180*, 708.

(12) Xu, K. *Chem. Rev.* **2004**, *104*, 4303.

(13) Verma, P.; Maire, P.; Novák, P. *Electrochimica Acta* **2010**, *55*, 6332.

(14) Aurbach, D.; Zinigrad, E.; Cohen, Y.; Teller, H. *Proc. Symp. Mater. Adv. Batter. Fuel Cells Organised Conjunction Int. Conf. Mater. Adv. Technol. ICMAT 2001* **2002**, *148*, 405.

(15) Balbuena, Perla B.; Wang, Yixuan. *Lithium-Ion Batteries: Solid-Electrolyte Interphase*; Imperial College Press, 2004.

(16) Pérez-Villar, S.; Lanz, P.; Schneider, H.; Novák, P. *Electrochimica Acta* **2013**, *106*, 506.

(17) Schroder, K. W.; Celio, H.; Webb, L. J.; Stevenson, K. J. *J. Phys. Chem. C* **2012**, *116*, 19737.

(18) Xing, L.; Li, W.; Wang, C.; Gu, F.; Xu, M.; Tan, C.; Yi, J. *J. Phys. Chem. B* **2009**, *113*, 16596.

(19) Borodin, O.; Behl, W.; Jow, T. R. *J. Phys. Chem. C* **2013**, *117*, 8661.

(20) Edström, K.; Gustafsson, T.; Thomas, J. O. *Polym. Batter. Fuel CellsSelection Pap. First Int. Conf.* **2004**, *50*, 397.

(21) Ostrovskii, D.; Ronci, F.; Scrosati, B.; Jacobsson, P. *J. Power Sources* **2001**, *103*, 10.

(22) Malmgren, S.; Rensmo, H.; Gustafsson, T.; Gorgoi, M.; Edström, K. *ECS Trans.* **2010**, *25*, 201.

(23) Castro, L.; Dedryvère, R.; Ledeuil, J.-B.; Bréger, J.; Tessier, C.; Gonbeau, D. *J. Electrochem. Soc.* **2012**, *159*, A357.

(24) Membreño, N.; Xiao, P.; Park, K.-S.; Goodenough, J. B.; Henkelman, G.; Stevenson, K. J. *J. Phys. Chem. C* **2013**, *117*, 11994.

(25) Yin, S.-C.; Grondey, H.; Strobel, P.; Huang, H.; Nazar, L. F. *J. Am. Chem. Soc.* **2002**, *125*, 326.

(26) Dedryvère, R.; Maccario, M.; Croguennec, L.; Le Cras, F.; Delmas, C.; Gonbeau, D. *Chem. Mater.* **2008**, *20*, 7164.

(27) Strzemiecka, B.; Voelkel, A.; Donate-Robles, J.; Martín-Martínez, J. M. *Appl. Surf. Sci.* **2014**, *316*, 315.

(28) Beamson, G.; Briggs, D. *High Resolution of organic polymers: The Scienta ESCA 300 database*; John Wiley & Sons: Chichester, U.K., 1992; Vol. 15.

(29) Chen, Y.; Zhang, D.; Bian, X.; Bie, X.; Wang, C.; Du, F.; Jang, M.; Chen, G.; Wei, Y. *Electrochimica Acta* **2012**, *79*, 95.

(30) Aurbach, D.; Markovsky, B.; Shechter, A.; Ein-Eli, Y.; Cohen, H. *J. Electrochem. Soc.* **1996**, *143*, 3809.

(31) Andersson, A. .; Henningson, A.; Siegbahn, H.; Jansson, U.; Edström, K. *Sel. Pap. Present. 11th Int. Meet. Lithium Batter.* **2003**, *119–121*, 522.

(32) Eshkenazi, V.; Peled, E.; Burstein, L.; Golodnitsky, D. *Solid State Ion.* **2004**, *170*, 83.

(33) Peled, E.; Bar Tow, D.; Merson, A.; Gladkich, A.; Burstein, L.; Golodnitsky, D. *Proc. 10th Int. Meet. Lithium Batter.* **2001**, *97–98*, 52.

(34) Moshkovich, M.; Cojocaru, M.; Gottlieb, H. .; Aurbach, D. *J. Electroanal. Chem.* **2001**, *497*, 84.

(35) Aurbach, D.; Markovsky, B.; Levi, M. .; Levi, E.; Schechter, A.; Moshkovich, M.; Cohen, Y. *J. Power Sources* **1999**, *81–82*, 95.

(36) Aurbach, D. *J. Power Sources* **2000**, *89*, 206.

(37) Zhang, S. S.; Xu, K.; Jow, T. R. *Electrochem. Solid-State Lett.* **2002**, *5*, A92.

(38) Chang, L.-S.; Lin, Y.-C.; Su, C.-Y.; Wu, H.-C.; Pan, J.-P. *Appl. Surf. Sci.* **2011**, *258*, 1279.

(39) Tasaki, K.; Harris, S. J. *J. Phys. Chem. C* **2010**, *114*, 8076.

(40) Tasaki, K.; Goldberg, A.; Lian, J.-J.; Walker, M.; Timmons, A.; Harris, S. J. *J. Electrochem. Soc.* **2009**, *156*, A1019.

(41) Jones, J.; Anouti, M.; Caillon-Caravanier, M.; Willmann, P.; Sizaret, P.-Y.; Lemordant, D. *Fluid Phase Equilibria* **2011**, *305*, 121.

(42) Chatelier, R. C.; St John, H. A. W.; Gengenbach, T. R.; Kingshott, P.; Griesser, H. J. *Surf. Interface Anal.* **1997**, *25*, 741.

(43) Artyushkova, K.; Fulghum, J. E. *Surf. Interface Anal.* **2004**, *36*, 1304.

(44) Lei, J.; Li, L.; Kostecki, R.; Muller, R.; McLarnon, F. *J. Electrochem. Soc.* **2005**, *152*, A774.

(45) Chueh, W. C.; El Gabaly, F.; Sugar, J. D.; Bartelt, N. C.; McDaniel, A. H.; Fenton, K. R.; Zavadil, K. R.; Tyliszczak, T.; Lai, W.; McCarty, K. F. *Nano Lett.* **2013**, *13*, 866.

(46) Nanda, J.; Remillard, J.; O'Neill, A.; Bernardi, D.; Ro, T.; Nietering, K. E.; Go, J.-Y.; Miller, T. J. *Adv. Funct. Mater.* **2011**, *21*, 3282.

Chapter 5

(1) Skoog, D. A.; Holler, J.; Crouch, S. R. *Principles of Instrumental Analysis*, 6th ed.; Cengage Learning: Boston, 2006.

(2) Baddour-Hadjean, R.; Pereira-Ramos, J.-P. *Chem Rev* **2009**, *110* (3), 1278.

(3) Dylla, A. G.; Stevenson, K. J. *J. Mater. Chem. A* **2014**, *2* (47), 20331.

(4) Shu, J.; Shui, M.; Xu, D.; Gao, S.; Yi, T.; Wang, D.; Li, X.; Ren, Y. *Ionics* **2011**, *17* (6), 503.

(5) Murugesan, S.; Harris, J. T.; Korgel, B. A.; Stevenson, K. J. *Chem. Mater.* **2012**, *24* (7), 1306.

(6) Wu, J.; Dathar, G.K.P.; Sun, C.; Theivanayagam, M.G.; Applestone, D.; Dylla, A.G.; Manthiram, A.; Goodenough, J.B.; Stevenson, K.J. *Nanotechnology* **2013**, *24* (42), 424009/1.

(7) Kim, Y. A.; Kojima, M.; Muramatsu, H.; Umemoto, S.; Watanabe, T.; Yoshida, K.; Sato, K.; Ikeda, T.; Hayashi, T.; Endo, M.; Terrones, M.; Dresselhaus, M. S. *Small* **2006**, *2* (5), 667.

(8) Burba, C. M.; Frech, R. *Appl. Spectrosc.* **2006**, *60* (5), 490.

(9) Gross, T.; Giebeler, L.; Hess, C. *Rev. Sci. Instrum.* **2013**, *84* (7), 073109.

(10) Syzdek, J.; Marcinek, M.; Kostecki, R. *J. Power Sources* **2014**, *245* (0), 739.

(11) Lei, J.; McLarnon, F.; Kostecki, R. *J. Phys. Chem. B* **2005**, *109* (2), 952.

(12) Sturm, P.; Leuenberger, M.; Sirignano, C.; Neubert, R. E. M.; Meijer, H. A. J.; Langenfelds, R.; Brand, W. A.; Tohjuma, Y. *J. Geophys. Res.* **2004**, *109* (d4), D04309/1.

(13) Burgmayer, S. J. N. *J. Chem. Educ.* **1998**, *75* (4), 460.

(14) Charlton, M. PhD Dissertation, The University of Texas at Austin: Austin, 2015.

(15) Yu, D. Y. W.; Fietzek, C.; Weydanz, W.; Donoue, K.; Inoue, T.; Kurokawa, H.; Fujitani, S. *J. Electrochem. Soc.* **2007**, *154* (4), A253.

(16) Ricci, P. C.; Carbonaro, C. M.; Stagi, L.; Salis, M.; Casu, A.; Enzo, S.; Delogu, F. *J. Phys. Chem. C* **2013**, *117* (15), 7850.

(17) Dambournet, D.; Belharouak, I.; Amine, K. *Chem. Mater.* **2010**, *22* (3), 1173.